Predictive Residential Energy Management with Photovoltaic Power Generation and Battery Energy Storage

by

Stef Coetzee

Thesis presented in partial fulfilment of the requirements for the degree of Master of Engineering (Electrical) in the Faculty of Engineering at Stellenbosch University

Supervisor: Prof. Toit Mouton

April 2019

Declaration

By submitting this thesis electronically, I declare that the entirety of the work contained therein is my own, original work, that I am the sole author thereof (save to the extent explicitly otherwise stated), that reproduction and publication thereof by Stellenbosch University will not infringe any third party rights and that I have not previously in its entirety or in part submitted it for obtaining any qualification.

Stef Coetzee
April 2019

Abstract

Over the course of the past decade, South African national energy utility Eskom has increased its average electricity rate more than fourfold as it finds itself in financial difficulty, brought about by a myriad causes. During the same time period, the cost of solar photovoltaic arrays and battery energy storage has fallen by more than two thirds.

In this thesis, a residential energy management system which incorporates small-scale solar photovoltaic power generation and battery energy storage is developed. The primary goal of the system is to increase self-sufficiency of a given household through management of the battery energy storage unit and two controllable loads: an air-handling unit and an electric water heater. Such a system would be able to shield residences, at least in part, from the energy utility's ongoing challenges.

A grid-connected household, featuring each of the controllable electrical entities mentioned, as well as a photovoltaic array, and a generic non-controllable load is described. Due to the intermittent nature of solar radiation, potential solar power generation is inevitably lost because of power supply-demand misalignment. Model predictive control, a popular process-control technique, is exerted over the residential system in pursuit of resolving this misalignment.

At a sampling time of ten minutes, a predictive controller capable of an hour (or six steps) of model-based foresight is formulated and tested in simulation. A rules-based hierarchical controller is used as baseline against which the predictive control scheme is evaluated. The controller's ability to reduce solar power curtailment is confirmed by evaluating its performance with relevant data from each of the four seasons (from September 2017 to August 2018), for prediction horizons one through six.

Opsomming

Deur die loop van die afgelope tien jaar het die nasionale kragverskaffer, Eskom, sy gemiddelde elektrisiteitstarief vervierdubbel, terwyl dié staatsinstansie onder verskeie uitdagings gebuk gaan. Gedurende dieselfde tydperk het die kosprys van fotovoltaïese sonpanele en battery energiestoor met meer as twee derdes verminder.

In hierdie tesis word 'n huishoudelike energiebestuurstelsel, wat van beide 'n fotovoltaïese skikking en battery energiestooreenheid gebruik maak, beskryf. Die hoofdoelwit van die stelsel behels die verbetering van die huishouding se selfversorgendheid sover sy energiebehoeftes aangaan. Die stelsel manipuleer 'n energiestooreenheid, tesame met twee beheerbare laste, naamlik, 'n lugreëlingseenheid en elektriese waterverwarmer (algemeen bekend as 'n geiser), in die nastreef van sy doelwit. 'n Stelsel van dié aard sal daarin kan slaag om huishoudings, minstens gedeeltelik, van die kragverskaffer se uitdagings te beskerm.

'n Huishouding, aan die nasionale kragstelsel gekoppel, wat van al die beheerbare laste hierbo genoem gebruik maak, te same met 'n fotovoltaïese skikking en 'n generiese verteenwoordiging van die oorblywende huislas, word beskryf. As gevolg van die wisselende aard van sonbestraling gaan daar gereeld waardevolle potensiële energie verlore, toegeskryf aan die swak belyning tussen drywingsbron en -las. Modelgebaseerde voorspellende beheer, 'n gewilde prosesbeheertegniek, word op die huishouding toegepas in die strewe na 'n oplossing vir hierdie belyningsprobleem.

Teen 'n monstertyd van tien minute word 'n voorspellende beheerder, daartoe instaat om 'n uur (of, altans, ses stappe) vooruitskattings te maak (met die hulp van wiskundige modelle), geformuleer en in 'n simulasie-omgewing beproef. 'n Hiërargiese beheerder, gebaseer op 'n stel voorwaardelike stellings, word as maatstaf waarteen die voorspellende beheerskema geëvalueer kan word gebruik. Die beheerder se vermoë om fotovoltaïese inkorting te verminder word bevestig deur die prestasie van die betrokke beheerder in omstandighede eie aan elke seisoen van die jaar (wat strek van September 2017 tot Augustus 2018) in 'n simulasie-omgewing te toets, met 'n voorspellingshorison van een tot ses stappe.

Acknowledgements

This thesis would not have been possible without financial support from the National Research Foundation in the form of a Master's Degree Innovation Scholarship. I would therefore like to thank the Foundation, first and foremost.

A great many thanks also to Prof. Toit Mouton for his unwavering support, for affording me the freedom to explore widely, and his patience in advising me throughout the process of bringing it all together. I have grown a great deal under his tutelage. For this and much more I am immensely grateful.

Drs. Dominic Wills and Christopher Haw gave valuable feedback in shaping the project. I have learned a great deal through your involvement. Thank you.

My time in the Power Electronics Group would definitely not have been so much fun without each and every one of the students in the postgraduate lab. I wish you the best of luck with your research and the challenges you decide to take on thereafter. I would be remiss if I did not mention Tinus by name, however. I owe you many, many cans of Red Bull for all you've done in assisting me. Thank you.

My parents, André and Anita, and my brother, Nato, have provided support throughout my years of study and continued to do so over the past two years. I do not know where I would be without you.

I am particularly grateful for the support of my girlfriend, Tanja. Your sense of adventure, as well as your can-do attitude, has irrevocably enriched my life.

Lastly, I would like to express my appreciation for my grandmother, Susan, who has been a solid base of support for as long I can remember. Ons heldin, geklee in nederigheid.

Contents

List of Figures

List of Tables

Nomenclature

Notation

Scalar variables are written in italics (e.g. x). Matrices and vectors are written in bold italics (e.g. $\boldsymbol{A}$ and $\boldsymbol{x}$).

Index variables are denoted by i, j, k and l. Subscripts are written in Roman type (e.g. p_{gen}).

Dimensions for states and disturbances are described through use of n with accompanying subscripts, whereas control input dimensions are specified with m and accompanying subscripts.

The identity matrix of dimension $n \times n$ is written as $\mathbf{I}^n$. The zero matrix of dimension $n \times m$ is written as $\mathbf{0}^{n \times m}$. The set of real numbers of dimension n is written to $\mathbb{R}^n$.

Acronyms

AHU	air-handling unit
BES	battery energy storage
COP	coefficient of performance
EER	energy efficiency ratio
EWH	electric water heater
MPC	model predictive control
NOCT	nominal operating cell temperature
PV	photovoltaic
SoC	state of charge
SQP	sequential quadratic programming

Symbols

α	convection coefficient, unless stated otherwise
C	thermal capacity
c	specific heat, unless stated otherwise
c_{BES}	maximum theoretical battery charge rate
c_{C}	cooling coefficient
c_{H}	heating coefficient
$c_{\dot{\text{m}}}$	mass flow coefficient
c_{r}	recovery factor
c_{w}	charge-well factor
d	thickness
d_{BES}	maximum theoretical battery discharge rate
E	energy storage capacity
$\bar{f}$	average switching frequency
l_{b}	upper bound
η_{BES}	battery energy storage efficiency
$\eta_{\text{BES,ch}}$	battery energy storage charging efficiency
$\eta_{\text{BES,dis}}$	battery energy storage discharging efficiency
η_{total}	total battery energy storage efficiency
ξ	extra-nodal power requirement
$P_{\text{EWH,r}}$	electric water heater rated power
p_{gen}	variable generated power
p_{load}	variable load power
Q	stored energy
ρ	density
R_{λ}	specific thermal resistance
R	thermal resistance
T_{amb}	ambient temperature
T_{cell}	photovoltaic cell temperature
T_{in}	incoming water temperature
T_{s}	sampling period
u_{b}	upper bound
V_{EWH}	volume of electric water heater tank
V_{used}	volume of water used in a given sampling period
w_{f}	forcibly wasted power
w_{s}	standing power losses

Chapter 1

Introduction

Traditionally, household electrical infrastructure has been viewed as a connector between the electrical grid and energy-consuming devices on the premises. This one-way view of residential power flow is being challenged as the impact of fossil-fuel intensive methods of power generation are facing increased scrutiny [1].

Altering the role of households, towards enabling increased local as opposed to centralised generation, can have a sizeable positive impact on the nature of the modern electrical grid. For illustration, consider that the residential share of energy consumption amounts to roughly 24 % in the Netherlands [2], 28 % in South Africa [3] and 37 % in the United States of America [1].

Home energy management, defined as any means of providing consumers with feedback and/or control over their energy use, has generally been concerned with technologies that reduce consumption [4]. There exists, however, many opportunities to shift local electrical demand so as to lessen the overall strain on the electrical grid. Taking this idea one step further, if local generation and storage are available, the household could be able to meet a majority of its energy needs [5]. If applied broadly, this measure would result in decentralising power generation capacity and thereby yielding a more robust electrical grid.

1.1 The South African Context

In South Africa, higher-end and heavy-use domestic consumers of utility energy subsidise lower-income households. Consider Stellenbosch Municipality rates, as is shown in Figure 1.1. Residential properties valued at R200 000 or less pay a reduced Life Line Tariff. Properties above this threshold pay higher rates, mostly based on their energy consumption history. Residences that, on average, consumed 600 kWh or less prepaid electricity per month, in the previous financial year, pay higher per-unit costs than those that averaged above 600 kWh per month. The former, however, is exempt from a monthly base charge, while the latter is not. Regular residential consumers, not equipped with the prepaid facility, are subject to the same per-unit cost as prepaid residences with above-600 kWh

average monthly consumption, but are subject to a higher base rate still. Domestic properties equipped with solar photovoltaic (PV) arrays exclusively for own use fall under the same cost structure as regular residences, while those equipped to export power are charged an additional monthly reading cost. Appendix A lists the various Stellenbosch Municipality tariffs and charges, effective from 1 July 2018.

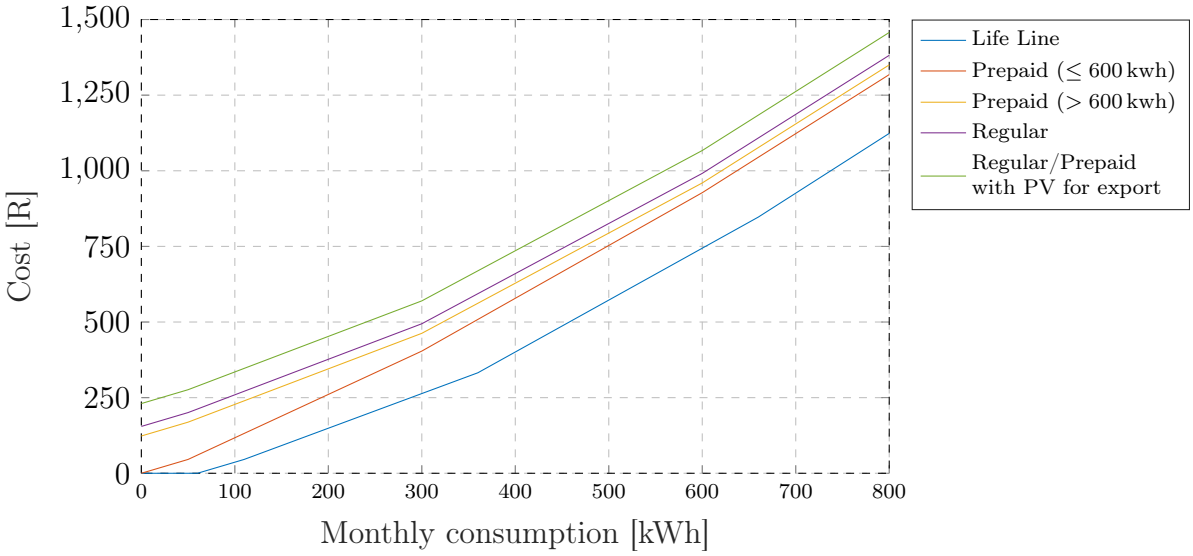

Figure 1.1: Stellenbosch Municipality domestic electrical tariff tiers compared. Residential properties equipped with solar PV arrays for own use and export fall under the most expensive scheme.

Additionally, export rates into the grid are all lower than the lowest-cost import rate from the grid (refer to Table A.2), with the exception of the high-season (winter) peak-time rate. Both the morning and evening peak periods, however, fall outside the time of day when the bulk of energy generation takes place. Similar rates apply in other metro areas, e.g. those of the City of Cape Town [6]. It can be concluded that there is little municipal incentive for residential PV installations to be biased towards exporting their generated power.

1.1.1 Eskom Rates Rise While Solar and Storage Costs Fall

A 2017 report [7], prepared by Deliotte for national power utility Eskom, anticipates materially higher energy rates in coming years. Calculated as expenditure per unit energy generated for a given year, the utility's cost of energy has steadily shot upward since 2007 (in real terms, using 2016 rands) [7, p. 40] . Due to a myriad reasons, Eskom is unable to provide electricity at pre-2007 levels. This is also evident from the Department of Energy's price report of 2017, which estimates that the cost per kilowatt-hour (averaged across all categories) jumped more than fourfold from the 2007/8 to the 2016/17 financial year. In the 2010–2017 period, an increase of 207 % is estimated [8, p. 34]. Additionally, the practice of rolling blackouts (commonly referred to as "load shedding") has been used in

recent years to lessen strain on the electrical grid.

Contrasted with the above, the falling prices of both PV panels and battery energy storage (BES) have made the prospect of decentralised power generation more attractive in recent years. The International Renewable Energy Agency provides recent figures on solar PV system costs, estimating a 68 % reduction worldwide, from \$4394/kW to \$1388/kW, during the 2010–2017 period [9, p. 42]. Bloomberg New Energy Finance estimates that the cost price of lithium-ion batteries fell 84 % in the same period, from \$1000/kWh in 2010 to \$162/kWh in 2017 [10, p. 7].

The cost of decentralised generation and storage remains sizeable and perhaps beyond the reach of many South African households. It does seems posed, however, to play a significant role in counteracting the uncertainties brought about by the national utility's challenges.

1.1.2 Decentralised Generation and Storage Coupled with Demand-Side Management

Many modern commercial buildings have building automation systems installed. Controlling blinds, lighting, and heating, ventilation and cooling often leads to material reductions in energy consumption within commercial contexts. Such systems are inexpensive to install in large buildings, but require many invasive sensors and actuators, the fixed costs of which dissuade residential use [11].

A system more limited in scope than what is conventionally understood by a building automation system could find widespread residential adoption. Within a household, the largest electrical load results from temperature regulation of air and water [12]. It is therefore reasonable to devise a demand-side management system which chiefly manipulates these temperature-regulation appliances to increase household self-sufficiency.

Shifting electrical load requires some knowledge of future conditions that will affect the load curve. When controlling temperature-regulating loads, this implies utilising estimated future temperatures (of air and water) to pro-actively take the best possible route in managing electrical load. When making use of highly-variable power sources, as solar radiation is, forecasts can lend much-needed stability to the power supply-demand balancing act. In this way, when solar energy generation is available the system can apply it to maximal benefit of the household and otherwise minimise the amount of energy required from the grid.

One school of control techniques ideally positioned to address the above aims is predictive control. A heterogeneous system, as the one described above, would necessarily be multivariate in nature, something predictive control is especially well-suited to address. The controller is defined in the time domain and can accommodate widely-varying, even contrasting, operational goals [13]. By making use of an objective function, these goals can be prioritised in order of importance. The controller acts accordingly, satisfying as

many of the specified goals as possible, while adhering to the system's limitations.

A predictive-control approach could thus make decentralised demand-side management of the sort described above feasible. Combined with models that accurately capture physical phenomena, a route to increased self-sufficiency for residences can be obtained.

1.2 Study Objectives

Within the context set out in the prior section, the study objectives are to:

- Describe a household power system comprised of regular loads and manipulable temperature-regulation appliances, in addition to a solar PV array and BES unit.
- Exert predictive control over the described system to reduce the amount of curtailed PV energy and thereby grid dependency, demonstrating that predictions farther ahead yield better results.
- Minimise the loss of thermal comfort (i.e. water and air temperatures outside of preferred ranges) in the pursuit of the second objective.

1.3 Thesis Summary

This thesis consists of five chapters, the content each is summarised below.

Chapter 1: Introduction provides the context within which the thesis is developed. Additionally, the general idea of the proposed solution is described. The chapter concludes by defining the thesis objectives, with the main focus placed on increasing the self-sufficiency of households through reduced PV curtailment, while minimising loss of comfort.

Chapter 2: Background motivates the model-based approach taken, and describes model predictive control (MPC) in terms of the two main approaches to its use in practice, the latter of which is used in this thesis. The chapter concludes by briefly discussing convexity, as this concept is foundational to the solution of optimisation problems (of which predictive control is but one application).

Chapter 3: System Description introduces the power node framework and defines a household power system, consisting of controllable and non-controllable power nodes. A suitable solar PV array is defined, and the diverse non-controllable load is described. Three controllable power nodes are defined and simulated, namely: a BES unit, an air-handling unit (AHU), and an electric water heater (EWH). The chapter concludes by combining all three controllable power nodes into a single state-space representation that

serves as the plant over which control is exerted.

Chapter 4: Predictive Control makes use of the system described in Chapter 3, along with the theoretical background provided in Chapter 2 to formulate a predictive control strategy. This includes the derivation of an objective function in the quadratic form, control-input reference generation focused on maximally allocating control inputs to reduce PV curtailment and the conversion of the formulated strategy into an implementable algorithm. The predictive controller is successfully tested in simulations across conditions typical of all four seasons, for prediction horizons one through six. The controller is shown to capable of reducing curtailed PV energy substantially.

Chapter 5: Conclusions and Recommendations draws the thesis to a close, reviewing the main contributions made and ends with select suggestions for follow-on research.

Chapter 2

Background

The theoretical background required for the thesis is provided here. The chosen modelling approach is described, the general MPC idea is explained, and convexity, an important aspect of the solution of optimisation problems is discussed.

2.1 Modelling Approach

Various approaches can be taken to model the various subsystems present in a household. Physics-based state-space representations are preferred in the present instance, as they can be combined into larger systems in a largely intuitive manner. Widely varying subsystems, each accurately modelling relevant phenomena in state-space representations, can be used in concert. Such models are easily used in tandem with predictive control schemes. Additionally, preference is given to models of low computational complexity (i.e. few parameters), while remaining reasonably accurate.

The work of Woon and Negnevitsky [14] provides reasonably accurate results, with relatively few parameters, and could be used within a state-space framework. More recent work [15], based in part on [14], is used as the basis of a suitable model of the EWH.

The OptiControl project at ETH Zurich provides thorough modelling of the thermal behaviour of buildings and the appliances acting in on the air within. A series of published research stems from the project [16] [17] [18], and is used as the foundation of the AHU model used in this work, as they describe physics-based state-space representations of low computational complexity.

A suitable BES model, meeting the desired requirements stated above, is required to represent the presence of energy storage within the household. Dualfoil [19] has for some time been the premier battery simulator, modelling a wide array of internal dynamics. While being the most accurate representation of physical phenomena within batteries, the model is computationally complex. Instead, a simplified model, presented in [20] and developed to closely approximate Dualfoil model's behaviour, is selected. The chosen model is of low computational complexity, while remaining reasonably accurate. Furthermore, it is described through means of a state-space representation.

2.1.1 Discretisation of Continuous-Time Models

With the exception of the EWH model, subsystems have to be discretised in order to be used within a discrete-time context. This is preferred over the continuous domain as it is easily used in practical environments (e.g. controlling a real-world system through means of a micro-controller), or when, as is the case here, simulating such environments.

The exact discretisation method [21, p. 106] is a standard technique within control engineering and is used in the present instance. Suppose the continuous-time state-space representation of a particular model is defined as

$$\dot{\boldsymbol{x}}(t) = \boldsymbol{A}_{\mathrm{c}}\boldsymbol{x}(t) + \boldsymbol{B}_{\mathrm{c}}\boldsymbol{u}(t), \tag{2.1}$$

where $\boldsymbol{x}$ is the state vector and $\boldsymbol{u}$ the control-input vector. Furthermore, $\boldsymbol{A}_{\mathrm{c}}$ and $\boldsymbol{B}_{\mathrm{c}}$ represent the continuous-time state and control-input matrix, respectively. The continuous-time representation can be discretised to yield its discrete-time equivalent, defined as

$$\boldsymbol{x}(k+1) = \boldsymbol{A}\boldsymbol{x}(k) + \boldsymbol{B}\boldsymbol{u}(k). \tag{2.2a}$$

The following definitions apply[1]:

$$\boldsymbol{A} = \boldsymbol{e}^{\boldsymbol{A}_{\mathrm{c}}T_{\mathrm{s}}} \tag{2.2b}$$

and

$$\boldsymbol{B} = \int_0^{T_{\mathrm{s}}} \boldsymbol{e}^{\boldsymbol{A}_{\mathrm{c}}\tau} d\tau \boldsymbol{B}_{\mathrm{c}}. \tag{2.2c}$$

If $\boldsymbol{A}_{\mathrm{c}}$ is invertible (i.e. non-singular), the following can be used in place of (2.2c):

$$\boldsymbol{B} = -\boldsymbol{A}_{\mathrm{c}}^{-1}(\mathbf{I} - \boldsymbol{A})\boldsymbol{B}_{\mathrm{c}}, \tag{2.2d}$$

with $\mathbf{I}$ taken as the identity matrix of appropriate dimensions.

2.2 Model Predictive Control

MPC is a specific kind of receding-horizon control, itself a popular process-control technique which concerns the solution of a finite-control problem at each time step of a system [13]. In this way, an infinite-horizon control problem is approximated through means of successive finite-horizon calculations. The solution is obtained by repeatedly solving an open-loop problem in short succession and applying the signal as input to a given system. This input signal is referred to as the control law. Where the control law is derived on-line (i.e. in real-time), making use of a receding-horizon policy, the technique is referred to as MPC. While initially developed to address control challenges in the process industry, the technique has since found widespread application elsewhere [22].

[1] Note that '$\boldsymbol{e}$' (as used in (2.2b) and elsewhere) represents the matrix exponent, as opposed to the element-wise exponent.

MPC is formulated entirely within the time domain, as opposed to the frequency domain. This allows for greater accommodation of systems that are non-linear, multiple-input multiple-output, and/or constrained in nature. The controller operates on the basis of manipulating a dynamic model, which non-linearities easily form part of. Furthermore, multiple cascading single-input single-output control loops are not required, since MPC is a multivariate control method. Constraints, even if in conflict, can be imposed on the controller and prioritised through means of an objective function. Viewed this way, the controller is an amalgamation of multiple control modes [23].

2.2.1 Dynamic Model

Define the discrete-time state-space representation of a generic system as

$$\boldsymbol{x}(k+1) = g(\boldsymbol{x}(k), \boldsymbol{u}(k)), \tag{2.3}$$

where $\boldsymbol{x}(k)$ is the state vector at time step k and $\boldsymbol{u}(k)$ its control-input vector. The state at the next time step is a function g of the present state, as shown.

2.2.2 Constraints

Limitations on the allowable range of both $\boldsymbol{x}$ and $\boldsymbol{u}$ above can be imposed by simply specifying the desired range. This constraint set is then used within the optimisation procedure. There are two kinds of constraints acting in on a given system: hard and soft constraints. The former is normally a consequence of the physical characteristics of the system (e.g. the maximum possible discharge power of a battery), while the latter can be disregarded when adherence to them result in an infeasible solution (e.g. desired water temperature level that the system is physically unable to be reach).

Constraints on $\boldsymbol{x}(k+1)$ are in fact a function of $\boldsymbol{x}(k)$ and $\boldsymbol{u}(k)$, and can be defined as[2]

$$g(\boldsymbol{x}_k, \boldsymbol{u}_k) \in \mathcal{X}, \tag{2.4}$$

which states that $\boldsymbol{x}(k+1)$ has to belong to allowable-state set $\mathcal{X}$. Constraints can also be applied to the entries of $\boldsymbol{u}$ in sets of one or more inequalities, that is,

$$\boldsymbol{C}\boldsymbol{u}_k \leq \boldsymbol{0}, \tag{2.5}$$

where $\boldsymbol{C}$ contains coefficients applicable to the entries of $\boldsymbol{u}$ and $\boldsymbol{0}$ is the zero vector of appropriate size.

[2] A note on notation: in (2.6) and elsewhere, the use of subscripts k and l (e.g. $\boldsymbol{x}_l$) imply predicted values, whereas standard notation (e.g. $\boldsymbol{x}(k)$) implies measured or set (and thus known) values.

2.2.3 Objective Function

The general form of the objective function J at time step k is

$$J_{k\to N}(\boldsymbol{x}(k), \boldsymbol{U}(k)) = \sum_{l=k}^{N+k-1} q(\boldsymbol{x}_l, \boldsymbol{u}_l). \tag{2.6}$$

Scalar $q(\boldsymbol{x}_l, \boldsymbol{u}_l)$ represents the stage cost at step l and N the prediction horizon (as measured in number of steps ahead), where q consists of one or more weighting functions. Vector $\boldsymbol{U}(k)$ groups together the sequence of control-input vectors over prediction horizon N, i.e.

$$\boldsymbol{U}(k) = \begin{bmatrix} \boldsymbol{u}_k^{\mathrm{T}} & \boldsymbol{u}_{k+1}^{\mathrm{T}} & \cdots & \boldsymbol{u}_{k+N-1}^{\mathrm{T}} \end{bmatrix}^{\mathrm{T}}. \tag{2.7}$$

2.2.4 Optimisation Procedure

The objective function is minimised at every time step, subject to specified constraints. There are two main methods of solving this minimisation problem: the recursive and batch approach. Both are discussed here, with the latter used as part of a control scheme in Chapter 4.

Recursive Approach

Often, a specific final state is desired. In these instances, the recursive approach to MPC is used, which makes use of Bellman's principle of optimality: for a given optimal-state trajectory, an intermediate trajectory must also be optimal [13, p. 150]. This is used to break up an optimisation problem into smaller, successive sub-problems. The recursive approach is also referred to as dynamic programming.

Starting from the final-state cost $p(\boldsymbol{x}_{k+N})$ and state constraint $\mathcal{X}_F$, that is,

$$J^*_{k+N\to k+N}(\boldsymbol{x}_{k+N}) = p(\boldsymbol{x}_{k+N}) \tag{2.8a}$$

and

$$\mathcal{X}_{k+N\to k+N} = \mathcal{X}_F, \tag{2.8b}$$

the optimal path is obtained by working backwards, i.e.

$$\begin{aligned} J^*_{k+N-1\to k+N}(\boldsymbol{x}_{k+N-1}) = \min_{\boldsymbol{u}_{N-1}} \; & q(\boldsymbol{x}_{k+N-1}) + J^*_{k+N\to k+N}(\boldsymbol{x}_{k+N}) \\ \text{subject to } & \boldsymbol{C}\boldsymbol{u}_{k+N-1} \leq \boldsymbol{0}, \\ & g(\boldsymbol{x}_{k+N-1}, \boldsymbol{u}_{k+N-1}) \in \mathcal{X}_{k+N\to k+N} \\ & \vdots \\ J^*_{k\to k+N}(\boldsymbol{x}_k) = \min_{\boldsymbol{u}_k} \; & q(\boldsymbol{x}_k) + J^*_{k\to k+N}(\boldsymbol{x}_k) \\ \text{subject to } & \boldsymbol{C}\boldsymbol{u}_k \leq \boldsymbol{0}, \\ & g(\boldsymbol{x}_k, \boldsymbol{u}_k) \in \mathcal{X}_{k\to k+N}, \\ & \boldsymbol{x}_k = \boldsymbol{x}(k). \end{aligned} \tag{2.9}$$

As used above, J^* represents the optimal value of J.

Batch Approach

When no particular final state is desired, the batch approach is used: calculate the least-cost path so long as the solution adheres to specified constraints, regardless of what the end state may be. Often times a reference state is known, but there exists a trade-off that prohibits excessive control-input effort (a finite amount of power, for example). If the entirety of the future is known, an optimal path could be obtained that would adhere to specific constraints and yield the lowest-cost path possible. In practice, at least two hurdles arise: First, the system model can approximate actual dynamics sufficiently accurate in the near term, but deviation from actual behaviour compounds over a longer time frame, causing the input sequence calculated to cease bearing relevance to the system. Secondly, the computational burden of calculating the optimal input sequence tends to grow quickly as the horizon over which the optimisation takes place is increased.

Instead, a finite N-step ("batch") solution is applied to the system with the aim that, with sufficient foresight, a noticeable improvement in control performance can be observed. An analogy used to describe the appeal of this approach is that of driving a car along a winding road: while the driver may not know the route to be driven in its entirety, knowledge of the short-term future allows for control actions to be taken that allow for a more efficient use of fuel (fewer stops and starts, smoother turning, etc.).

The batch-approach optimisation problem can be stated as

$$\begin{aligned} J^*_{k\to k+N}(\boldsymbol{x}(k), \boldsymbol{U}(k)) = \min_{\boldsymbol{U}(k)} \; & J(\boldsymbol{x}(k), \boldsymbol{U}(k)) \\ \text{subject to } & \boldsymbol{C}\boldsymbol{u}_k \leq \boldsymbol{0}, \\ & g(\boldsymbol{x}_k, \boldsymbol{u}_k) \in \mathcal{X}_{k\to k+N}. \end{aligned} \tag{2.10}$$

In subsequent chapters the relaxed notation $J(k)$ is used, instead of the strict $J_{k\to k+N}(\boldsymbol{x}(k), \boldsymbol{U}(k))$

notation.

2.2.5 Receding-Horizon Policy

Figure 2.1 depicts the working of the batch approach for a single-input, single-output system with state x and control input u, as an illustration of the receding-horizon concept. At time step k a control-input sequence is calculated, of which only the first entry, $u(k)$, is applied. At the next time step, the process is repeated. A more efficient route, requiring less input effort, is found by looking ahead and taking proactive steps to guide the trajectory toward the lower-cost route. This procedure constitutes a receding-horizon policy.

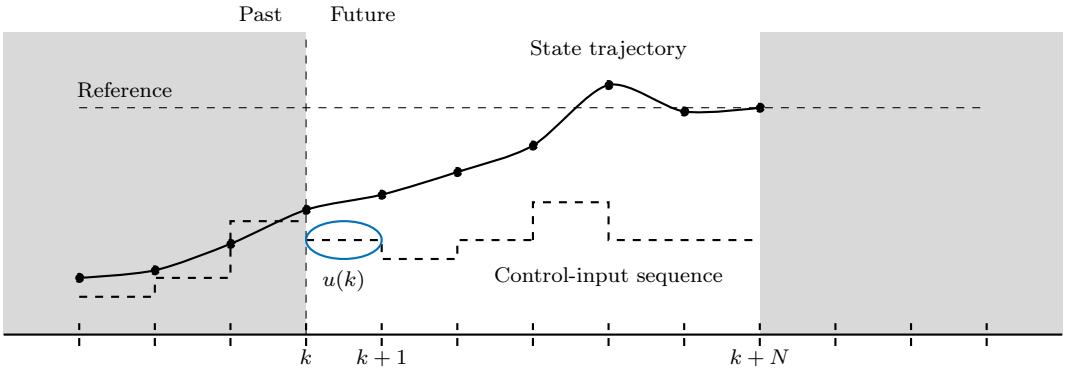

(a) The system state and control input at time k.

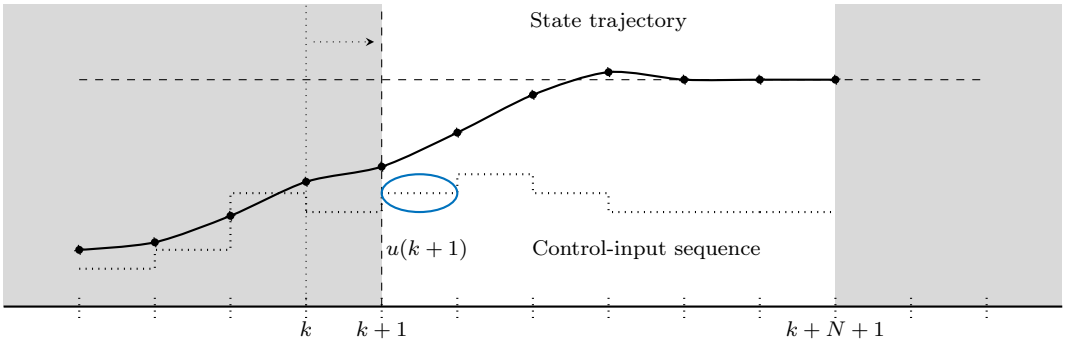

(b) The system state and control input at time $k+1$.

Figure 2.1: An example batch-approach state trajectory and control-input sequence, based on [13, p. 244].

2.3 Quadratic Programme Convexity

Equations in the quadratic form are often used as objective functions in optimisation procedures (because it is mathematically convenient), generally defined as [13, p. 39]

$$J = \frac{1}{2}\boldsymbol{z}^{\mathrm{T}}\boldsymbol{H}\boldsymbol{z} + \boldsymbol{q}^{\mathrm{T}}\boldsymbol{z}, \tag{2.11}$$

where $\boldsymbol{z}$ is the vector to be optimised, $\boldsymbol{H}$ is referred to as the Hessian matrix [24, p. 626], and $\boldsymbol{q}$ is the linear cost vector. A global optimizer (the single most-suitable $\boldsymbol{z}$ across its entire range) is preferred over a local optimizer (the most-suitable $\boldsymbol{z}$ in a small range). Optimisation problems for which any local optimizer is also considered to be a global optimizer are said to be 'convex'. The globally optimal $\boldsymbol{z}$, $\boldsymbol{z}^*$, for an unconstrained problem is defined as

$$\boldsymbol{z}^* = -\boldsymbol{H}^{-1}\boldsymbol{q}. \tag{2.12}$$

In these cases, the Hessian $\boldsymbol{H}$ is said to be positive definite and the global optimizer is unique. There exist cases where $\boldsymbol{H}$ is singular (i.e. non-invertible), the implication being that there are multiple global optimizers, for which the unconstrained optimizer(s) can be found from

$$\boldsymbol{H}\boldsymbol{z}^* = -\boldsymbol{q}. \tag{2.13}$$

Here, the Hessian allows for a convex optimisation problem, but, since it is singular, the Hessian is said to be positive semi-definite. This is the minimum condition necessary in order for the problem to be reliably optimised.

2.4 Summary

Chapter 2 discusses underlying theory applicable to later chapters of the thesis. The preferred modelling approach is expanded upon, a specific predictive control method is described, and the definition of convex quadratic programmes, applicable to the implementation of predictive control, is provided.

Chapter 3

System Description

This chapter describes a framework to reconcile heterogeneous electrical entities within a power system. Descriptions of a number of such entities are supplied. Lastly, a sample system, featuring each of the described entities, is proposed for use within a control framework.

3.1 Electrical Entities as Power Nodes

Electrical entities within a power system can be divided into three groups: generators, loads, or storage devices. These entities interact through electrical energy transfer, where a conversion to other types (e.g. chemical, kinetic, light, or thermal) of energy can take place. Electrical entities can differ a great deal from one another. By focusing, instead, on commonalities between them, a framework can be formed within which each entity is sufficiently described. In this way, a heterogeneous set of generators, loads, and storage devices can be characterised by a homogeneous set of properties.

A framework of this sort can be used to gain an understanding of the present state of the power system. This includes the ability to identify opportunities where generators' excess can be assigned to candidate loads in an optimal manner. (More is said on this subject in Chapter 4.)

One such approach views electrical entities as power nodes [25], whereby each entity can be described by a number of properties. Generation and load power p_{gen} and p_{load}, respectively, describe the node's activity at a given point in time. Energy storage capacity E describes the node's ability to store energy in absolute terms, e.g. charge (as opposed to relative terms, e.g. water temperature relative to ambient temperature), if the node is indeed capable of doing so. If a node can store electrical charge, level x describes the percentage of total capacity filled at a given point in time. External requirement ξ describes rigid demand power the node requires (with a permitted range of $\xi \leq 0$) or supply power it produces (with a permitted range of $\xi \geq 0$) at a given point in time. Nodes with $\xi = 0$ are controllable, and nodes with non-zero ξ are non-controllable. Forced waste w_{f} (applicable to nodes with non-zero ξ) describes the degree to which ξ for a given node

is unfulfilled at a given point in time. Standing loss w_s (applicable to storage devices) describes losses incurred due to the internal operations of a storage device. A summary of all power node properties, adapted for the present use-case from [25], can be found in Table 3.1.

Table 3.1: Properties of a Generic Power Node

Property		State	Implication
p_{gen}	[W]	$p_{gen} \geq 0$	Generator
p_{load}	[W]	$p_{load} \geq 0$	Load
		$p_{gen} \geq 0$ & $p_{load} \geq 0$	Storage device
E	[Wh]	$E = 0$	No energy storage capacity
		$E > 0$	Energy storage present
x	[p.u.]	$0 \leq x \leq 1$	Storage capacity filled
ξ	[W]	$\xi \leq 0$	Uncontrollable demand
		$\xi = 0$	Controllable
		$\xi \geq 0$	Uncontrollable supply
w_f	[W]	$w_f < 0$	Unmet load
		$w_f > 0$	Curtailed generated energy
w_s	[W]	$w_s = 0$	Lossless storage
		$w_s > 0$	Standing losses present

A graphical depiction of a generic power node, including all described properties, is shown in Figure 3.1.

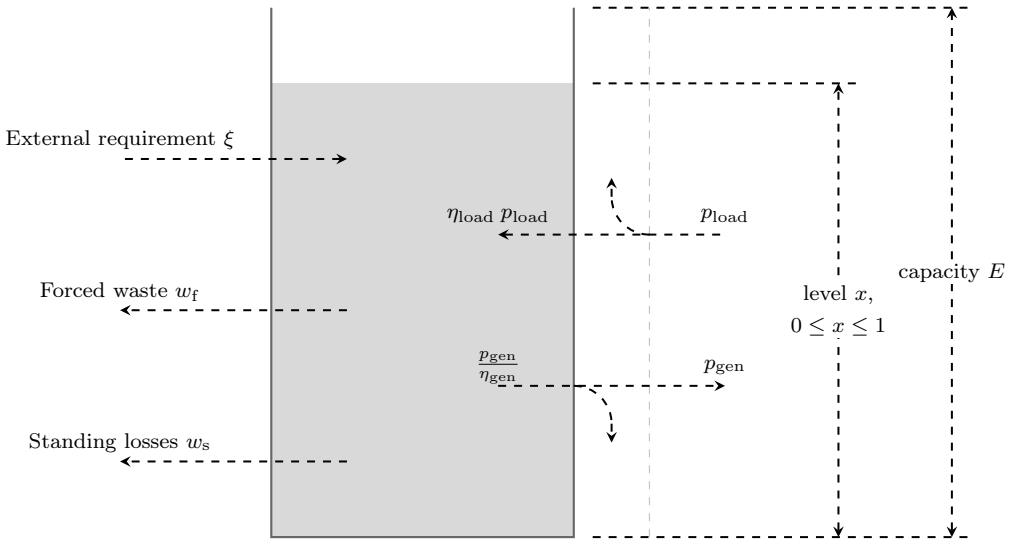

Figure 3.1: A generic power node.

A sample system is simulated using the power-nodes framework. Figure 3.2 depicts the electrical bus of said system. The nodes highlighted in blue are of particular interest. Under a control regime, each of these subsystems can be manipulated so that the PV

array's productivity, defined as the percentage of potential generation utilised, can be maximised.

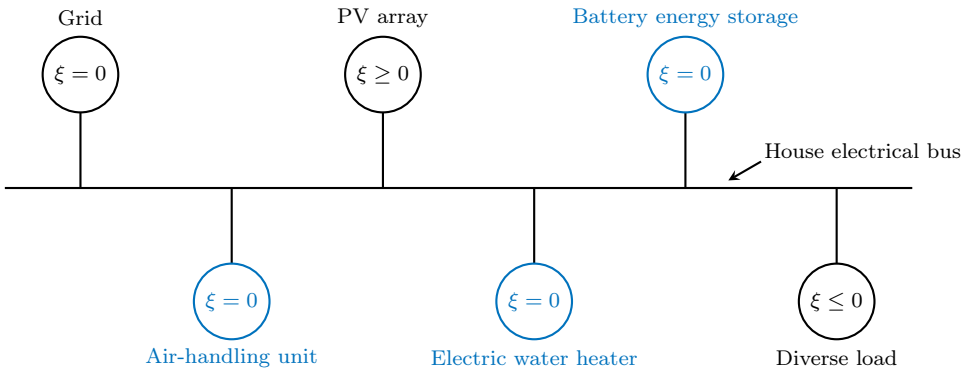

Figure 3.2: The sample system.

Incoming grid power, pictured above, is also considered controllable. Its power contribution at any given time step is calculated to be the amount of supply power which cannot be provided by some combination of the BES and PV array.

Optimising the scheduling of blue power nodes (in Figure 3.2), so that the household is supplied by the PV array and BES unit as far as possible, is considered to be the most valuable contribution the proposed energy management system can make. Further sections in this chapter describe parts of the system, as a precursor to exercising control over the system as a whole (the subject of Chapter 4).

3.2 Uncontrollable Nodes

In this section, entities with either $\xi \leq 0$ or $\xi \geq 0$, that is, over which no meaningful control can be exerted, are described. Two entities are of interest in the present case: a PV array, and a number of household appliances (referred to collectively as the diverse load). Load-power data from a real-world system gathered from 1 September 2017 to 31 August 2018 are used as the diverse load. Gathered data points are 10 min apart, where power measurements represent average power.

3.2.1 Photovoltaic Array

Optimal sizing of the solar PV array is not the subject of the present study, but an installation of reasonable size is to be used. This section describes the process by which such an installation is obtained.

Suppose the PV array is to yield 6500 kWh of energy annually, an arbitrary choice. The Stellenbosch region has an estimated 1826 h of full-sun conditions, annually [26]. Represent reticulation-wiring losses, dirt, and module mismatch with a derate factor of

0.88 [27]. When combined, this results in a required array size [27, p. 336] of

$$P_{\text{dc}} = \frac{6500\,\text{kWh/yr}}{(0.88)(1826\,\text{h/yr})} = 4.05\,\text{kW}. \tag{3.1}$$

Canadian Solar 290MS-SD (290 W) PV modules [28] are used for the simulated array. A total of $4.05/0.29 = 13.97 \approx 14$ panels would be required. Suppose an SMA Sunny Boy 4000TL-21 [29] is selected as solar inverter of choice. A single 14-panel string would fall in the inverter's maximum-power point range. The validity of this arrangement is confirmed below.

Temperature data recorded on the engineering faculty's roof over the course of the last decade report a maximum temperature of 41.83 °C and a minimum of 0 °C [30]. Along with the specifications listed in Table 3.2, this leads to maximum and minimum panel and string voltages as follows: Maximum panel voltage is calculated, making use of the difference between standard testing-conditions and the expected minimum temperature, as

$$32.1\big(1 - 0.0031(0 - 25)\big) = 34.59\,\text{V}, \tag{3.2}$$

and therefore a maximum string voltage of 484.26 V is obtained (the panel resides at ambient temperature in cold conditions). On hotter days, the panel temperature is estimated using [27, p. 338]

$$T_{\text{cell}} = T_{\text{amb}} + \left(\frac{\text{NOCT} - 20}{0.8}\right) S, \tag{3.3}$$

where insolation S is taken as $1\,\text{kW/m}^2\text{/day}$. This results in a maximum cell temperature of 73.08 °C and a minimum panel voltage of

$$32.2\big(1 - 0.0031(73.08 - 25)\big) = 27.32\,\text{V}. \tag{3.4}$$

The corresponding string voltage is 382.48 V. Both the minimum and maximum string voltages fall within the allowable range of the solar inverter's maximum-power point tracker. This confirms the validity of the 14-panel string arrangement.

Table 3.2: Selected specifications

Specification	Value	Units
Canadian Solar 290MS-SD		
Short-circuit current	15	A
Rated voltage	32.1	V
Temperature coefficient	-0.31	%/K
Nominal operating cell temperature (NOCT)	45	°C
SMA Sunny Boy 3600TL-21		
Allowable short-circuit current	20	A
Maximum-power point range	175–500	V
Standard testing-conditions temperature	25	°C

Global horizontal irradiation [31] data gathered on the rooftop of Stellenbosch University's engineering faculty from the start of September 2017 to the end of August 2018, downloaded from Southern African Universities Radiometric Network (SAURAN) [32], are used to represent radiation falling in on the simulated flat-panel (0° tilt) solar PV array. A sample of this dataset is shown in Figure 3.3, which depicts the solar inverter's output power for 1–7 October 2017. Over the selected sample period, a total of 87.82 kWh is output by the solar inverter.

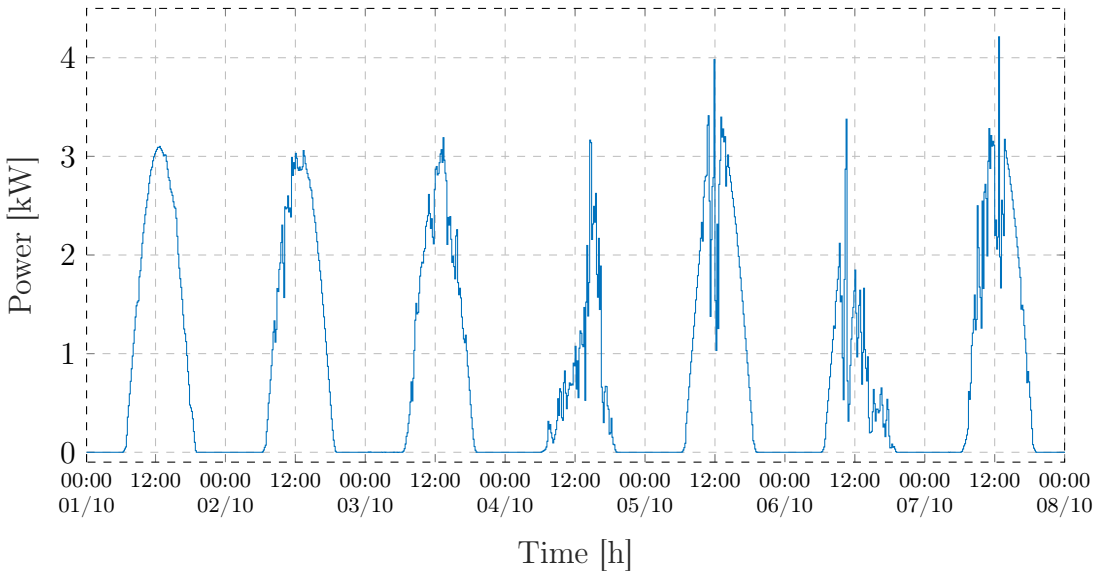

Figure 3.3: PV inverter output power during the 1–7 October 2017 period.

3.2.2 Diverse Load

Household power consumption data, recorded from September 2017 through August 2018, for a number of appliances (devices plugged into power outlets, stove, etc.) comprise the system's uncontrollable load (i.e. $\xi \leq 0$) power node. A sample of this dataset is shown in Figure 3.4, which depicts the diverse load's power consumption for 1–7 October 2017.

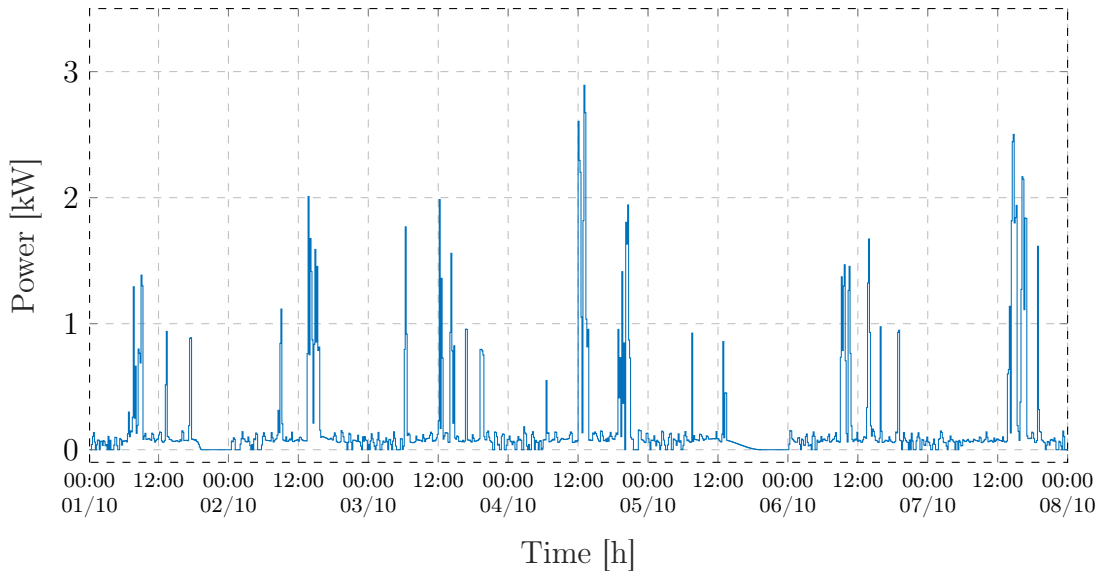

Figure 3.4: Diverse load power consumption during the 1–7 October 2017 period.

Over the course of the selected period, a total of 30.47 kWh is consumed by the system's diverse load.

3.3 Selected Controllable Nodes

Three controllable electrical entities are described in this section: a BES model, which is continuously controllable (0–100 %), as well as AHU and EWH models, both of which are controllable on an integer basis (i.e. 'on/off') . The discretisation sampling period T_s is taken to be 10 min.

3.3.1 Battery Energy Storage

In this section, the chosen battery model, based on [20], is described and simulated.

Model Description

A visual depiction of the working of the BES model is provided in Figure 3.5. Charge-well factor c_w [%] models the distribution of energy, which is stored throughout the battery and not available in its entirety at a moment's notice. Instead, only the available well, denoted by $x_{BES,1}(k)$ [p.u.], is immediately available.

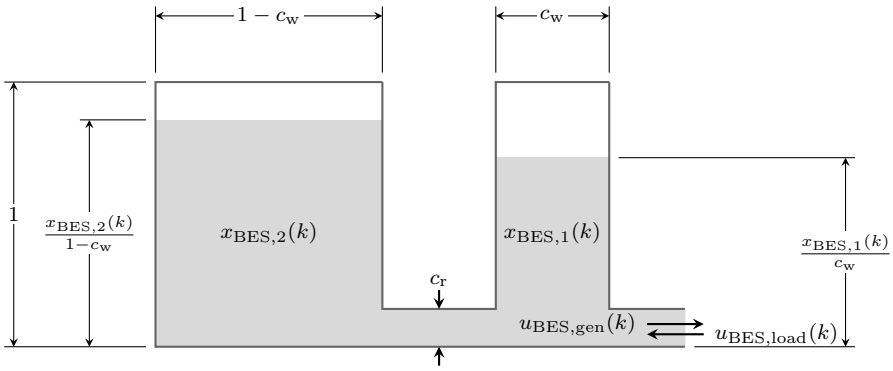

Figure 3.5: Visual depiction of the battery energy storage model, which models the rate-capacity effect [20].

Energy flows through from the reserve (denoted as $x_{\text{BES},2}(k)$ [p.u.]) to the available well at a rate determined by recovery factor c_r [s^{-1}]. This phenomenon is referred to as the rate-capacity effect: at higher operating rates of charge or discharge, the usable battery capacity is reduced. The rate-capacity effect models these bottlenecks in the flow of charge by representing the battery as two charge wells.

In the charge state, for example, once the available well reaches capacity, the flow of current into the battery is limited to the maximum allowable flow of charge between the charge wells. Leaving the battery inactive, referred to as 'relaxing' the battery, after use allows for energy to redistribute between the wells at a given point in time.

The BES state of charge (SoC) is the sum of its charge two charge wells. The battery state vector is thus

$$\boldsymbol{x}_{\text{BES}}(k) = \begin{bmatrix} x_{\text{BES},1}(k) \\ x_{\text{BES},2}(k) \end{bmatrix}. \tag{3.5}$$

The state-space representation describing the battery SoC [20] is

$$\boldsymbol{x}_{\text{BES}}(k+1) = \boldsymbol{A}_{\text{BES}}\boldsymbol{x}_{\text{BES}}(k) + \boldsymbol{B}_{\text{BES}}\boldsymbol{u}_{\text{BES}}(k) \text{ [p.u.]}, \tag{3.6}$$

where $\boldsymbol{x}_{\text{BES}}$ and $\boldsymbol{u}_{\text{BES}}$ are the battery's state and control-input vector, respectively.

The battery control-input vector is defined as

$$\boldsymbol{u}_{\text{BES}}(k) = \begin{bmatrix} u_{\text{BES,gen}}(k) \\ u_{\text{BES,load}}(k) \end{bmatrix}, \tag{3.7}$$

where

$$u_{\text{BES,gen}}(k) \in [0, 1] \text{ and } u_{\text{BES,load}}(k) \in [-1, 0].$$

(The battery control inputs are assumed to be continuous in nature.)

To incorporate the factors described earlier, state matrix $\boldsymbol{A}_{\text{BES,c}}$ can be defined (in

the continuous-time domain) as [20]

$$\boldsymbol{A}_{\mathrm{BES,c}} = \begin{bmatrix} -\frac{c_\mathrm{r}}{c_\mathrm{w}} & \frac{c_\mathrm{r}}{1-c_\mathrm{w}} \\ \frac{c_\mathrm{r}}{c_\mathrm{w}} & -\frac{c_\mathrm{r}}{1-c_\mathrm{w}} \end{bmatrix}. \tag{3.8}$$

Furthermore, [20, p. 18] shows that a single efficiency, η_{BES}, can be used for both charge and discharge states, that is,

$$\eta_{\mathrm{BES,ch}} \approx \eta_{\mathrm{BES,dis}} = \eta_{\mathrm{BES}}. \tag{3.9}$$

Assume that the battery converter has efficiency η_{conv}. Take η_{total} as the product of η_{BES} and η_{conv}. This yields the input matrix

$$\boldsymbol{B}_{\mathrm{BES,c}} = \begin{bmatrix} -\frac{1}{\eta_{\mathrm{total}}} & -\eta_{\mathrm{total}} \\ 0 & 0 \end{bmatrix}. \tag{3.10}$$

Both $\boldsymbol{A}_{\mathrm{BES,c}}$ and $\boldsymbol{B}_{\mathrm{BES,c}}$ are discretised, using the exact-discretisation method described in Chapter 2, before use within the simulated system, as the simulation is done in discrete time. Their discete-time representations will be referred to similarly, but without the 'c' subscript. The discrete-time state and control-input matrices are calculated as follows:

$$\boldsymbol{A}_{\mathrm{BES}} = \boldsymbol{e}^{\boldsymbol{A}_{\mathrm{BES,c}} T_\mathrm{s}}. \tag{3.11a}$$

The discretised matrix $\boldsymbol{B}_{\mathrm{BES}}$ is additionally normalised to its per-unit representation, the preferred notation when describing electrical systems subject to size variability. Rated power $P_{\mathrm{BES,r}}$ [W] and rated storage capacity $E_{\mathrm{BES,r}}$ [Wh] are used to convert the matrix to its per-unit equivalent, as shown below:

$$\boldsymbol{B}_{\mathrm{BES}} = \left(\frac{P_{\mathrm{BES,r}}}{E_{\mathrm{BES,r}}}\right) \int_0^{T_\mathrm{s}} \boldsymbol{e}^{\boldsymbol{A}_{\mathrm{BES,c}}\tau} d\tau \; \boldsymbol{B}_{\mathrm{BES,c}}. \tag{3.11b}$$

For the sake of generality, dimensions of the BES state-space model are defined as

$$\boldsymbol{x}_{\mathrm{BES}}(k) \in \mathbb{R}^{n_{\mathrm{BES}}}, \boldsymbol{u}_{\mathrm{BES}}(k) \in \mathbb{R}^{m_{\mathrm{BES}}}, \boldsymbol{A}_{\mathrm{BES}} \in \mathbb{R}^{n_{\mathrm{BES}} \times n_{\mathrm{BES}}}, \boldsymbol{B}_{\mathrm{BES}} \in \mathbb{R}^{n_{\mathrm{BES}} \times m_{\mathrm{BES}}},$$

where $\mathbb{R}$ refers to real space and its superscript denoting the dimensions of the matrix or vector.

BES Test Simulation

The simulated battery makes use of the Tesla Powerwall 2's specifications [33]. Energy capacity E_{BES} is chosen as 13.5 kWh, with a maximum continuous power rating of 5 kW (for both charge and discharge) at an efficiency η_{total} of 95 %; Charge well $x_{\mathrm{BES},1}$ stores a

maximum of 15 % of battery capacity (thus $c_w = 0.15$), with the remaining 85 % stored in $x_{BES,2}$; recovery factor c_r is taken to be $1 \times 10^{-3} s^{-1}$ [20]. No standing losses are taken into consideration.

Figure 3.6 shows the modelled battery cycled from a fully charged state to depletion and back again (Figure 3.6a). The rate-capacity effect can be observed in both charge and discharge states. As the available well ($x_{BES,1}$) is depleted, the rate at which energy is redistributed from the reserve well ($x_{BES,2}$) is lower than rated discharge power (Figure 3.6b).

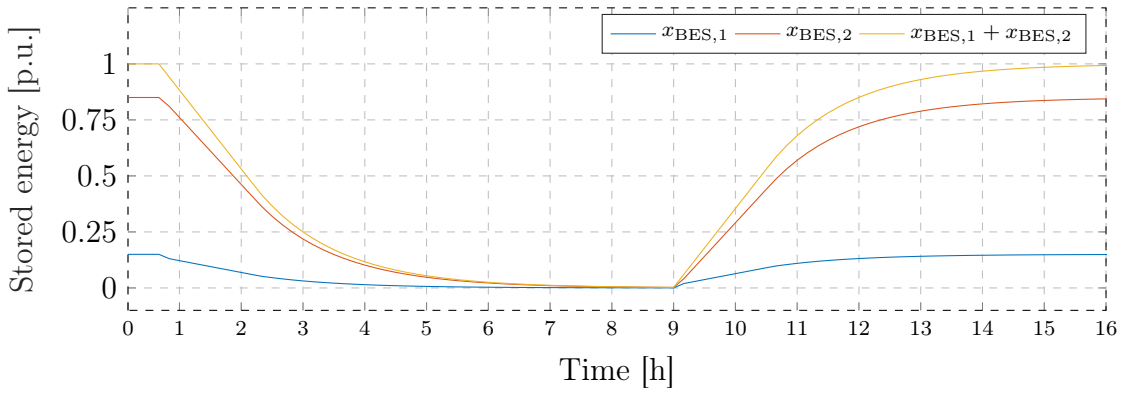

(a) Stored energy.

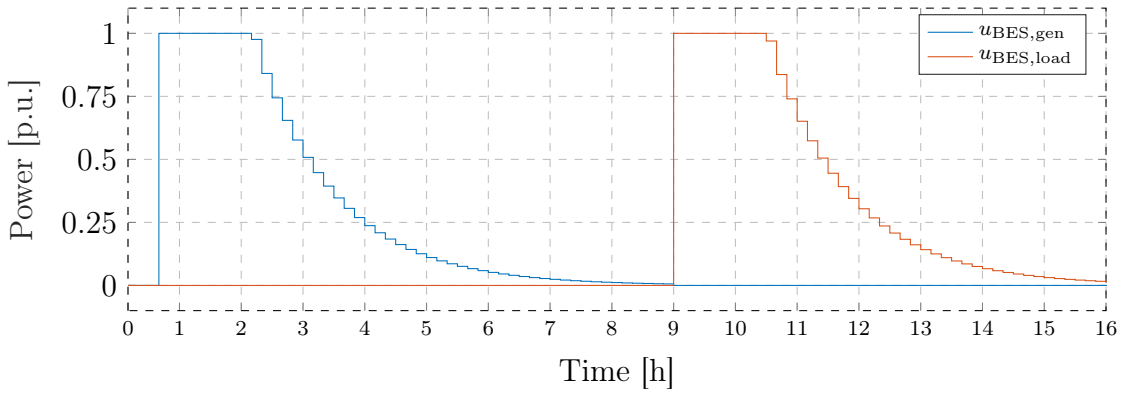

(b) BES generation and load power during the test simulation.

Figure 3.6: BES test simulation stored energy, and generation and load power.

Although the battery, in its entirety, hypothetically contains the amount of charge required to discharge at maximum capacity, due to the bottleneck in flow of charge, lower discharge power is observed. The inverse process can also be observed.

3.3.2 Air-Handling Unit

This section describes the room thermal model and AHU in terms of its states, control input, and disturbances acting in on the room. The room's thermal characteristics are described, as well as those of two heat fluxes. A heat flux is a mechanism through which heat energy is transferred per unit area per unit time, specifically, to/from the room or

any of its building elements' surfaces. Applicable heat fluxes are the passive interaction with the surrounding ambient air and the active interaction with the AHU itself. The model used is based on [17] and [18]. Note that it is assumed that only integer control can be exercised over the AHU, i.e. an 'on' or 'off' command.

Characterisation of the Simulated Room

A single simulated room is considered. It is assumed to be a four-walled room, with no windows through which solar radiation can enter the room.

The room is made up out of various components, namely: the air within the room (referred to as the 'zone'), as well as its four surrounding walls, the ceiling, and floor, referred to as building elements one to four, five, and six, respectively. The zone and building temperatures are grouped together in the AHU state vector $\boldsymbol{x}_{\text{AHU}}(k)$, i.e.

$$\boldsymbol{x}_{\text{AHU}}(k) = \begin{bmatrix} x_{\text{Z}}(k) & x_{\text{BE},1}(k) & \cdots & x_{\text{BE},6}(k) \end{bmatrix}^{\text{T}} \in \mathbb{R}^{n_{\text{Z}}+n_{\text{BE}}} \text{ [°C]}. \tag{3.12}$$

Both n_{Z} and n_{BE} are defined for the sake of generality. Additionally, $n_{\text{AHU}} = n_{\text{Z}} + n_{\text{BE}}$.

The simulated room is depicted in Figure 3.7.

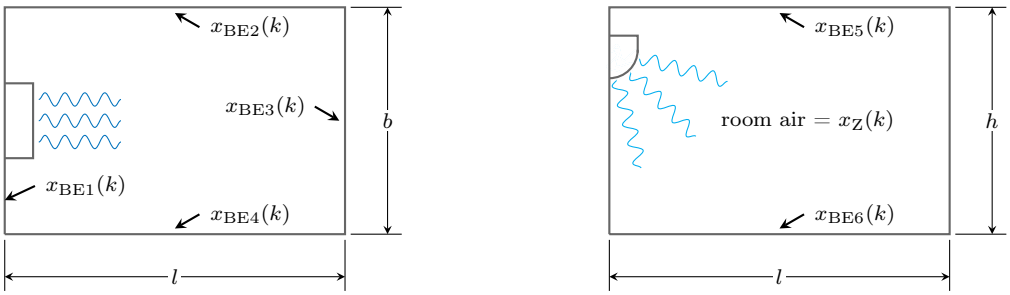

(a) Top view. (b) Side view.

Figure 3.7: Depiction of the simulated room. All monitored states are visible. Heat exchange can take place between the room air and walls, as well as each of the walls and the surrounding ambient air.

The AHU state-space model is summarised as:

$$\boldsymbol{x}_{\text{AHU}}(k+1) = \boldsymbol{A}_{\text{AHU}}\boldsymbol{x}_{\text{AHU}}(k) + \boldsymbol{B}_{\text{AHU},u}(k)u_{\text{AHU}}(k) + \boldsymbol{B}_{\text{AHU},v}\boldsymbol{v}_{\text{AHU}}(k) \text{ [°C]}, \tag{3.13a}$$

where $\boldsymbol{A}_{\text{AHU}}$ is the AHU state matrix, and $\boldsymbol{B}_{\text{AHU},v}$ its disturbance-input matrix. Its time-varying control-input matrix $\boldsymbol{B}_{\text{AHU},u}(k)$ is defined as

$$\boldsymbol{B}_{\text{AHU},u}(k) = \Big(\boldsymbol{B}_{\text{AHU},u} + \big(\boldsymbol{B}_{\text{AHU},xu}\boldsymbol{x}_{\text{AHU}}(k) + \boldsymbol{B}_{\text{AHU},vu}\boldsymbol{v}_{\text{AHU}}(k)\big)\tilde{\boldsymbol{1}}^{\text{T}}_{\text{AHU},u}\Big)\boldsymbol{c}_{\text{AHU}}(k), \tag{3.13b}$$

where $\boldsymbol{B}_{\text{AHU},u}$ is the time-invariant control-input matrix, $\boldsymbol{B}_{\text{AHU},xu}$ its state-control input matrix, $\boldsymbol{B}_{\text{AHU},vu}$ its disturbance-control input matrix, and $\boldsymbol{c}_{\text{AHU}}(k)$ its conversion vector.

Lastly,

$$\tilde{\mathbf{1}}_{\mathrm{AHU},u} = \begin{bmatrix} 1 & 0 & 0 \end{bmatrix}^{\mathrm{T}}. \tag{3.13c}$$

The disturbance-input vector $\boldsymbol{v}_{\mathrm{AHU}}(k)$ consists of ambient-temperature scalars acting in on each of the external walls of the room, i.e.

$$\boldsymbol{v}_{\mathrm{AHU}}(k) = \begin{bmatrix} 0 & T_{\mathrm{amb}}(k) & \cdots & T_{\mathrm{amb}}(k) & 0 & 0 \end{bmatrix}^{\mathrm{T}} \in \mathbb{R}^{n_{\mathrm{AHU}}}. \tag{3.14}$$

Temperature data downloaded from the Southern African Universities Radiometric Network (SAURAN) [32] are represented by ambient temperature T_{amb}.

A complete description of each component of (3.13) follows.

Each of the building elements is described in terms of its dimensions and the materials used to construct it. If more than one material is used, the degree to which each contributes to the building element's characteristics is defined in its construction. In the present case, each building element is made from a single material, therefore requiring no elaborate construction specifications. Refer to Appendix B for construction and material characteristics.

Analogous to an electrical circuit, a modelling approach that views the simulated environment as a thermal resistive-capacitive network is used. Within this approach, a number of nodes make up the network, as depicted in Figure 3.8.

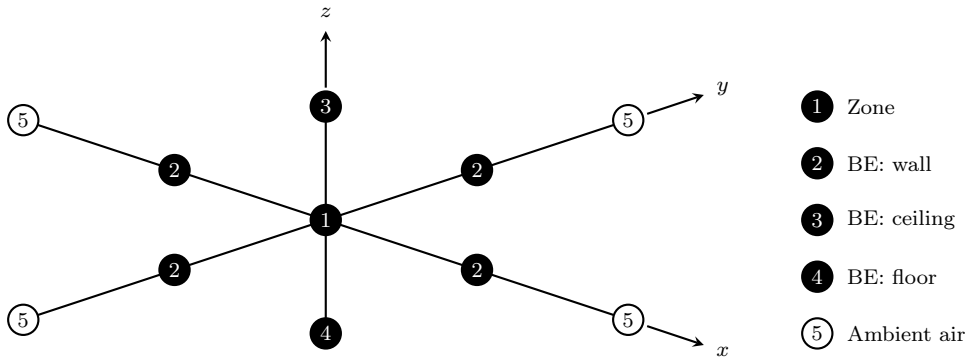

Figure 3.8: Simulated room components depicted as thermal nodes. 'BE', as used in the figure, is the acronym for 'building element.'

Heat exchange between two adjacent thermal nodes in Figure 3.8, i and j, can be described as follows [17, p. 70]:

$$\underbrace{\frac{dQ_i}{dx_i}}_{C_i} \frac{dx_i(t)}{dt} = \underbrace{A\,\alpha_{ij}}_{\frac{1}{R_{ij}}} \big(x_j(t) - x_i(t)\big), \tag{3.15a}$$

which, when rewritten, yields

$$C_i\,\dot{x}_i(t) = \frac{1}{R_{ij}}\big(x_j(t) - x_i(t)\big),$$
$$\dot{x}_i(t) = -\Big(\frac{1}{R_{ij}C_i}\Big)x_i(t) + \Big(\frac{1}{R_{ij}C_i}\Big)x_j(t). \tag{3.15b}$$

Here Q_i is the enthalpy (stored thermal energy) of node i, while C_i is its thermal capacitance. The cross-sectional area of contact between the nodes is represented by A and α_{ij} the convection coefficient between them, the product of which is equivalent to the inverse of thermal resistance R_{ij}. Node temperatures are represented by x_i and x_j.

Algorithm 1[1] describes the procedure through which all thermal interactions, as stated in (3.15b), are modelled in matrix form (denoted by subscript 't'). Index j_{Z} denotes the position of x_{Z} in $\boldsymbol{x}_{\mathrm{AHU}}$ and, similarly, $j_{\mathrm{BE},i}$ denotes the position of the i^{th} building element in $\boldsymbol{x}_{\mathrm{AHU}}$.

Algorithm 1 Construction of room thermal model matrices

function $[\boldsymbol{A}_{\mathrm{t}}, \boldsymbol{B}_{\mathrm{t}}]$ = `ROOM_THERMAL_MODEL(thermal_model_data)`
  Initialise $\bar{\boldsymbol{A}}$ as 0
  Zone heat capacity $C_{\mathrm{Z}} \leftarrow c_{\mathrm{air}}\,\rho_{\mathrm{air}}\,V_{\mathrm{Z}}$
  $\boldsymbol{C} \leftarrow C_{\mathrm{Z}}$
  for i from 1 to n_{BE} **do**
    i^{th} building element's heat capacity $C_{\mathrm{BE},i} \leftarrow a_{\mathrm{BE},i}\,d_{\mathrm{BE},i}\,\rho_{\mathrm{BE},i}\,c_{\mathrm{BE},i}$
    $\boldsymbol{C} \leftarrow \boldsymbol{C}$ appended with $C_{\mathrm{BE},i}$
    $\bar{\boldsymbol{A}} \leftarrow \mathtt{blkdiag}(\bar{\boldsymbol{A}}, 0)$
    Determine indices j_{Z} and $j_{\mathrm{BE},i}$ (positions of zone and i^{th} building element in $\boldsymbol{x}_{\mathrm{AHU}}$ vector)
    $\bar{\boldsymbol{A}}(j_{\mathrm{Z}}, j_{\mathrm{BE},i}) \leftarrow a_{\mathrm{BE},i}/\big(\frac{d_{\mathrm{BE},i}\,R_{\lambda,\mathrm{BE}}}{2} + \frac{1}{\alpha_{\mathrm{BE},i}}\big)$
    $\bar{\boldsymbol{A}}(j_{\mathrm{BE},i}, j_{\mathrm{Z}}) \leftarrow a_{\mathrm{BE},i}/\big(\frac{d_{\mathrm{BE},i}\,R_{\lambda,\mathrm{BE}}}{2} + \frac{1}{\alpha_{\mathrm{BE},i}}\big)$
    $\bar{\boldsymbol{A}}(j_{\mathrm{Z}}, j_{\mathrm{Z}}) \leftarrow -a_{\mathrm{BE},i}/\big(\frac{d_{\mathrm{BE},i}\,R_{\lambda,\mathrm{BE}}}{2} + \frac{1}{\alpha_{\mathrm{BE},i}}\big)$
    $\bar{\boldsymbol{A}}(j_{\mathrm{BE},i}, j_{\mathrm{BE},i}) \leftarrow -a_{\mathrm{BE},i}/\big(\frac{d_{\mathrm{BE},i}\,R_{\lambda,\mathrm{BE}}}{2} + \frac{1}{\alpha_{\mathrm{BE},i}}\big)$
  end for
  $\bar{\boldsymbol{B}} \leftarrow \mathbf{I}$ of same dimensions as $\bar{\boldsymbol{A}}$
  $\boldsymbol{A}_{\mathrm{t}} \leftarrow \boldsymbol{C}^{-1}\bar{\boldsymbol{A}}$
  $\boldsymbol{B}_{\mathrm{t}} \leftarrow \boldsymbol{C}^{-1}\bar{\boldsymbol{B}}$
end function

Heat Flux: Ambient Air

Heat fluxes are denoted by a subscript 'q'. The procedure for the first of which, ambient air, follows below.

[1] Algorithm 1 makes use of the $\mathtt{blkdiag}(\boldsymbol{A}, \boldsymbol{B})$ function, which returns $\begin{bmatrix}\boldsymbol{A} & \boldsymbol{0}\\ \boldsymbol{0} & \boldsymbol{B}\end{bmatrix}$. This notation is also used elsewhere in the thesis.

Heat is lost to the ambient air surrounding the room's walls. Both the ceiling and floor temperatures are also state variables, but heat exchanges on their outside adjacent surfaces are not taken into account, as they are considered to be negligible [18]. Although this model of heat exchange is greatly simplified, it succeeds in representing the most significant interactions. Algorithm 2 describes the relevant procedure, where `thermal_model_data` is a data structure containing the room and building elements' relevant characteristics.

Algorithm 2 Heat exchange between room walls and ambient air

function $[\boldsymbol{A}_{\text{q,amb}},\ \boldsymbol{B}_{\text{q,v,amb}}]$ = `AMB_MATS(thermal_model_data)`
  Initialise $\boldsymbol{A}_{\text{q,amb}}$ and $\boldsymbol{B}_{\text{q,v,amb}}$ as $\boldsymbol{0}^{(n_{\text{Z}}+n_{\text{BE}})\times(n_{\text{Z}}+n_{\text{BE}})}$
  for i from 1 to $n_{\text{BE}}-2$ **do**
    Determine index $j_{\text{BE},i}$ (position of i^{th} building element in $\boldsymbol{x}_{\text{AHU}}$ vector)
    $\boldsymbol{A}_{\text{q,amb}}(j_{\text{BE},i}, j_{\text{BE},i}) = -a_{\text{BE},i}/\left(\frac{1}{\alpha_{\text{AdjB},i}} + R_{\lambda,i}\ \frac{d_i}{2}\right)$
    $\boldsymbol{B}_{\text{q,v,amb}}(j_{\text{BE},i}, j_{\text{BE},i}) = a_{\text{BE},i}/\left(\frac{1}{\alpha_{\text{AdjB},i}} + R_{\lambda,i}\ \frac{d_i}{2}\right)$
  end for
end function

Heat Flux: Dual Split-Inverter AHU

The room temperature is regulated by an AHU of the dual split-inverter variant, described in Appendix B. The device can only be toggled between 'on' and 'off' states. Its on-state power consumption is time-varying and dependent on the difference between present state and reference temperatures.

Time-varying AHU power consumption is calculated through use of the AHU conversion vector $\boldsymbol{c}_{\text{AHU}}(k)$, defined as

$$\boldsymbol{c}_{\text{AHU}}(k) = \begin{bmatrix} c_{\dot{\text{m}}}(k) & c_{\text{H}}(k) & c_{\text{C}}(k) \end{bmatrix}^{\text{T}}, \tag{3.16}$$

where $c_{\dot{\text{m}}}(k)$, $c_{\text{H}}(k)$ and $c_{\text{C}}(k)$ are the estimated mass flow rate, heating, and cooling coefficients, respectively. Note that $c_{\text{H}}(k)$ and $c_{\text{C}}(k)$ cannot have non-zero values simultaneously; the AHU is either heating or cooling at any given point in time, based on which action will reduce the discrepancy between actual and reference room temperatures to the greatest extent. For this functionality, a simple quadratic cost function $J_{\text{AHU,ctrl}}(k)$ is used:

$$J_{\text{AHU,ctrl}}(k) = \Big(x_{\text{Z}}\big(\boldsymbol{c}_{\text{AHU}}(k), T_{\text{amb}}(k)\big) - x_{\text{Z,ref}}(k)\Big)^2. \tag{3.17}$$

The internal controller compares $J^*_{\text{H}}(k)$, defined as

$$\begin{aligned} J^*_{\text{H}}(k) = &\min_{\boldsymbol{c}_{\text{AHU}}} J_{\text{AHU,ctrl}}(k) \\ &\text{subject to constraints on } c_{\dot{\text{m}}}(k) \text{ and } c_{\text{H}}(k), \\ &\text{and } c_{\text{C}}(k) = 0, \end{aligned} \tag{3.18}$$

with $J_{\mathrm{C}}^{*}(k)$, defined as

$$\begin{aligned} J_{\mathrm{C}}^{*}(k) = \min_{\boldsymbol{c}_{\mathrm{AHU}}} & J_{\mathrm{AHU,ctrl}}(k) \\ & \text{subject to constraints on } c_{\dot{\mathrm{m}}}(k) \text{ and } c_{\mathrm{C}}(k), \\ & \text{and } c_{\mathrm{H}}(k) = 0, \end{aligned} \tag{3.19}$$

where the applicable constraints are dependent on the product chosen to simulate (in this instance an Alliance Arctic Midwall unit [34]).
The lowest-cost option between the optimal cooling and heating costs is selected and the applicable $\boldsymbol{c}_{\mathrm{AHU}}(k)$ returned.

In [18], it is reported that most heating, ventilation, and cooling models employ straight-line relations between the temperature regulation effort exerted by the AHU and its energy usage. Under the assumption that the fan extracting or injecting air approximates ideal behaviour, an estimate of the fan's power consumption can be made, based on the volumetric air flow rates supplied. Figure 3.9 depicts this relation for the AHU used in this instance.

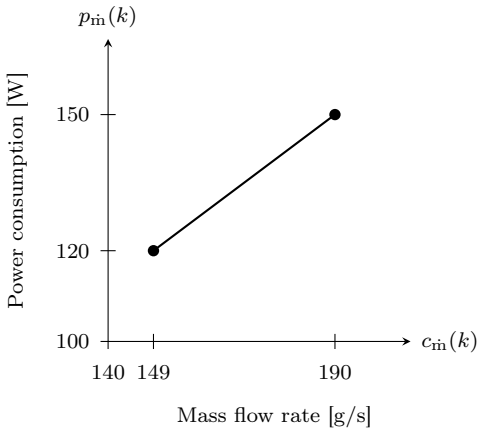

Figure 3.9: AHU fan power consumption curve.

The straight-line approximation, combined with the coefficient of performance (COP) and energy efficiency ratio (EER) specifications provided [34] (refer to Appendix B for an extract from the datasheet), can be used to convert the AHU coefficients to representative power consumption values, as shown:

$$p_{\mathrm{AHU}}(k) = \left(\gamma_1 c_{\dot{\mathrm{m}}}(k) + \gamma_2\right) + \frac{c_{\mathrm{H}}(k)}{\mathrm{COP}} + \frac{c_{\mathrm{C}}(k)}{\mathrm{EER}}, \tag{3.20}$$

where $c_{\{\dot{\mathrm{m}},\mathrm{H},\mathrm{C}\}}(k)$ are the elements of $\boldsymbol{c}_{\mathrm{AHU}}(k)$, while constants γ_1 and γ_2 are the gradient and vertical-axis intersection of Figure 3.9, respectively.

Within the state-space representation, coefficient vector $\boldsymbol{c}_{\mathrm{AHU}}(k)$ is separated from an

integer control input $u_{\mathrm{AHU}}(k)$, defined as

$$u_{\mathrm{AHU}}(k) \in \{0, 1\}. \tag{3.21}$$

Heat-flux control-input matrix $\boldsymbol{B}_{\mathrm{q},u} \in \mathbb{R}^{(n_{\mathrm{Z}}+n_{\mathrm{BE}})\times(n_{\mathrm{Z}}+n_{\mathrm{BE}})}$ is sparse, containing only the following non-zero entries:

$$\boldsymbol{B}_{\mathrm{q},u}(i_{\mathrm{Z}}, i_{c_{\mathrm{H}}}) = 1 \tag{3.22a}$$

and

$$\boldsymbol{B}_{\mathrm{q},u}(i_{\mathrm{Z}}, i_{c_{\mathrm{C}}}) = -1, \tag{3.22b}$$

which correspond with the AHU coefficient values $c_{\mathrm{H}}(k)$ and $c_{\mathrm{C}}(k)$.

Similarly, state control-input matrix $\boldsymbol{B}_{\mathrm{q},xu}$ and disturbance-input control-input matrix $\boldsymbol{B}_{\mathrm{q},vu}$ consist mostly of zeroes, save for the following entries:

$$\boldsymbol{B}_{\mathrm{q},xu}(j_{\mathrm{Z}}, j_{\mathrm{Z}}) = -c_{\mathrm{air}}, \tag{3.23}$$

and

$$\boldsymbol{B}_{\mathrm{q},vu}(j_{\mathrm{Z}}, j_{\mathrm{T_{amb}}}) = c_{\mathrm{air}}. \tag{3.24}$$

Constant c_{air} represents the specific heat capacity of air and converts the air mass removed or added to the room into its equivalent in terms of energy extracted or injected into said room. Index $j_{\mathrm{T_{amb}}}$ refers to the offset of the first instance of T_{amb} in $\boldsymbol{v}_{\mathrm{AHU}}$.

AHU State-Space Matrices

Matrices describing the room's own characteristics, as well as those relating to heat fluxes, are developed in prior sections. Here, they are discretised (with a sampling period of T_{s}) and combined to yield the AHU state-space model.

The product of $\boldsymbol{B}_{\mathrm{t}}$ and the various thermal resistance matrices represent temperature transfer rates between modelled elements per unit time. The discretised matrices represent transfer rates per sampling interval. When used in concert with $\boldsymbol{x}_{\mathrm{AHU}}$, u_{AHU}, and $\boldsymbol{v}_{\mathrm{AHU}}$, temperature changes can be modelled across the system as a whole.

The continuous-time state matrix $\boldsymbol{A}_{\mathrm{AHU,c}}$ is calculated as

$$\boldsymbol{A}_{\mathrm{AHU,c}} = \boldsymbol{A}_{\mathrm{t}} + \boldsymbol{A}_{\mathrm{q,amb}}. \tag{3.25}$$

Each of the continuous-time matrices are discretised, using the exact discretisation method, as shown below:

$$\boldsymbol{A}_{\mathrm{AHU}} = \boldsymbol{e}^{\boldsymbol{A}_{\mathrm{AHU,c}} T_{\mathrm{s}}}, \tag{3.26a}$$

$$\boldsymbol{B}_{\mathrm{AHU},u} = \int_0^{T_{\mathrm{s}}} \boldsymbol{e}^{\boldsymbol{A}_{\mathrm{AHU,c}} \tau} d\tau \; \boldsymbol{B}_{\mathrm{t}} \; \boldsymbol{B}_{\mathrm{q},u}, \tag{3.26b}$$

$$\boldsymbol{B}_{\mathrm{AHU},v} = \int_0^{T_\mathrm{s}} \boldsymbol{e}^{\boldsymbol{A}_{\mathrm{AHU,c}}\tau} d\tau \; \boldsymbol{B}_\mathrm{t} \; \boldsymbol{B}_{\mathrm{q},v}, \tag{3.26c}$$

$$\boldsymbol{B}_{\mathrm{AHU},xu} = \int_0^{T_\mathrm{s}} \boldsymbol{e}^{\boldsymbol{A}_{\mathrm{AHU,c}}\tau} d\tau \; \boldsymbol{B}_\mathrm{t} \; \boldsymbol{B}_{\mathrm{q},xu}, \tag{3.26d}$$

and, lastly,

$$\boldsymbol{B}_{\mathrm{AHU},vu} = \int_0^{T_\mathrm{s}} \boldsymbol{e}^{\boldsymbol{A}_{\mathrm{AHU,c}}\tau} d\tau \; \boldsymbol{B}_\mathrm{t} \; \boldsymbol{B}_{\mathrm{q},vu}. \tag{3.26e}$$

Matrix and vector dimensions are given below:

$$n_\mathrm{AHU} = n_\mathrm{Z} + n_\mathrm{BE},$$

$$\boldsymbol{x}_\mathrm{AHU}(k), \boldsymbol{v}_\mathrm{AHU}(k) \in \mathbb{R}^{n_\mathrm{AHU}}, \boldsymbol{u}_\mathrm{AHU}(k) \in \mathbb{R}^{m_\mathrm{AHU}},$$

$$\boldsymbol{A}_\mathrm{AHU}, \boldsymbol{B}_{\mathrm{AHU},v}, \boldsymbol{B}_{\mathrm{AHU},xu}, \boldsymbol{B}_{\mathrm{AHU},vu} \in \mathbb{R}^{n_\mathrm{AHU} \times n_\mathrm{AHU}},$$

$$\boldsymbol{B}_{\mathrm{AHU},u} \in \mathbb{R}^{n_\mathrm{AHU} \times m_\mathrm{AHU}}.$$

AHU Test Simulation

The dual split-inverter AHU used is an Alliance Arctic Midwall FOUSI12 (12 000 Btu) [34], the specifications of which are given in Table B.9.

A 24 h simulation is done using ambient temperature data from 11 September 2017 (selected arbitrarily). The AHU injects heat into the room from 08:00 to 17:00, following a reference temperature of 26 °C. The resulting temperature progression is shown in Figure 3.10a.

The room volume is within the AHU's operating range (48 m^3; refer to Table B.1 for complete dimensions description), and therefore room temperature can be regulated successfully. A temperature drop can be observed at 08:00. Room temperature at the previous time step is at ambient temperature, therefore no heat is lost to surrounding building elements (also still at ambient temperature). Losses are incurred at the next time step, however, and as a result the AHU briefly operates at maximum capacity to mitigate the difference between room and reference temperature.

The room walls act as a buffer between zone temperature x_Z and the surrounding ambient air. Once the AHU is switched off, room-temperature decline is buoyed by the enthalpy of surrounding building elements.

AHU power consumption during the simulation is shown in Figure 3.10b. As ambient temperature rises, the inverter-type AHU requires less power to regulate the room air to its reference temperature.

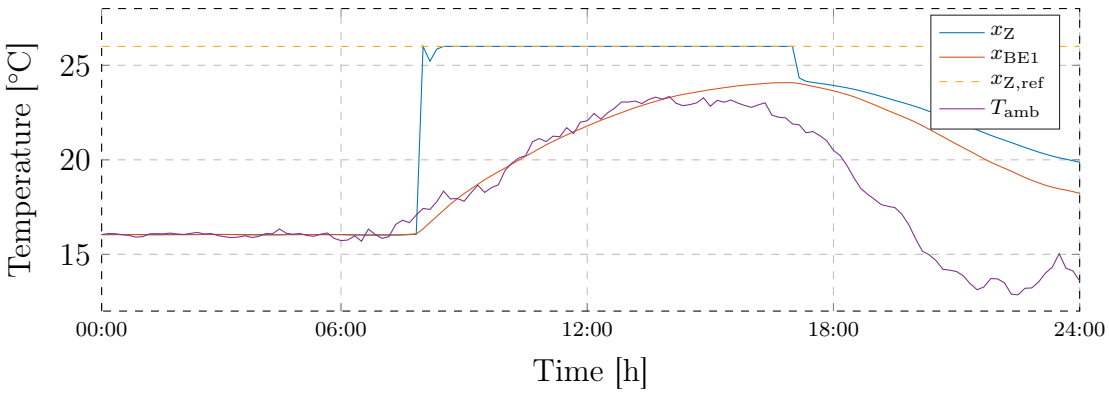

(a) Air, wall, reference, and ambient temperatures.

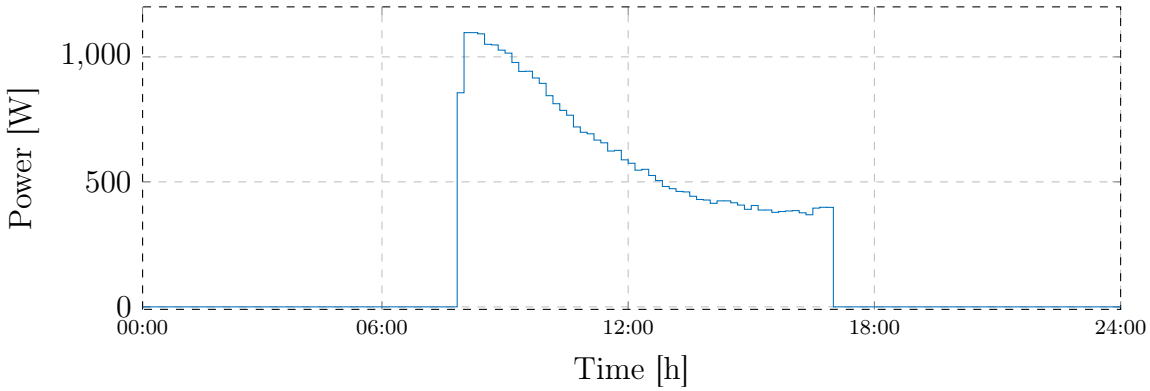

(b) Power consumption.

Figure 3.10: AHU test simulation results, using ambient-air temperature data from 11 September 2017.

The model successfully captures the exponential decay of heat in air, as can be seen in the temperature decline in both the room and wall temperatures from 18:00 onwards. Additionally, the reduced power required to maintain room temperature at reference, as ambient air temperature rises, is characteristic of inverter-type AHUs. The focus of both [17] and [18] is multi-room building management, and detailed power consumption graphs are not available to compare present model operation against. As the thermal behaviour compares well, operating from the same modelling approach, power consumption is assumed to be reasonably estimated, as well.

3.3.3 Electric Water Heater

In this section the EWH model is described, followed by a test simulation.

Model Description

A suitable model, converted into its equivalent state-space representation from [15], is used. In [15], one- and two-node models are compared, with the latter's gains in accuracy over the former minuscule. The one-node model is reworked for the present application,

as it can be applied to either a horizontally- or vertically-installed water heater. It is an approximation, as it assumes uniform temperature distribution within the tank. Water temperature within the EWH is defined as state x_{EWH} [°C], and the one-node model can be summarised as

$$x_{\text{EWH}}(k+1) = a_{\text{EWH}} x_{\text{EWH}}(k) + b_{\text{EWH},u} u_{\text{EWH}}(k) + \boldsymbol{B}_{\text{EWH},v}(k)\boldsymbol{v}_{\text{EWH}}(k)\ [^\circ\text{C}], \tag{3.27a}$$

where $u_{\text{EWH}}(k)$ is the EWH control input, defined as an integer (i.e. 'on/off') input, that is,

$$u_{\text{EWH}}(k) \in \{0, 1\}, \tag{3.27b}$$

and $\boldsymbol{v}_{\text{EWH}}(k)$ its disturbance-input vector. Additionally, a_{EWH} is its state coefficient and $b_{\text{EWH},u}$ its control-input coefficient. The disturbance input vector $\boldsymbol{B}_{\text{EWH},v}(k)$ is defined as

$$\boldsymbol{B}_{\text{EWH},v}(k) = \boldsymbol{b}^{\text{T}}_{\text{EWH},v} + b_{\text{EWH},xv} x_{\text{EWH}}(k) \tilde{\boldsymbol{1}}^{\text{T}}_{\text{EWH},xv} + b_{\text{EWH},vv} \boldsymbol{v}^{\text{T}}_{\text{EWH}}(k) \tilde{\boldsymbol{1}}_{\text{EWH},vv}, \tag{3.27c}$$

where

$$\boldsymbol{b}_{\text{EWH},v} = \begin{bmatrix} b_{\text{EWH},v} & 0 & 0 \end{bmatrix}^{\text{T}}, \tag{3.27d}$$

with $b_{\text{EWH},v}$ being the EWH disturbance coefficient. Additionally, $b_{\text{EWH},xv}$ is its state-disturbance coefficient and $b_{\text{EWH},vv}$ its disturbance-disturbance coefficient. Lastly, the EWH's auxiliary vector and matrix are defined as

$$\tilde{\boldsymbol{1}}_{\text{EWH},xv} = \begin{bmatrix} 0 & 1 & 0 \end{bmatrix}^{\text{T}} \tag{3.27e}$$

and

$$\tilde{\boldsymbol{1}}_{\text{EWH},vv} = \begin{bmatrix} 0 & 0 & 0 \\ 0 & 0 & 0 \\ 0 & 1 & 0 \end{bmatrix}, \tag{3.27f}$$

which are used to convert products between variables to their state-space equivalent.

A description of each coefficient used in (3.27) follows.

Energy contained within an EWH is lost through two mechanisms: heat loss due to an ambient temperature lower than that of the water within, and the loss of heated water during a usage event (when water is drawn off, the lost volume is replenished with water at a significantly lower temperature). Figure 3.11 depicts these interactions.

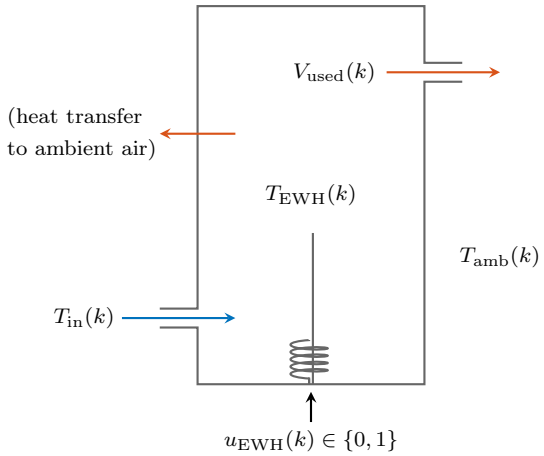

Figure 3.11: A graphical depiction of the water-heating variables' representations.

In state-space parlance, the methods of energy loss can be modelled through the use of disturbances. Specifically, the following disturbances are considered: ambient temperature T_{amb}, volume of heated water drawn-off V_{used}, and the temperature of incoming water T_{in}. These factors comprise the disturbance vector

$$\boldsymbol{v}_{\text{EWH}}(k) = \begin{bmatrix} T_{\text{amb}}(k) & V_{\text{used}}(k) & T_{\text{in}}(k) \end{bmatrix}^{\text{T}} \in \mathbb{R}^{n_{\text{EWH},v}}. \tag{3.28}$$

Lost heat can be replenished through means of the heating element within the tank in question, at rated power $P_{\text{EWH,r}}$. The heating-element state is referred to as control input u_{EWH}.

State coefficient a_{EWH} is defined as

$$a_{\text{EWH}} = e^{\beta}, \tag{3.29}$$

and represents the dissipation of stored heat into the surrounding environment. Constant β is defined as

$$\beta = \frac{-T_{\text{s}}}{c_{\text{water}}\, \rho_{\text{water}}\, V_{\text{EWH}}\, R_{\text{EWH}}}, \tag{3.30}$$

where T_{s} is the simulation sample period, c_{water} is the specific thermal capacitance of water, ρ_{water} is the density of water, V_{EWH} is the volume of the EWH tank, and R_{EWH} is the thermal resistance of the tank itself.

Input coefficient $b_{\text{EWH},u}$ can be defined as

$$b_{\text{EWH},u} = \frac{P_{\text{EWH,r}}\, T_{\text{s}}}{c_{\text{water}}\, m_{\text{EWH}}}, \tag{3.31}$$

where $P_{\text{EWH,r}}$ is the rated EWH input power and EWH mass m_{EWH} is the product of ρ_{water} and V_{EWH}.

Disturbance coefficient $b_{\text{EWH},v}$ is defined as

$$b_{\text{EWH},v} = (1 - e^{\beta}). \tag{3.32}$$

State-disturbance coefficient $b_{\text{EWH},xv}$ is defined as

$$b_{\text{EWH},xv} = \frac{-e^{\beta}}{V_{\text{EWH}}}. \tag{3.33}$$

Finally, disturbance-disturbance coefficient $b_{\text{EWH},vv}$ is defined as

$$b_{\text{EWH},vv} = \frac{1}{V_{\text{EWH}}}. \tag{3.34}$$

For completeness' sake:

$$x_{\text{EWH}}, a_{\text{EWH}}, b_{\text{EWH},u}, b_{\text{EWH},v}, b_{\text{EWH},vv}, b_{\text{EWH},xv} \in \mathbb{R}.$$

In the interest of generality, refer to the dimensions of the EWH state as residing in n_{EWH}-dimensional real space and its control input within m_{EWH}-dimensional binary space.

EWH Test Simulation

A 24 h simulation is done to illustrate the working of the EWH model. Table 3.3 lists the parameter values used in the test simulation [15]. Inflowing water is assumed to be at ambient temperature.

Table 3.3: Electric water heater parameter values

Parameter	Value	Units
c_{water}	4.185	$\frac{\text{kJ}}{\text{kg·K}}$
ρ_{water}	1000	kg/m^3
R_{EWH}	0.43	K/W
$P_{\text{EWH,r}}$	3	kW
V_{EWH}	0.15	m^3

Hot water-usage data are taken from [35], which provides data for a number of anonymous households, one instance of which is used for $V_{\text{used}}(k)$. This dataset is assumed to be representative of typical household hot water-consumption behaviour. Ambient temperature data for 11 September 2017 are used. The demonstration date is arbitrarily selected.

Water temperature inside the EWH tank can be seen in Figure 3.12a. The EWH reference temperature is 65 °C. Corresponding hot-water volume consumed, batched in 5-minute increments, can be seen in Figure 3.12b. The input power required to replenish lost heat can be seen in Figure 3.12c.

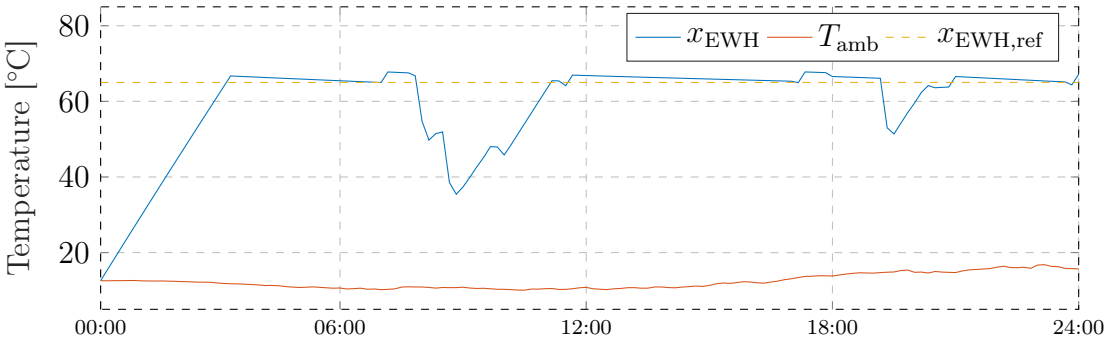

(a) Water, ambient, and reference temperatures.

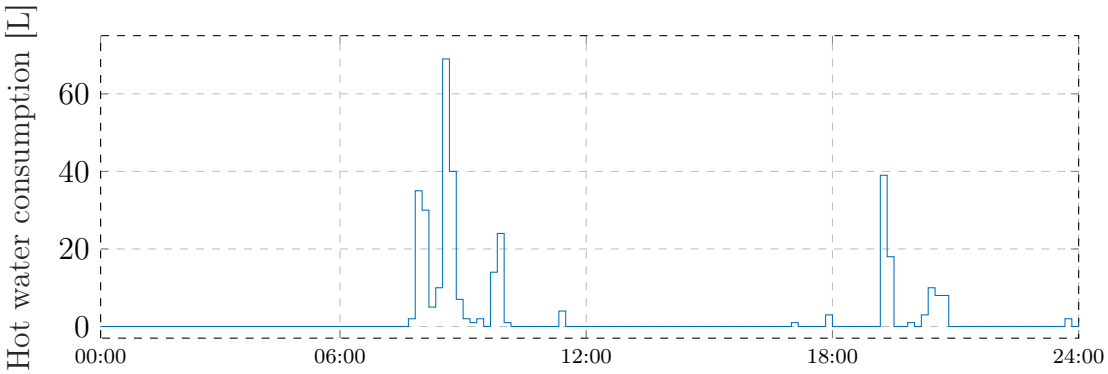

(b) Hot-water volume consumed during usage events.

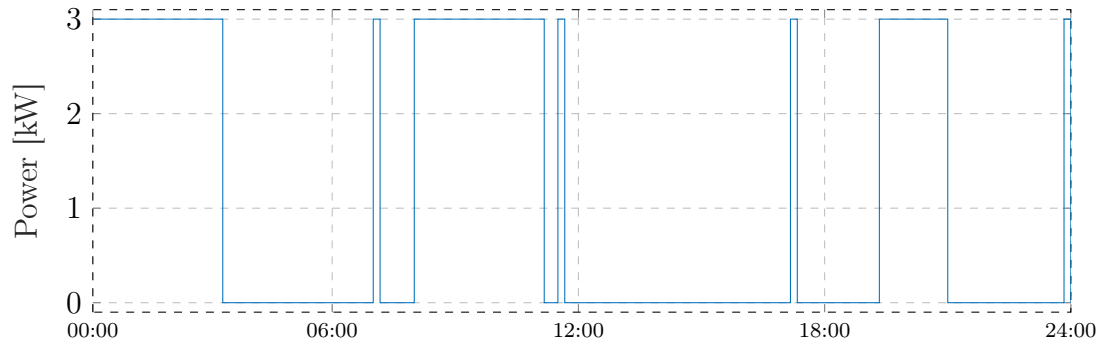

(c) Load power. Short bursts of power consumption are observed outside of usage periods, when the tank water temperature drops below 65 °C (its reference temperature).

Figure 3.12: EWH test simulation temperatures, volume consumed and power consumption on 11 September 2017.

Heat loss as a result of usage events follows the behaviour of the one-node model in [15], which confirms the validity of the state-space representation of the model.

3.3.4 Combined State-Space Model of Selected Subsystems

As the overarching goal requires a single model, it is beneficial to combine the various subsystems into a combined state-space representation, written as

$$\boldsymbol{x}(k+1) = \boldsymbol{A}\boldsymbol{x}(k) + \boldsymbol{B}_u(k)\boldsymbol{u}(k) + \boldsymbol{B}_v(k)\boldsymbol{v}(k), \tag{3.35}$$

where the combined state vector is

$$\boldsymbol{x}(k) = \begin{bmatrix} \boldsymbol{x}_{\text{BES}}^{\text{T}}(k) & \boldsymbol{x}_{\text{AHU}}^{\text{T}}(k) & x_{\text{EWH}}(k) \end{bmatrix}^{\text{T}} \in \mathbb{R}^{n_x}, \tag{3.36}$$

with

$$n_x = n_{\text{BES}} + n_{\text{AHU}} + n_{\text{EWH}}. \tag{3.37}$$

Control inputs can be divided into those of a continuous nature and those of an integer nature. The latter are only capable of existing in either an 'on' or 'off' binary state. Denote the vector of continuous-control inputs as $\boldsymbol{u}_{\text{c}}$ and its binary counterpart as $\boldsymbol{u}_{\text{b}}$. These are, respectively,

$$\boldsymbol{u}_{\text{c}}(k) = \boldsymbol{u}_{\text{batt}}(k) \in \mathbb{R}^{m_{\text{c}}}, \tag{3.38}$$

and

$$\boldsymbol{u}_{\text{b}}(k) = \begin{bmatrix} u_{\text{AHU}}(k) \\ u_{\text{EWH}}(k) \end{bmatrix} \in \{0,1\}^{m_{\text{b}}}. \tag{3.39}$$

Note that $m_{\text{c}} = m_{\text{BES}}$ and $m_{\text{b}} = m_{\text{AHU}} + m_{\text{EWH}}$. Written together, the control-input vector is

$$\boldsymbol{u}(k) = \begin{bmatrix} \boldsymbol{u}_{\text{c}}(k) \\ \boldsymbol{u}_{\text{b}}(k) \end{bmatrix} \in \mathbb{R}^{m_{\text{c}}} \times \{0,1\}^{m_{\text{b}}}. \tag{3.40}$$

Collectively, the control-input vector is of dimension $m = m_{\text{c}} + m_{\text{b}}$.

Disturbance vector $\boldsymbol{v}(k)$ can be defined as

$$\boldsymbol{v}(k) = \begin{bmatrix} \boldsymbol{0}^{n_{\text{BES}}} & \boldsymbol{v}_{\text{AHU}}^{\text{T}}(k) & \boldsymbol{v}_{\text{EWH}}^{\text{T}}(k) \end{bmatrix}^{\text{T}} \in \mathbb{R}^{n_v}, \tag{3.41}$$

where

$$n_v = n_{\text{BES}} + n_{\text{AHU}} + n_{\text{EWH},v}. \tag{3.42}$$

The state matrix $\boldsymbol{A} \in \mathbb{R}^{n_x \times n_x}$ of the system is described as

$$\boldsymbol{A} = \begin{bmatrix} \boldsymbol{A}_{\text{BES}} & \boldsymbol{0}^{n_{\text{BES}} \times n_{\text{AHU}}} & \boldsymbol{0}^{n_{\text{BES}} \times n_{\text{EWH}}} \\ \boldsymbol{0}^{n_{\text{AHU}} \times n_{\text{BES}}} & \boldsymbol{A}_{\text{AHU}} & \boldsymbol{0}^{n_{\text{AHU}} \times n_{\text{EWH}}} \\ \boldsymbol{0}^{n_{\text{EWH}} \times n_{\text{BES}}} & \boldsymbol{0}^{n_{\text{EWH}} \times n_{\text{AHU}}} & a_{\text{EWH}} \end{bmatrix}, \tag{3.43}$$

the combined control input matrix $\boldsymbol{B}_u(k) \in \mathbb{R}^{n_x \times m}$ is defined as

$$\boldsymbol{B}_u(k) = \begin{bmatrix} \boldsymbol{B}_{\text{BES}} & \boldsymbol{0}^{n_{\text{BES}} \times m_{\text{AHU}}} & \boldsymbol{0}^{n_{\text{BES}} \times m_{\text{EWH}}} \\ \boldsymbol{0}^{n_{\text{AHU}} \times m_{\text{BES}}} & \boldsymbol{B}_{\text{AHU},u}(k) & \boldsymbol{0}^{n_{\text{AHU}} \times m_{\text{EWH}}} \\ \boldsymbol{0}^{n_{\text{EWH}} \times m_{\text{BES}}} & \boldsymbol{0}^{n_{\text{EWH}} \times m_{\text{AHU}}} & b_{\text{EWH},u} \end{bmatrix}, \tag{3.44}$$

and the combined disturbance input matrix $\boldsymbol{B}_v(k) \in \mathbb{R}^{n_x \times n_v}$ is defined as

$$\boldsymbol{B}_v(k) = \begin{bmatrix} \mathbf{0}^{n_{\text{BES}} \times n_{\text{BES}}} & \mathbf{0}^{n_{\text{BES}} \times n_{\text{AHU}}} & \mathbf{0}^{n_{\text{BES}} \times n_{\text{EWH},v}} \\ \mathbf{0}^{n_{\text{AHU}} \times n_{\text{BES}}} & \boldsymbol{B}_{\text{AHU},v} & \mathbf{0}^{n_{\text{AHU}} \times n_{\text{EWH},v}} \\ \mathbf{0}^{n_{\text{EWH}} \times n_{\text{BES}}} & \mathbf{0}^{n_{\text{EWH}} \times n_{\text{AHU}}} & \boldsymbol{B}_{\text{EWH},v}(k) \end{bmatrix}. \tag{3.45}$$

3.4 Summary

Chapter 3 describes a framework that provides a unified view of diverse electrical entities by focusing on shared properties. A sample system, using said framework, is proposed. Descriptions of selected controllable and uncontrollable subsystems (referred to as 'nodes') follow. Simulation results for controllable nodes agree with those of referenced models. Lastly, controllable nodes are combined into a single state-space representation suitable for use within a control system.

Chapter 4

Predictive Control

This chapter describes a predictive-control strategy aimed at maximising the utilisation of a given PV array, defined as the percentage of generated energy usefully employed within the local power system, while adhering to specified temperature constraints. The general structure of the strategy is described, followed by relevant mathematical and algorithmic formulations. An evaluation of controller performance follows thereafter. The chapter concludes with a summary.

4.1 Control System Structure

Figure 4.1 depicts the described control system. To maximise the productivity of a given solar PV array, the control system is structured as follows: The sum total generated power of uncontrollable generation-only (i.e. $\xi \geq 0$) nodes, minus the sum total load power of uncontrollable load-only (i.e. $\xi \leq 0$) nodes, is fed into a controller as target power $p_{\text{target}}(k)$. State-reference vector $\boldsymbol{X}_{\text{ref}}(k)$, consisting of selected state-reference values, and a number of penalty matrices act as inputs to the controller. Deviations from the state and control-input references, change in control input, and constraint parameters are regulated through means of penalty matrices. State $\boldsymbol{x}(k)$ and the previous discrete-time instant's control input $\boldsymbol{u}(k-1)$, along with disturbance vector $\boldsymbol{v}(k)$, are also fed into the controller. Each of these variable vectors and matrices are discussed in follow-on sections. State-space representation (3.35) acts as the plant upon which control is exerted, repeated here for convenience:

$$\boldsymbol{x}(k+1) = \boldsymbol{A}\boldsymbol{x}(k) + \boldsymbol{B}_u(k)\boldsymbol{u}(k) + \boldsymbol{B}_v(k)\boldsymbol{v}(k). \tag{4.1}$$

Note that the plant is bilinear in nature, because of the products between state, input and disturbance variables. The implication for control purposes is that the plant is mildly non-linear, seeing as the disturbance and state variables change slowly. This impacts the choice of numerical solver, as it has to capable of accommodating non-linearities.

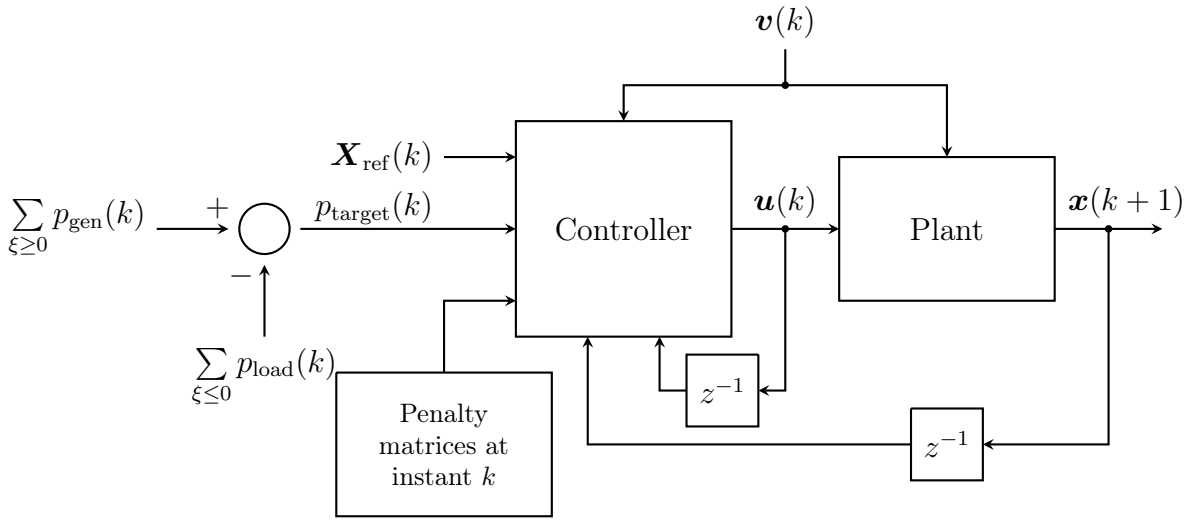

Figure 4.1: The control-system diagram.

4.2 Problem Formulation

The optimal control-input sequence $\boldsymbol{U}^*(k)$ is determined by minimising an objective function $J(k)$ over a prediction horizon N. Where after, only the first vector in the sequence, $\boldsymbol{u}(k)$, is applied to the plant at time k. The procedure is repeated at each time step thereafter, constituting a receding-horizon policy. This makes the system more robust against noise and unanticipated changes in references, states, and disturbances. The objective function, defined in (4.2a), consists of three terms for each step over horizon N, at each time step:

- The first penalises deviations from a specified state reference, weighted by state penalty matrix $\boldsymbol{Q}$.
- The second performs a similar role for control inputs, weighted by control-input penalty matrix $\boldsymbol{R}$.
- Lastly, the third term discourages continuous commutation (i.e. interchange between integer inputs' states), weighted by control-input change penalty matrix $\boldsymbol{R}_{\Delta u}$.

In this section, the parts of $J(k)$, as well as constraints acting in on the control system, are described in detail.

4.2.1 Objective Function Definition

Objective function $J(k)$ is defined as

$$J(k) = \sum_{l=k}^{k+N-1} \left(\|\boldsymbol{x}_{l+1} - \boldsymbol{x}_{\text{ref}}(l+1)\|_{\boldsymbol{Q}}^2 + \|\boldsymbol{u}_l - \boldsymbol{u}_{\text{ref},l}\|_{\boldsymbol{R}}^2 + \|\Delta\boldsymbol{u}_l\|_{\boldsymbol{R}_{\Delta u}}^2 \right), \tag{4.2a}$$

where

$$\|\boldsymbol{\zeta}\|_{\boldsymbol{M}}^2 = \boldsymbol{\zeta}^{\mathrm{T}}\boldsymbol{M}\boldsymbol{\zeta} \tag{4.2b}$$

is referred to as the weighted 2-norm (or Euclidean norm) relative to matrix $\boldsymbol{M}$. Matrix $\boldsymbol{M}$ has to be at least positive semi-definite for a solution to consistently exist. The objective function is quadratic in both the states and inputs, as this is a mathematically-convenient form. The sum in (4.2a) depicts all three parts of the objective function, as described above, but does not make for efficient use within an optimisation context. Calculating $J(k)$ via the brute-force approach, i.e. evaluating each of the possible sum sequences over an N-step horizon, quickly becomes computationally intractable as N increases. Instead, rewriting (4.2a) as a quadratic programme allows for longer horizons to be feasible by evaluating routes based on their respective cost, as opposed to exhaustively evaluating all possible options.

First, as an intermediate step, $J(k)$ is written in vector form, that is,

$$\begin{aligned} J(k) = &\|\boldsymbol{X}(k) - \boldsymbol{X}_{\mathrm{ref}}(k)\|_{\tilde{\boldsymbol{Q}}}^2 + \|\boldsymbol{U}(k) - \boldsymbol{U}_{\mathrm{ref}}(k)\|_{\tilde{\boldsymbol{R}}}^2 \\ &+ \left\|\tilde{\mathbf{I}}_{\Delta u}\boldsymbol{U}(k) - \tilde{\mathbf{I}}_{\Delta u,\mathrm{init}}\boldsymbol{u}(k-1)\right\|_{\tilde{\boldsymbol{R}}_{\Delta u}}^2, \end{aligned} \tag{4.3a}$$

making use of the vector form of the state-space representation:

$$\boldsymbol{X}(k) = \boldsymbol{S}_x\boldsymbol{x}(k) + \boldsymbol{S}_u(k)\boldsymbol{U}(k) + \boldsymbol{S}_v(k)\boldsymbol{V}(k), \tag{4.3b}$$

where

$$\boldsymbol{X}(k) = \begin{bmatrix} \boldsymbol{x}_{k+1} \\ \boldsymbol{x}_{k+2} \\ \vdots \\ \boldsymbol{x}_{k+N} \end{bmatrix}, \ \boldsymbol{U}(k) = \begin{bmatrix} \boldsymbol{u}_{k} \\ \boldsymbol{u}_{k+1} \\ \vdots \\ \boldsymbol{u}_{k+N-1} \end{bmatrix} \text{ and } \boldsymbol{V}(k) = \begin{bmatrix} \boldsymbol{v}(k) \\ \boldsymbol{v}_{k+1} \\ \vdots \\ \boldsymbol{v}_{k+N-1} \end{bmatrix} \tag{4.3c}$$

are the evolution of the state vector, the control-input vector and the disturbance-input vector over the prediction horizon, respectively.

The state- and input-reference vectors over the prediction horizon are defined as

$$\boldsymbol{X}_{\mathrm{ref}}(k) = \begin{bmatrix} \boldsymbol{x}_{\mathrm{ref}}(k+1) \\ \boldsymbol{x}_{\mathrm{ref}}(k+2) \\ \vdots \\ \boldsymbol{x}_{\mathrm{ref}}(k+N) \end{bmatrix} \in \mathbb{R}^{N\cdot n_x} \text{ and } \boldsymbol{U}_{\mathrm{ref}}(k) = \begin{bmatrix} \boldsymbol{u}_{\mathrm{ref}}(k) \\ \boldsymbol{u}_{\mathrm{ref},k+1} \\ \vdots \\ \boldsymbol{u}_{\mathrm{ref},k+N-1} \end{bmatrix} \in \mathbb{R}^{N(m_{\mathrm{c}}+m_{\mathrm{b}})}, \tag{4.3d}$$

respectively. All $\boldsymbol{X}_{\mathrm{ref}}(k)$ values are set, and thus known. Control-input reference $\boldsymbol{u}_{\mathrm{ref}}(k)$ is known, but all other instances $(\boldsymbol{u}_{\mathrm{ref},k+1}, \ldots, \boldsymbol{u}_{\mathrm{ref},k+N-1})$ are likely to change. Control-input reference generation is the subject of Section 4.3.

Furthermore, $\boldsymbol{S}_x \in \mathbb{R}^{N \cdot n_x \times n_x}$ is defined as

$$\boldsymbol{S}_x = \begin{bmatrix} \boldsymbol{A} \\ \boldsymbol{A}^2 \\ \vdots \\ \boldsymbol{A}^{\mathrm{N}} \end{bmatrix}, \tag{4.3e}$$

$\boldsymbol{S}_u(k) \in \mathbb{R}^{N \cdot n_x \times N \cdot m}$ is defined as

$$\boldsymbol{S}_u(k) = \begin{bmatrix} \boldsymbol{B}_u(k) & \boldsymbol{0} & \boldsymbol{0} & \cdots & \boldsymbol{0} \\ \boldsymbol{A}\boldsymbol{B}_u(k) & \boldsymbol{B}_{u,k+1} & \boldsymbol{0} & \cdots & \boldsymbol{0} \\ \boldsymbol{A}^2\boldsymbol{B}_u(k) & \boldsymbol{A}\boldsymbol{B}_{u,k+1} & \boldsymbol{B}_{u,k+2} & \cdots & \boldsymbol{0} \\ \vdots & \vdots & \vdots & \ddots & \vdots \\ \boldsymbol{A}^{N-1}\boldsymbol{B}_u(k) & \boldsymbol{A}^{N-2}\boldsymbol{B}_{u,k+1} & \boldsymbol{A}^{N-3}\boldsymbol{B}_{u,k+2} & \cdots & \boldsymbol{B}_{u,k+N-1} \end{bmatrix} \tag{4.3f}$$

and, similarly, $\boldsymbol{S}_v(k) \in \mathbb{R}^{N \cdot n_x \times N \cdot n_v}$ is defined as

$$\boldsymbol{S}_v(k) = \begin{bmatrix} \boldsymbol{B}_v(k) & \boldsymbol{0} & \boldsymbol{0} & \cdots & \boldsymbol{0} \\ \boldsymbol{A}\boldsymbol{B}_v(k) & \boldsymbol{B}_{v,k+1} & \boldsymbol{0} & \cdots & \boldsymbol{0} \\ \boldsymbol{A}^2\boldsymbol{B}_v(k) & \boldsymbol{A}\boldsymbol{B}_{v,k+1} & \boldsymbol{B}_{v,k+2} & \cdots & \boldsymbol{0} \\ \vdots & \vdots & \vdots & \ddots & \vdots \\ \boldsymbol{A}^{N-1}\boldsymbol{B}_v(k) & \boldsymbol{A}^{N-2}\boldsymbol{B}_{v,k+1} & \boldsymbol{A}^{N-3}\boldsymbol{B}_{v,k+2} & \cdots & \boldsymbol{B}_{v,k+N-1} \end{bmatrix} \tag{4.3g}$$

with $\boldsymbol{0}$ taken as the zero matrix of appropriate dimensions.

Note the time-varying nature of each of the non-zero elements of both $\boldsymbol{S}_u(k)$ and $\boldsymbol{S}_v(k)$ above. This is because, while $\boldsymbol{A}$ stays constant, both $\boldsymbol{B}_u(k)$ and $\boldsymbol{B}_v(k)$ are time-varying. This implies that, at time instant k, for every step over the prediction horizon N these matrices are updated with new element values, based on the state vector's trajectory.

Penalty matrices $\boldsymbol{Q}$, $\boldsymbol{R}$, and $\boldsymbol{R}_{\Delta u}$ are diagonal matrices tuned experimentally. Their equivalents over the entirety of the prediction horizon, i.e. $\tilde{\boldsymbol{Q}}$, $\tilde{\boldsymbol{R}}$, and $\tilde{\boldsymbol{R}}_{\Delta u}$, are defined as:

$$\begin{gathered} \tilde{\boldsymbol{Q}} = \texttt{blkdiag}(\boldsymbol{Q}, \ldots, \boldsymbol{Q}), \tilde{\boldsymbol{R}} = \texttt{blkdiag}(\boldsymbol{R}, \ldots, \boldsymbol{R}), \text{ and} \\ \tilde{\boldsymbol{R}}_{\Delta u} = \texttt{blkdiag}(\boldsymbol{R}_{\Delta u}, \ldots, \boldsymbol{R}_{\Delta u}). \end{gathered} \tag{4.3h}$$

(The full vector-form derivation can be found in Appendix C.1.)

The quadratic form of $J(k)$ follows directly from its vector representation, and is defined as:

$$J(k) = \boldsymbol{U}^{\mathrm{T}}(k)\boldsymbol{\Gamma}(k)\boldsymbol{U}(k) + 2\boldsymbol{\Upsilon}^{\mathrm{T}}(k)\boldsymbol{U}(k) + \Theta(k), \tag{4.4a}$$

where

$$\boldsymbol{\Gamma}(k) = \boldsymbol{S}_u^{\mathrm{T}}(k)\tilde{\boldsymbol{Q}}\boldsymbol{S}_u(k) + \tilde{\boldsymbol{R}} + \tilde{\mathbf{I}}_{\Delta u}^{T}\tilde{\boldsymbol{R}}_{\Delta u}\tilde{\mathbf{I}}_{\Delta u}, \tag{4.4b}$$

$$\begin{aligned}\boldsymbol{\Upsilon}^{\mathrm{T}}(k) = {} & \boldsymbol{x}^{\mathrm{T}}(k)\boldsymbol{S}_x^{\mathrm{T}}\tilde{\boldsymbol{Q}}\boldsymbol{S}_u(k) + \boldsymbol{V}^{\mathrm{T}}(k)\boldsymbol{S}_v^{\mathrm{T}}(k)\tilde{\boldsymbol{Q}}\boldsymbol{S}_u(k) - \boldsymbol{X}_{\mathrm{ref}}^{\mathrm{T}}(k)\tilde{\boldsymbol{Q}}\boldsymbol{S}_u(k) \\ & -\boldsymbol{U}_{\mathrm{ref}}^{\mathrm{T}}(k)\tilde{\boldsymbol{R}} - \boldsymbol{u}^{\mathrm{T}}(k-1)\tilde{\mathbf{I}}_{\Delta u,\mathrm{init}}^{\mathrm{T}}\tilde{\boldsymbol{R}}_{\Delta u}\tilde{\mathbf{I}}_{\Delta u},\end{aligned} \tag{4.4c}$$

and

$$\begin{aligned}\Theta(k) = {} & 2\big(\boldsymbol{V}^{\mathrm{T}}(k)\boldsymbol{S}_v^{\mathrm{T}}(k)\tilde{\boldsymbol{Q}}\boldsymbol{S}_x\boldsymbol{x}(k) - \boldsymbol{X}_{\mathrm{ref}}^{\mathrm{T}}(k)\tilde{\boldsymbol{Q}}\boldsymbol{S}_x\boldsymbol{x}(k) - \boldsymbol{X}_{\mathrm{ref}}^{\mathrm{T}}(k)\tilde{\boldsymbol{Q}}\boldsymbol{S}_v(k)\boldsymbol{V}(k)\big) \\ & + \|\boldsymbol{S}_x\boldsymbol{x}(k)\|_{\tilde{\boldsymbol{Q}}}^2 + \|\boldsymbol{S}_v(k)\boldsymbol{V}(k)\|_{\tilde{\boldsymbol{Q}}}^2 + \|\boldsymbol{X}_{\mathrm{ref}}(k)\|_{\tilde{\boldsymbol{Q}}}^2 + \|\boldsymbol{U}_{\mathrm{ref}}(k)\|_{\tilde{\boldsymbol{R}}}^2 \\ & + \left\|\tilde{\mathbf{I}}_{\Delta u,\mathrm{init}}\boldsymbol{u}(k-1)\right\|_{\tilde{\boldsymbol{R}}_{\Delta u}}^2.\end{aligned} \tag{4.4d}$$

The full quadratic-form derivation can be found in Appendix C.2. Note that $\boldsymbol{\Gamma}(k)$ is a multiple (specifically, half) of the Hessian matrix, and is positive semi-definite. Furthermore, $\Theta(k)$ does not depend on the control-input vector and, therefore, stays constant during the optimisation.

4.2.2 Constraints

The control system is to adhere to certain constraints, namely: Bounds are placed on the allowable temperature of both x_{Z} and x_{EWH}. Furthermore, total load power cannot exceed total generated power. The converse is not necessarily true, as the solar PV array is capable of generating more power than can be usefully applied. These constraints can be represented by inequalities, which are formulated here.

To ensure load power does not exceed total generated power, the product of $\boldsymbol{p}(k)$ and $\boldsymbol{u}(k)$ cannot exceed $p_{\mathrm{target}}(k)$, i.e.

$$\boldsymbol{p}^{\mathrm{T}}(k)\boldsymbol{u}(k) \leq p_{\mathrm{target}}(k), \tag{4.5a}$$

where control-input power vector $\boldsymbol{p}(k)$ is defined as

$$\boldsymbol{p}(k) = \begin{bmatrix} -P_{\mathrm{BES,r}} & -P_{\mathrm{BES,r}} & p_{\mathrm{AHU}}(k) & P_{\mathrm{EWH,r}} \end{bmatrix}^{\mathrm{T}}. \tag{4.5b}$$

Note that the two negative BES coefficients in $\boldsymbol{p}(k)$ pertain to $u_{\mathrm{BES,gen}}(k)$ and $u_{\mathrm{BES,load}}(k)$, respectively. The first ensures power generated by the BES counteracts load power, while the second compensates for $u_{\mathrm{BES,load}}(k) \in [-1, 0]$ [p.u.], ensuring that BES load power contributes to overall load power in the inequality.

Bounds on the AHU and EWH temperatures (where l_{b} refers to lower and u_{b} to upper bounds) can be stated as

$$l_{\mathrm{b,AHU}}(k+1) \leq x_{\mathrm{Z}}(k+1) \leq u_{\mathrm{b,AHU}}(k+1), \tag{4.5c}$$

and

$$l_{\mathrm{b,EWH}}(k+1) \leq x_{\mathrm{EWH}}(k+1) \leq u_{\mathrm{b,EWH}}(k+1). \tag{4.5d}$$

Inequalities (4.5a)–(4.5d) are hard constraints that can, at times, be impossible to adhere to. Constraint parameters are introduced to convert them into soft constraints. To address the scenario in which total local generation power falls short of total demand power, constraint parameter $f_{\text{grid}}(k)$ is introduced to draw power from the grid, that is,

$$\begin{aligned} \boldsymbol{p}^{\text{T}}(k)\boldsymbol{u}(k) &\leq p_{\text{target}}(k) + f_{\text{grid}}(k) \\ \boldsymbol{p}^{\text{T}}(k)\boldsymbol{u}(k) - f_{\text{grid}}(k) &\leq p_{\text{target}}(k), \end{aligned} \tag{4.6a}$$

where $f_{\text{grid}}(k) \in [0, P_{1\phi}]$ [W], with $P_{1\phi}$ representing single-phase rated power. Energy can also be drawn from the grid to mitigate differences between reference and actual temperatures during the times of day when no solar PV and/or BES supply power are available. This is regulated by the penalty placed on f_{grid} as described in (4.8).

Similarly, to soften temperature bounds, $f_{\text{AHU}}(k)$ and $f_{\text{EWH}}(k)$ are introduced, as follows:

$$l_{\text{b,AHU}}(k+1) \leq x_{\text{Z}}(k+1) - f_{\text{AHU}}(k) \leq u_{\text{b,AHU}}(k+1), \tag{4.6b}$$

and

$$l_{\text{b,EWH}}(k+1) \leq x_{\text{EWH}}(k+1) - f_{\text{EWH}}(k) \leq u_{\text{b,EWH}}(k+1). \tag{4.6c}$$

There are no limits imposed on the allowable range of f_{AHU} and f_{EWH}, as environmental changes can cause temperature variations that exceed the AHU and EWH's ability to counteract within a single sampling period or longer. It is therefore not advisable to impose limits on these constraint parameters. Instead, these deviations are penalised heavily within an adjusted form of the objective function, as described in (4.8).

Taken together, constraint-parameter vector $\boldsymbol{f}(k)$ is defined as

$$\boldsymbol{f}(k) = \begin{bmatrix} f_{\text{grid}}(k) \\ f_{\text{AHU}}(k) \\ f_{\text{EWH}}(k) \end{bmatrix} \in \mathbb{R}^{m_f}. \tag{4.7a}$$

Additionally, define constraint-parameter sequence vector $\boldsymbol{F}(k)$ as the evolution of $\boldsymbol{f}$ over the prediction horizon N, that is,

$$\boldsymbol{F}(k) = \begin{bmatrix} \boldsymbol{f}(k) \\ \boldsymbol{f}_{k+1} \\ \vdots \\ \boldsymbol{f}_{k+N-1} \end{bmatrix} \in \mathbb{R}^{N \cdot m_f}. \tag{4.7b}$$

As constraint parameters are employed to soften hard constraints, their use necessarily entails deviation from one or more constraints. To penalise such deviations, and thereby keep them to a minimum, the parameters are included in $J(k)$, described in (4.4a), as

follows:

$$J(k) = \boldsymbol{U}^{\mathrm{T}}(k)\boldsymbol{\Gamma}(k)\boldsymbol{U}(k) + \boldsymbol{F}^{\mathrm{T}}(k)\tilde{\boldsymbol{R}}_f\boldsymbol{F}(k) + 2\boldsymbol{\Upsilon}^{\mathrm{T}}(k)\boldsymbol{U}(k) + \Theta(k), \tag{4.8a}$$

where $\boldsymbol{R}_f \in \mathbb{R}^{m_f \times m_f}$ is a sparse matrix with penalty weightings for each element of $\boldsymbol{f}(k)$ on its diagonal, and $\tilde{\boldsymbol{R}}_f \in \mathbb{R}^{N\cdot m_f \times N\cdot m_f}$ is defined as

$$\tilde{\boldsymbol{R}}_f = \texttt{blkdiag}(\boldsymbol{R}_f, \ldots, \boldsymbol{R}_f). \tag{4.8b}$$

The optimisation problem, including constraint parameters, can be formulated as

$$\boldsymbol{U}^*(k) = \arg\min_{\boldsymbol{U},\boldsymbol{F}} J(k), \tag{4.9a}$$

subject to a number of constraints, namely:

- BES constraint

$$\begin{gathered}\Big(0 \leq u_{\mathrm{BES,gen}}(k) \leq \min(c_{\mathrm{BES}}(k), 1) \text{ and } u_{\mathrm{BES,load}}(k) = 0\Big) \\ \text{or} \\ \Big(u_{\mathrm{BES,gen}}(k) = 0 \text{ and } -\min(d_{\mathrm{BES}}(k), 1) \leq u_{\mathrm{BES,load}}(k) \leq 0\Big),\end{gathered} \tag{4.9b}$$

  where $c_{\mathrm{BES}}(k)$ and $d_{\mathrm{BES}}(k)$ are the maximum theoretical charge and discharge power possible, respectively, based on the BES's present SoC, and maximum rated power is represented by unity per-unit power (the '$\min(a, b)$' function returns the smaller of the two input values).

- Integer control-input constraint

$$\boldsymbol{u}_{\mathrm{b}}(k) \in \{0, 1\}^{m_{\mathrm{b}}}. \tag{4.9c}$$

- Power constraint

$$\boldsymbol{p}^{\mathrm{T}}(k)\boldsymbol{u}(k) - f_{\mathrm{grid}}(k) \leq p_{\mathrm{target}}(k), \tag{4.9d}$$

  where

$$f_{\mathrm{grid}}(k) \in [0, P_{1\phi}]. \tag{4.9e}$$

- AHU temperature bounds

$$\begin{aligned}-\tilde{\mathbf{1}}_{\mathrm{b,AHU}}^{\mathrm{T}}\boldsymbol{B}_{\mathrm{AHU},u}(k)u_{\mathrm{AHU}}(k) + f_{\mathrm{AHU}}(k) \leq \tilde{\mathbf{1}}_{\mathrm{b,AHU}}^{\mathrm{T}}\Big(&\boldsymbol{A}_{\mathrm{AHU}}\boldsymbol{x}_{\mathrm{AHU}}(k) + \\ &\boldsymbol{B}_{\mathrm{AHU},v}v_{\mathrm{AHU}}(k)\Big) - l_{\mathrm{b,AHU}}(k+1),\end{aligned} \tag{4.9f}$$

and

$$\tilde{\mathbf{1}}_{\mathrm{b,AHU}}^{\mathrm{T}}\boldsymbol{B}_{\mathrm{AHU},u}(k)u_{\mathrm{AHU}}(k) - f_{\mathrm{AHU}}(k) \leq u_{\mathrm{b,AHU}}(k+1) - \tilde{\mathbf{1}}_{\mathrm{b,AHU}}^{\mathrm{T}}\Big(\boldsymbol{A}_{\mathrm{AHU}}\boldsymbol{x}_{\mathrm{AHU}}(k) + \boldsymbol{B}_{\mathrm{AHU},v}v_{\mathrm{AHU}}(k)\Big), \tag{4.9g}$$

where

$$\tilde{\mathbf{1}}_{\mathrm{b,AHU}} = \begin{bmatrix} 1 & 0 & \cdots & 0 \end{bmatrix}^{\mathrm{T}} \in \mathbb{R}^{n_{\mathrm{AHU}}}.$$

- EWH temperature bounds

$$-b_{\mathrm{EWH},u}u_{\mathrm{EWH}}(k) + f_{\mathrm{EWH}}(k) \leq a_{\mathrm{EWH}}x_{\mathrm{EWH}}(k) + \boldsymbol{B}_{\mathrm{EWH},v}(k)\boldsymbol{v}_{\mathrm{EWH}}(k) - l_{\mathrm{b,EWH}}(k+1), \tag{4.9h}$$

and

$$b_{\mathrm{EWH},u}u_{\mathrm{EWH}}(k) - f_{\mathrm{EWH}}(k) \leq u_{\mathrm{b,EWH}}(k+1) - \Big(a_{\mathrm{EWH}}x_{\mathrm{EWH}}(k) + \boldsymbol{B}_{\mathrm{EWH},v}(k)\boldsymbol{v}_{\mathrm{EWH}}(k)\Big). \tag{4.9i}$$

Auxiliary vector $\tilde{\mathbf{1}}_{\mathrm{b,AHU}}$ above serves only as a means to obtain x_{Z} from $\boldsymbol{x}_{\mathrm{AHU}}$.

4.2.3 Apply Optimal Control Input to Power Nodes

At each time step k the first entry in optimal control-input sequence $\boldsymbol{U}^*(k)$ is applied to the system plant. This can be translated to the power-nodes framework as follows. Recall that

$$\boldsymbol{u}(k) = \begin{bmatrix} u_{\mathrm{BES,gen}}(k) & u_{\mathrm{BES,load}}(k) & u_{\mathrm{AHU}}(k) & u_{\mathrm{EWH}}(k) \end{bmatrix}^{\mathrm{T}} = \begin{bmatrix} \boldsymbol{u}_{\mathrm{c}}^{\mathrm{T}}(k) & \boldsymbol{u}_{\mathrm{b}}^{\mathrm{T}}(k) \end{bmatrix}^{\mathrm{T}}. \tag{4.10}$$

No standing losses are considered with respect to the BES, and so $w_{\mathrm{BES,s}}(k) = 0$ is always true. Optimal continuous-valued control-input vector $\boldsymbol{u}_{\mathrm{c}}^*(k)$ determines $p_{\mathrm{BES,gen}}(k)$ and $p_{\mathrm{BES,load}}(k)$.

Load power $p_{\mathrm{AHU,load}}(k)$ and $p_{\mathrm{EWH,load}}(k)$ are determined by $\boldsymbol{u}_{\mathrm{b}}^*(k)$.

The grid is also considered to be a controllable power node, covering shortfalls in generation from the BES and solar PV array. Grid generation power $p_{\mathrm{grid,gen}}(k)$ is equal to constraint parameter $f_{\mathrm{grid}}(k)$.

No new information applicable to uncontrollable generator nodes' $p_{\mathrm{gen}}(k)$, or uncontrollable load nodes' $p_{\mathrm{load}}(k)$ is gained from the optimisation output. The diverse load's demand must always be met, and can, therefore, not have any unmet load ($w_{\mathrm{diverse,f}}(k) = 0$).

The amount of potential energy to be curtailed, due to there being no useful application thereof and the inability of the electrical grid to absorb energy from the household, can be determined from the optimisation procedure's output. This is assigned to forced waste $w_{\mathrm{PV,f}}(k)$.

At the next discrete-time instant, the optimisation process is repeated with $p_{\text{target}}(k+1)$, the difference between solar PV supply and diverse load demand at $k+1$.

4.3 Control-Input Reference Generation

While $\boldsymbol{X}_{\text{ref}}(k)$ consists of desired reference values fed into the controller, the procedure for determining $\boldsymbol{U}_{\text{ref}}(k)$ concerns the solution of an optimal allocation problem at every step of the prediction horizon. In this manner, a sequence of control-input references are generated.

The aim is to closely match $p_{\text{target}}(k)$, which is defined as

$$p_{\text{target}}(k) = \sum_{\xi \geq 0} p_{\text{gen}}(k) - \sum_{\xi \leq 0} p_{\text{load}}(k) = p_{\text{PV,gen}}(k) - p_{\text{diverse,load}}(k), \tag{4.11}$$

through means of a combination of the available control inputs. Continuous control of the BES allows for flexibility in the allocation, since both the AHU (although it has time-varying power consumption) and EWH only permit integer control.

An illustration of the goal in mind when generating $\boldsymbol{U}_{\text{ref}}(k)$ is shown in Figure 4.2. Suppose that, at time step k, $p_{\text{target}}(k)$ is insufficient for both the AHU and EWH to be utilised in the power allocation. Suppose also that the BES has a high SoC at time step k. Given the described scenario, the optimisation procedure concludes that BES discharge is preferred over allowing one of the controllable loads to remain inactive and let the surplus solar-inverter output power go to waste.

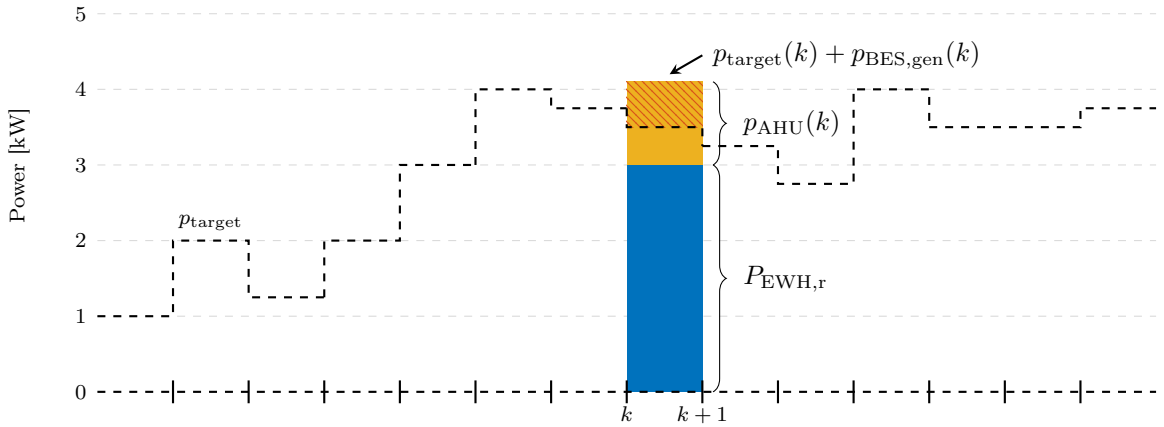

Figure 4.2: An example maximal allocation. The area hatched in orange represents $p_{\text{BES,gen}}(k)$.

The controllable-node arrangement at a given time step depends on the outcome of the optimal-allocation problem formulated below. Note that in the BES model, input and output power are not viewed as opposing sides of one input variable's allowable range, but instead as two separate variables altogether. That distinction need not apply here, as the BES model does not form part of the optimal control-input allocation procedure,

and a single BES control input can be used. This is preferred, as it allows for an easier problem formulation. Therefore, define $u'_{\text{BES}}(k)$ as a combination of both $u_{\text{BES,gen}}(k)$ and $u_{\text{BES,load}}(k)$, that is,

$$-\min(d_{\text{BES}}(k), 1) \leq u'_{\text{BES}}(k) \leq \min(c_{\text{BES}}(k), 1) \text{ [p.u.]}. \tag{4.12}$$

Grouping $u'_{\text{BES}}(k)$ with $\boldsymbol{u}_{\text{b}}(k)$ yields augmented control vector $\boldsymbol{u}'(k)$, i.e.

$$\boldsymbol{u}'(k) = \begin{bmatrix} u'_{\text{BES}}(k) & u_{\text{AHU}}(k) & u_{\text{EWH}}(k) \end{bmatrix}^{\text{T}}. \tag{4.13}$$

Vector $\boldsymbol{p}'(k)$ converts $\boldsymbol{u}'(k)$ into the power domain, and is defined as

$$\boldsymbol{p}'(k) = \begin{bmatrix} P_{\text{BES,r}} & p_{\text{AHU}}(k) & P_{\text{EWH,r}} \end{bmatrix}^{\text{T}}, \tag{4.14}$$

where $p_{\text{AHU}}(k)$ is defined by (3.20).

Control-input allocation objective function $J_{\text{ref},u}(k)$ can subsequently be defined as

$$\begin{aligned} J_{\text{ref},u}(k) &= \left(p_{\text{target}}(k) - \boldsymbol{p}'^{\text{T}}(k)\boldsymbol{u}'(k)\right)^2 \\ &= \boldsymbol{u}'^{\text{T}}(k)\boldsymbol{H}(k)\boldsymbol{u}'(k) - 2\, p_{\text{target}}(k)\boldsymbol{p}'^{\text{T}}(k)\boldsymbol{u}'(k) + p^2_{\text{target}}(k), \end{aligned} \tag{4.15a}$$

where $\boldsymbol{H}(k)$ is positive semi-definite[1], and defined as

$$\boldsymbol{H}(k) = \begin{bmatrix} P^2_{\text{BES,r}} & P_{\text{BES,r}}\, p_{\text{AHU}}(k) & P_{\text{BES,r}}\, P_{\text{EWH,r}} \\ P_{\text{BES,r}}\, p_{\text{AHU}}(k) & p^2_{\text{AHU}}(k) & p_{\text{AHU}}(k)\, P_{\text{EWH,r}} \\ P_{\text{BES,r}}\, P_{\text{EWH,r}} & p_{\text{AHU}}(k)\, P_{\text{EWH,r}} & P^2_{\text{EWH,r}} \end{bmatrix}. \tag{4.15b}$$

Equation (4.15a) is in the quadratic form, under the assumption that $p_{\text{AHU}}(k)$ stays constant for the duration of a sampling interval. This form can be used to formulate an optimisation problem, i.e.

$$\begin{aligned} \boldsymbol{u}'^{*}_{\text{ref}}(k) = \; & \arg\min_{\boldsymbol{u}'(k)} J_{\text{ref},u}(k) \\ & \text{subject to } -\min(d_{\text{b}}(k), 1) \leq u'_{\text{BES}}(k) \leq \min(c_{\text{b}}(k), 1) \\ & \text{and } u_{\text{AHU}}(k), u_{\text{EWH}}(k) \in \{0, 1\}. \end{aligned} \tag{4.16}$$

Since (4.15a) is convex, an optimal augmented control-input vector $\boldsymbol{u}'^{*}_{\text{ref}}(k)$ can be found. A conversion to $\boldsymbol{u}_{\text{ref}}(k)$ from $\boldsymbol{u}'_{\text{ref}}(k)$ follows, based on the value of $u'^{*}_{\text{BES,ref}}(k)$. As the BES can only be in a charge, discharge or inactive state at any given point in time, only one of $u_{\text{BES,gen,ref}}(k)$ and $u_{\text{BES,load,ref}}(k)$ can be non-zero. If $u'^{*}_{\text{BES,ref}}(k)$ is negative, $u_{\text{BES,gen,ref}}(k)$ is assigned its absolute value, and vice versa. Otherwise, both the BES reference generation

[1] This is done intentionally. This way, scalar $\boldsymbol{u}'^{\text{T}}(k)\boldsymbol{H}(k)\boldsymbol{u}'(k)$ is non-negative for every (non-zero) vector $\boldsymbol{u}'(k)$, a necessary condition for convexity (i.e. that the local minimum is also a global minimum).

and load power are set to zero. The problem is solved using the Gurobi optimisation suite [36] (in concert with MATLAB).

4.4 Algorithmic Cost Calculation

Optimisation problem (4.9a) is a mixed-integer programme as it contains both continuous- and integer-input variables to be optimised.

While an optimal value, within a given range, can be found for continuous-valued input variables, the same cannot be said of their binary counterparts. Instead, the cost associated with each integer-input enumeration is calculated and the least-cost option among them is chosen as the optimal input. The set containing all integer-control input enumerations $\mathcal{U}$ is defined as

$$\mathcal{U} = \left\{ \begin{bmatrix} 0 \\ 0 \end{bmatrix}, \begin{bmatrix} 0 \\ 1 \end{bmatrix}, \begin{bmatrix} 1 \\ 0 \end{bmatrix}, \begin{bmatrix} 1 \\ 1 \end{bmatrix} \right\}. \tag{4.17}$$

At each time step k a mixed-integer problem is solved via the "branch and bound" method, as described in [13], to obtain the optimal control-input sequence.

Making use of the depth-first search with backtracking [37], the method evaluates nodes in a decision tree consisting of possible integer-input sequences. At each of the nodes, successive versions of $J(k)$ are solved up to prediction step $n = 1, 2, \ldots, N$. These steps are also used as depth levels of the tree. The branch sequence being traversed is commonly referred to as the 'candidate solution'.

Figure 4.3 depicts the search algorithm in progress, with an example path highlighted in blue. Starting from an initial optimal cost $J^*(k) = \infty$, the method heuristically moves down the branch containing the first entry in set $\mathcal{U}$ described above. From there, the method moves down the branch representing the first entry in $\mathcal{U}$ once more. This procedure is repeated until the N^{th} level of the tree is reached. Initially, there exists no incumbent optimal control-input sequence with which to compare the present candidate sequence, and thus the first 'leaf' (i.e. N^{th} level) node of the tree assumes the role of $\boldsymbol{U}^*(k)$. This node sequence is coloured orange in Figure 4.3a.

The tree is recursively traversed from this node, backtracking up the tree and moving down to other potential candidate solutions as far as their cumulative cost remains less than the incumbent optimal. If, once a new leaf node is reached, the candidate cost is less than that of the incumbent optimal, it assumes the role of $\boldsymbol{U}^*(k)$ until a lower-cost solution is found. This procedure repeats itself until the tree has been 'pruned', that is, all branches have been explored. At this point, the incumbent optimal control-input sequence is returned as the solution to optimisation problem (4.9a).

Algorithm 3 describes the recursive traversal of the search tree, where `cost_vars` is a data structure containing the following vectors:

- State and disturbance-input sequences $\boldsymbol{X}(k)$ and $\boldsymbol{V}(k)$;
- Incumbent optimal sequences $\boldsymbol{U}^*(k)$ and $\boldsymbol{F}^*(k)$, and $J^*(k)$;
- Candidate sequences $\boldsymbol{U}_{\text{cand}}(k)$ and $\boldsymbol{F}_{\text{cand}}(k)$, and $J_{\text{cand}}(k)$;
- State- and control-input reference sequences $\boldsymbol{X}_{\text{ref}}(k)$ and $\boldsymbol{U}_{\text{ref}}(k)$;
- As well as stacked state, control-input and disturbance-input matrices $\boldsymbol{S}_x$, $\boldsymbol{S}_u(k)$, and $\boldsymbol{S}_v(k)$, respectively.

Algorithm 3 Branch & Bound: Depth-First Search with Backtracking

Initialise $J^*(k) \leftarrow \infty$
function $[\boldsymbol{U}^*(k),\ \boldsymbol{F}^*(k),\ J^*(k)]$ = `BB_DFS_BT` (`cost_vars`, i)
  Obtain $p_{\text{AHU},k+i-1}$ using (3.20)
  Obtain $\boldsymbol{u}_{\text{ref},k+i-1}$ using (4.16)
  Update i^{th} row of $\boldsymbol{S}_u(k)$ with $\boldsymbol{B}_{u,k+i-1}$
  Update i^{th} row of $\boldsymbol{S}_v(k)$ with $\boldsymbol{B}_{v,k+i-1}$
  for each $\boldsymbol{u}_{\text{b}} \in \mathcal{U}$ **do**
    $J_{\text{cand}}(k) \leftarrow \min\limits_{\boldsymbol{U},\boldsymbol{F}} J(k)\Big|_i$ subject to constraints (4.9b)–(4.9i)
    $\left[\boldsymbol{U}_{\text{cand}}(k)\Big|_i, \boldsymbol{F}_{\text{cand}}(k)\Big|_i\right] \leftarrow \arg\min\limits_{\boldsymbol{U},\boldsymbol{F}} J(k)\Big|_i$ subject to constraints (4.9b)–(4.9i)
    if $J_{\text{cand}}(k) < J^*(k)$ **then**
      $\boldsymbol{x}_{k+i}(k) \leftarrow \boldsymbol{A}\boldsymbol{x}_{k+i-1} + \boldsymbol{B}_{u,k+i-1}\boldsymbol{u}_{k+i-1} + \boldsymbol{B}_{v,k+i-1}\boldsymbol{v}_{k+i-1}$
      if $i < N$ **then**
        Update `cost_vars` with newly-computed values, vectors and matrices
        $\left[\boldsymbol{U}^*(k)\Big|_{i+1}, J^*(k)\Big|_{i+1}\right] \leftarrow$ `BB_DFS_BT`(`cost_vars`, $i+1$)
      else
        $J^*(k) = J_{\text{cand}}(k)$
        $\boldsymbol{U}^*(k) = \boldsymbol{U}_{\text{cand}}(k)$
        $\boldsymbol{F}^*(k) = \boldsymbol{F}_{\text{cand}}(k)$
      end if
    end if
  end for
end function

From the continuous-continuous and binary-continuous bilinear products in (4.1), it can be seen that the system is "mildly" nonlinear. Sequential quadratic programming (SQP) has been shown to be effective in dealing with nonlinear constraints [24], and is used within the MATLAB programming environment to perform the minimisation of $J(k)$.

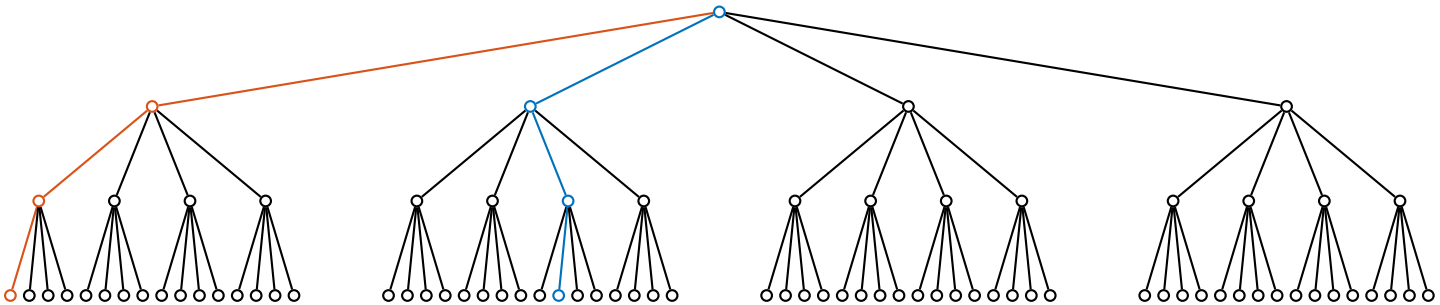

(a) The complete decision tree for $N = 3$. The first candidate solution is shown in orange, with an example explored path highlighted in blue.

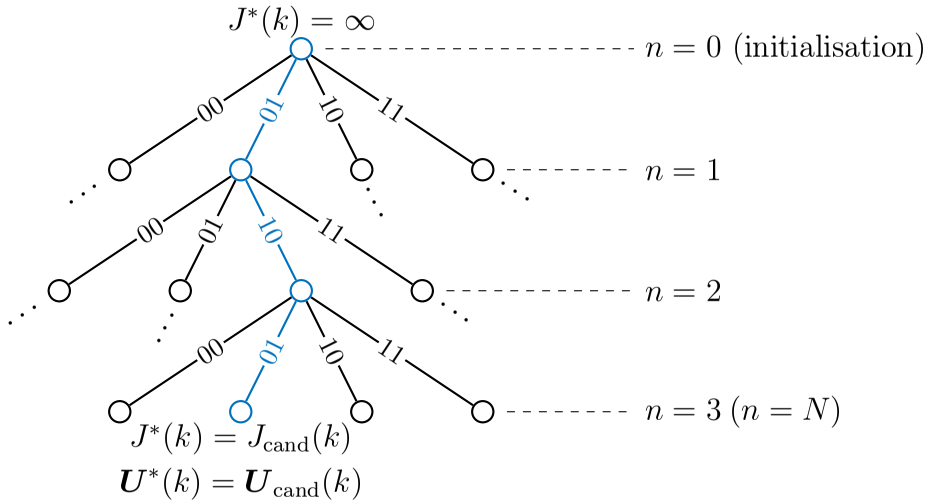

(b) A magnified view of the example explored path, annotated. The leaf node of the example candidate path has a lower cost than the incumbent optimal, and thus becomes the new optimal solution.

Figure 4.3: An example decision-tree traversal, illustrated.

4.5 Initial-Bound Guess

The exponential computational-burden growth inherent in decision trees, as horizon N is lengthened, can be remedied in part by recycling the control-input sequence generated at time instant $k-1$ to yield a "best-guess" initial cost J_{init} at time instant k. The control-input sequence is calculated as part of the receding-horizon policy, but, since only the first entry is applied to the plant, would otherwise be discarded.

Cost bound J_{init} shortens the search for the optimal control-input sequence by immediately excluding all alternatives more costly than repeating the previously-calculated control sequence, compensating for the now-obsolete control-input vector $\boldsymbol{u}(k-1)$ by making use of $\boldsymbol{u}(k+N-2)$ twice, as Algorithm 4 shows.

Algorithm 4 Initial-Bound Guess

function $[J_{\text{init}}(k)]$ = `BOUND_GUESS` (`cost_vars`)
  $\boldsymbol{U}_{\text{b,guess}}(k) \leftarrow \begin{bmatrix}\boldsymbol{u}_{\text{b}}(k-1) & \boldsymbol{u}_{\text{b},k} & \dots & \boldsymbol{u}_{\text{b},k+N-2} & \boldsymbol{u}_{\text{b},k+N-2}\end{bmatrix}^{\text{T}}$
  for i from 1 to $N-1$ **do**
    Obtain $p_{\text{AHU},k+i-1}$ using (3.20)
    Obtain $\boldsymbol{u}_{\text{ref}}(k+i-1)$ using (4.16)
    Update $\boldsymbol{S}_u(k)$ with $\boldsymbol{B}_{u,k+i-1}$ and $\boldsymbol{S}_v(k)$ with $\boldsymbol{B}_{v,k+i-1}$
    $\left[\boldsymbol{U}_{\text{guess}}(k)\Big|_i, \boldsymbol{F}_{\text{guess}}(k)\Big|_i\right] \leftarrow \arg\min_{\boldsymbol{U},\boldsymbol{F}} J(k)\Big|_i$
    $\boldsymbol{x}_{k+i}(k) \leftarrow \boldsymbol{A}\boldsymbol{x}_{k+i-1} + \boldsymbol{B}_{u,k+i-1}\boldsymbol{u}_{k+i-1} + \boldsymbol{B}_{v,k+i-1}\boldsymbol{v}_{k+i-1}$
  end for
  $J_{\text{init}}(k) \leftarrow \min_{\boldsymbol{U},\boldsymbol{F}} J(k)\Big|_N$
end function

4.6 Simulation Setup

For the predictive controller to be evaluated, allowable temperature bounds on both the AHU and EWH are to be defined. Additionally, controller performance at a given horizon length is to be compared against the performance of a controller without estimations of future states. To serve as baseline, a rules-based controller is described for this purpose.

4.6.1 Choice of Temperature Bounds and References

Air-Handling Unit

Temperature bounds for the AHU are chosen to be active between 07:00 and 19:00, every day of the week, under the assumption that the room to be air-conditioned is in frequent use. Furthermore, the allowable room temperature during use is limited to between 22 °C and 30 °C, with a reference temperature of 26 °C, similar to the values used in [18]. The AHU state reference weight in the objective function is tuned experimentally and enjoys priority.

Electric Water Heater

The EWH bounds are less subjective than those of the AHU due to the discovery of Legionnaires' disease[2], a severe form of pneumonia caused by a type of bacteria called legionella, that spreads through water systems [39]. A temperature spectrum is reproduced from [40] in Figure 4.4, showing the behaviour of legionella at various temperatures.

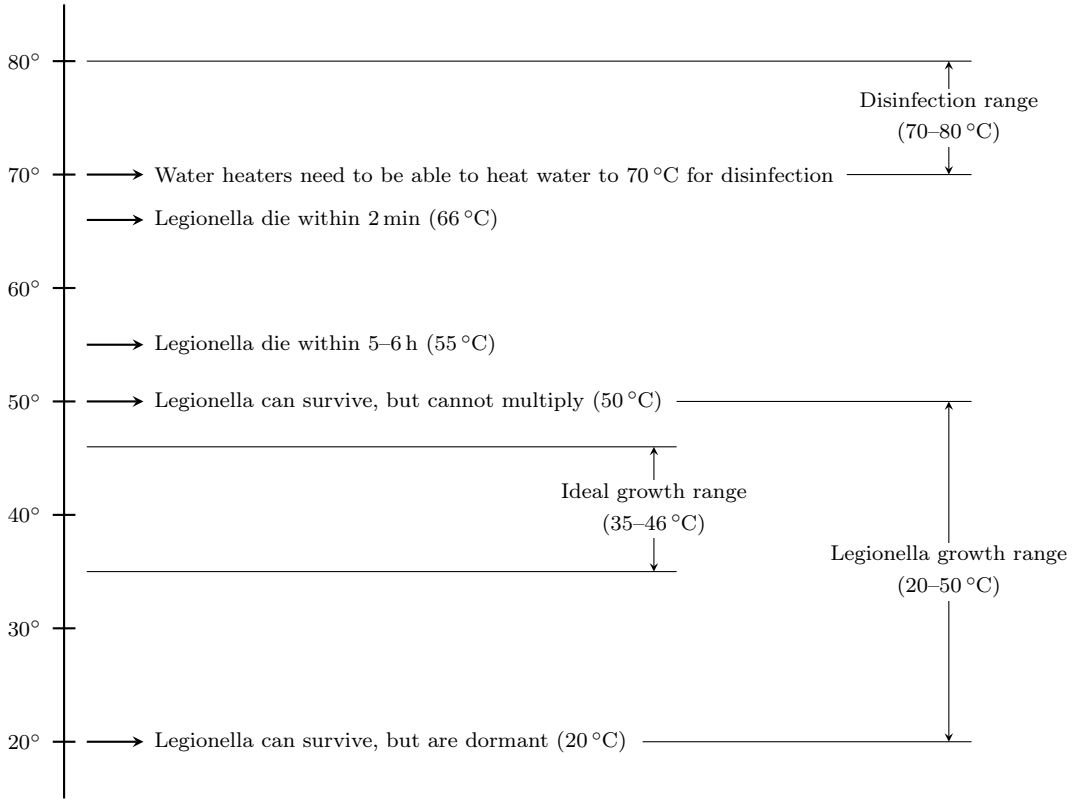

Figure 4.4: Legionella behaviour at various temperatures.

From Figure 4.4, it can be seen that, ideally, water residing within the EWH tank should not fall below 50 °C. To reduce the likelihood of scalding, a reference temperature of 60 °C is chosen [39], and is increased to 65 °C between 07:00 and 19:00 as a heuristic to prioritise storing energy in the EWH during hours of the day when the PV is likely to produce power. Lastly, an upper bound of 70 °C is selected, which skirts the region of disinfection ($\geq$ 70 °C).

4.6.2 Baseline Controller

In order to demonstrate improvements the predictive controller might bring about, a baseline is established using a rules-based hierarchical control scheme. Loads are prioritised in the following order: diverse load, EWH, AHU, and BES charge state. The power source hierarchy is as follows: solar PV array, BES discharge state, and electrical grid.

[2]The disease takes its name from the incident in which it was discovered, involving a gathering of the American *Legion* in Philadelphia in 1976 [38].

Figure 4.5 depicts the baseline controller. At a given time step k, the controller steps through a series of conditional statements in order to meet power requirements in the order listed above. Figure 4.5 makes use of the power-nodes notation described in Section 3.1. All values are initialised to zero, unless otherwise specified.

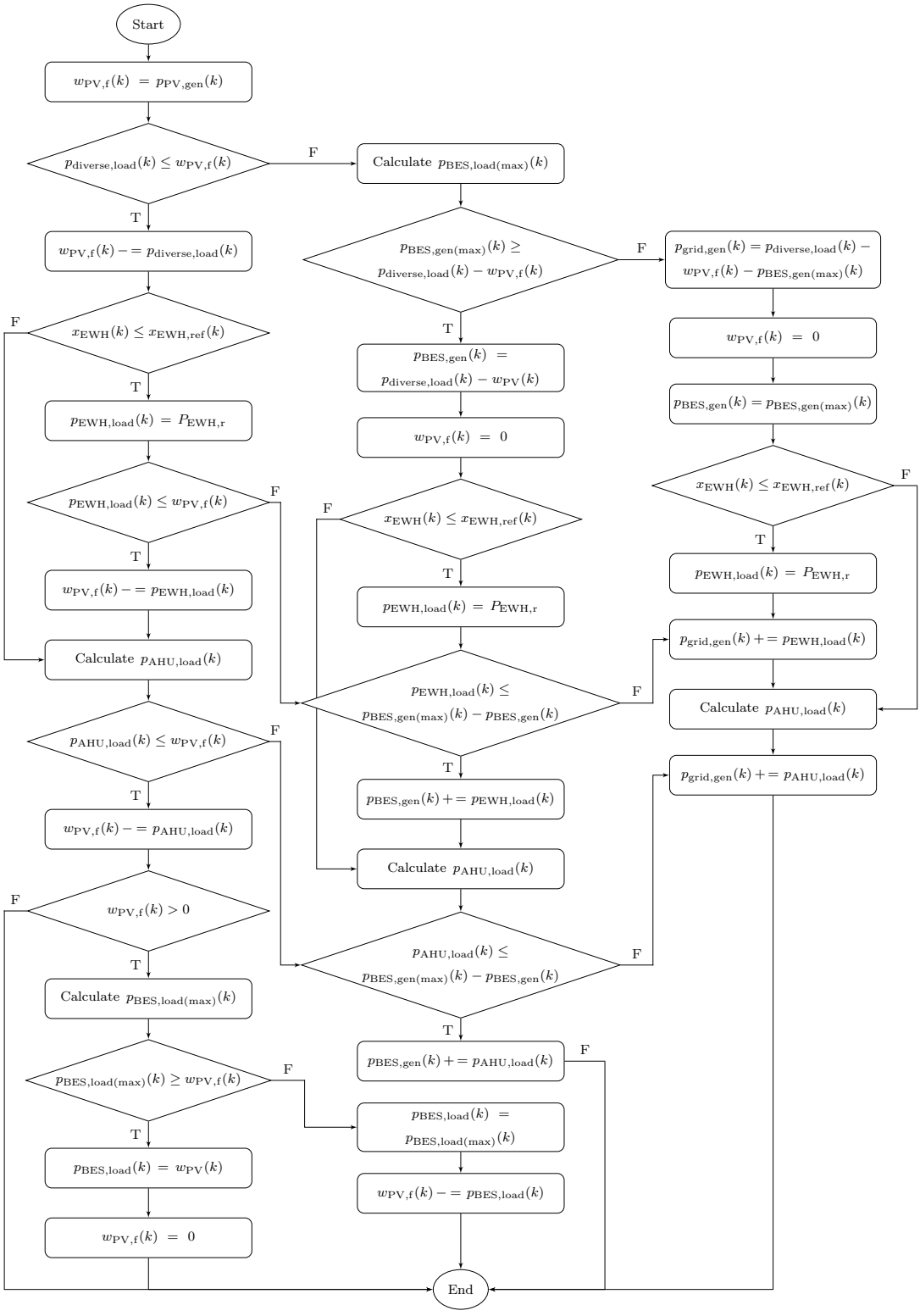

Figure 4.5: The hierarchical rules-based controller used as baseline for performance comparisons.

4.7 Simulation Results

A number of results are presented here. First, a comparison of the controller's performance at different horizon lengths is done, using data from each of the four seasons. A detailed examination of the summertime simulation, which depicts the controller operation most clearly, follows. Thereafter, the impact of variation in the penalty weighting of integer control inputs' commutation is investigated. Lastly, computational load reduction due to the addition of the initial-bound guess algorithm is validated.

4.7.1 Performance Comparison Across Horizon Lengths

In order to evaluate the controller's performance across different horizon lengths, the following key criteria are used:

- The amount of curtailed solar energy, representing lost solar PV array productivity,
- The amount of energy drawn from the electrical network, representing grid dependency, and
- Temperature-bound violations for both the EWH (any time of day) and AHU (between 07:00 and 19:00), representing a loss of comfort due to the controller's actions. These violations are measured in Kelvin-hours [K h].

A week-long simulation in each of the four seasons is done so as to evaluate the control scheme across a diverse set of conditions, starting with spring of 2017.

For each of the week-long simulations, the same initial state is used, defined as

$$\boldsymbol{x}(0) = \begin{bmatrix} \boldsymbol{x}_{\text{BES}}^{\text{T}}(0) & \boldsymbol{x}_{\text{AHU}}^{\text{T}}(0) & \boldsymbol{x}_{\text{EWH}}^{\text{T}}(0) \end{bmatrix}^{\text{T}}, \tag{4.18a}$$

where

$$\boldsymbol{x}_{\text{BES}}(0) = \begin{bmatrix} 0.05 & 0.15 \end{bmatrix}^{\text{T}} \text{p.u.}, \tag{4.18b}$$

$$\boldsymbol{x}_{\text{AHU}}(0) = \begin{bmatrix} 15 & \cdots & 15 \end{bmatrix}^{\text{T}} \text{°C}, \tag{4.18c}$$

and

$$x_{\text{EWH}}(0) = 45\text{°C}. \tag{4.18d}$$

Controller performance evaluation results across different horizon lengths are compared at the same amount of control effort, defined as the average frequency of integer control-input switching, i.e. $\bar{f}_{\text{AHU}}$ and $\bar{f}_{\text{EWH}}$ for the respective integer control inputs[3].

The general trend as the prediction horizon increases is of primary interest. Numerical values of the key criteria are of secondary importance, as these values can vary a great deal,

[3]Since the AHU is only active for 12 hours a day, its commutation is averaged over 84 hours, as opposed to the EWH's 168 hours (the amount of hours in a week).

depending on the size of system components and the penalty placed on integer control inputs' commutation. Instead, for the same amount of control-input effort, all else being equal, controllers with longer horizons are expected to outperform their short-horizon counterparts due to their informational advantage.

Spring

Figure 4.6 shows curtailed solar PV energy and grid supply required as a function of horizon length for the 16–23 October 2017 period. A noticeable improvement from the rules-based controller is observed.

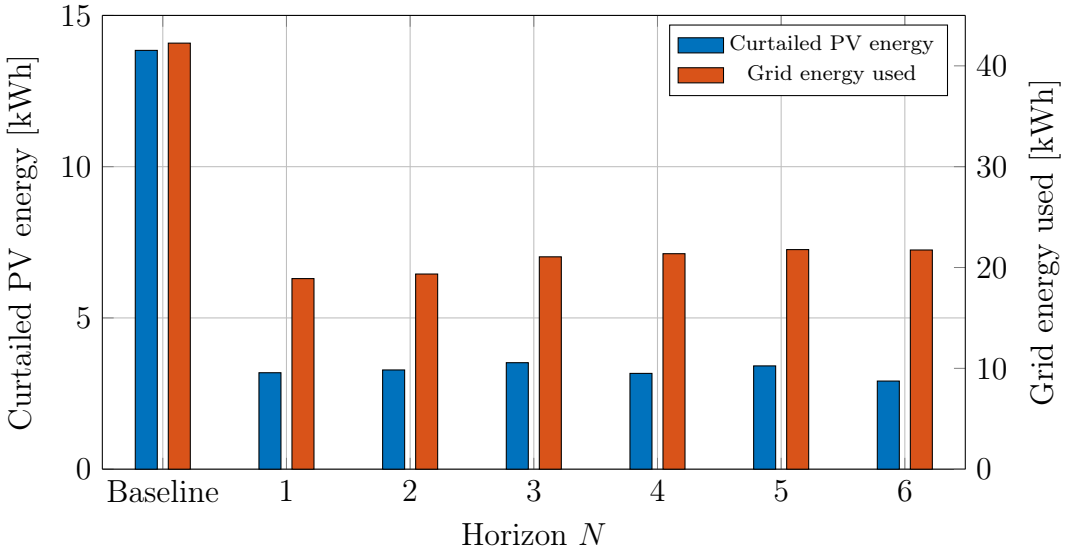

Figure 4.6: Curtailed solar energy and grid energy used compared across different horizons for a week in October 2017 ($\bar{f}_{\text{AHU}} = 0.71\,\text{h}^{-1}$ and $\bar{f}_{\text{EWH}} = 0.50\,\text{h}^{-1}$).

As the horizon increases, a trade-off takes place: the controller opts to consume slightly more grid energy in order to substantially reduce thermal discomfort. This can be seen from Figure 4.7, which displays a marked decline in cumulative EWH temperature bound violation as the horizon increases, keeping in mind that the control effort is kept constant by experimentally tuning the penalty matrices' diagonal entries.

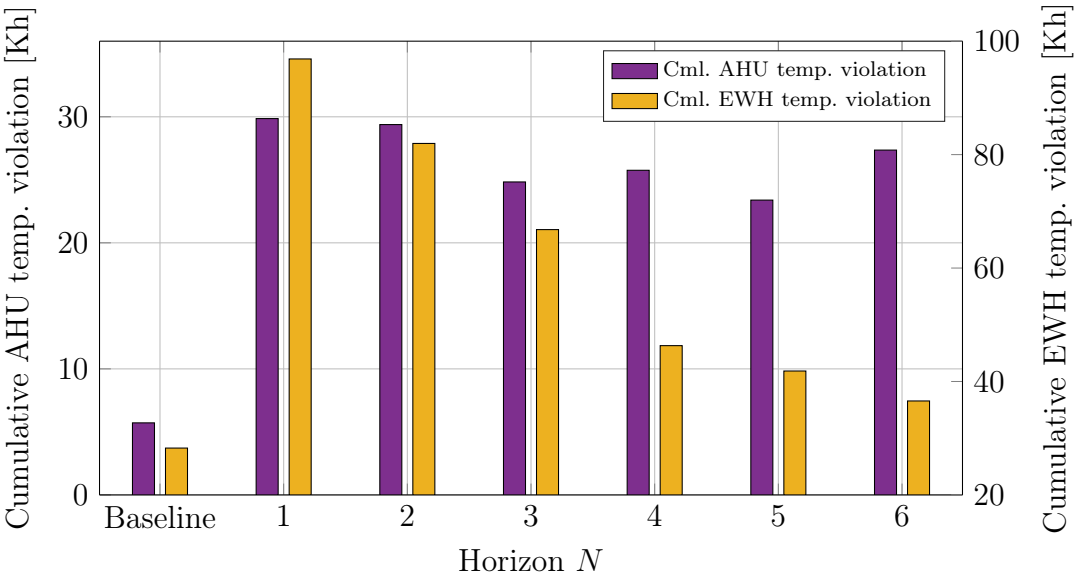

Figure 4.7: Temperature bound violations for the AHU and EWH compared across different horizons for a week in October 2017 ($\bar{f}_{\text{AHU}} = 0.71\,\text{h}^{-1}$ and $\bar{f}_{\text{EWH}} = 0.50\,\text{h}^{-1}$).

Summer

The summertime simulation makes use of data from the first week of December 2017. The controller performs well in clear-skied summer conditions, as would be expected. This can be seen from the improvements longer horizons bring about, as evidenced by Figures 4.8 and 4.9. Significant reductions in curtailed energy and grid dependency can be observed.

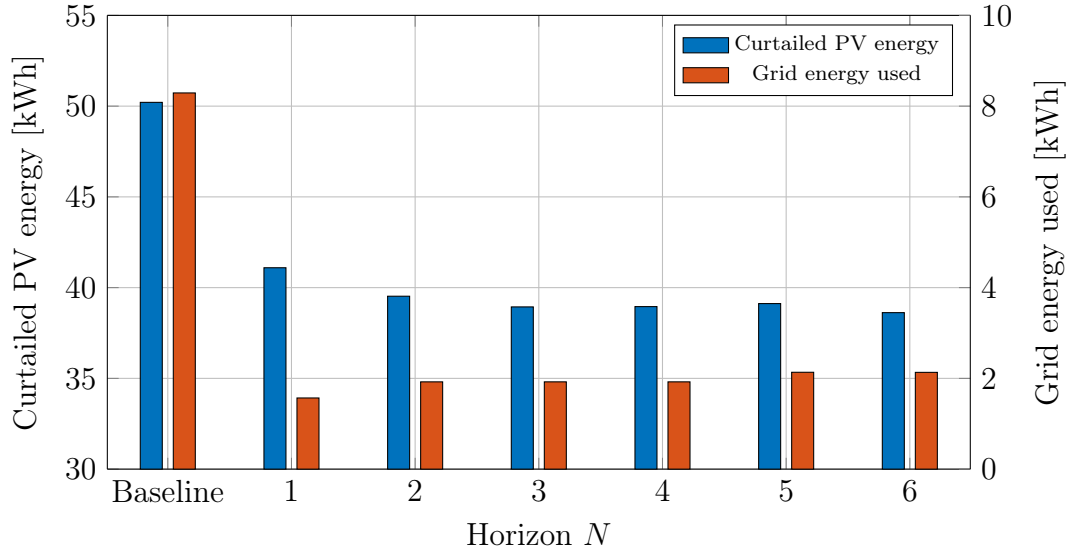

Figure 4.8: Curtailed solar and grid energy used compared across different horizons for a week in December 2017 ($\bar{f}_{\text{AHU}} = 0.26\,\text{h}^{-1}$ and $\bar{f}_{\text{EWH}} = 0.60\,\text{h}^{-1}$).

The trade-off observed in the springtime simulation is also observed here. By allowing a slight increase in grid dependency, longer prediction horizons orchestrate a significant

reduction in the EWH temperature bound violation. A clear indication that longer horizons yield superior results can be seen from Figure 4.9: A noticeable reduction in both temperature bound violations is observed between the one- and two-step horizon simulations, but no real change can be reported from the two-step to the four-step horizon. While keeping control effort constant, only when looking five steps, or more, ahead is a lower-cost alternative control-input sequence found.

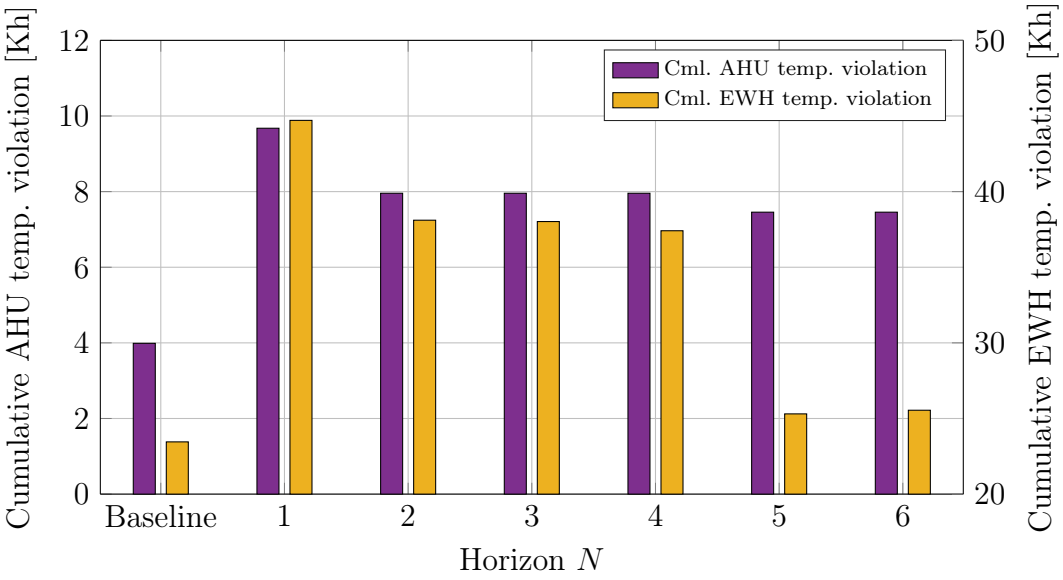

Figure 4.9: Performance comparison of different horizons for a week in December 2017 ($\bar{f}_{\text{AHU}} = 0.26\,\text{h}^{-1}$ and $\bar{f}_{\text{EWH}} = 0.60\,\text{h}^{-1}$).

Autumn

The simulation done in autumn makes use of data from the first week of April 2018. The most striking difference between the autumn simulations and those of both spring and summer is the decrease in solar radiation (Figure 4.10, as opposed to Figures 4.6 and 4.8).

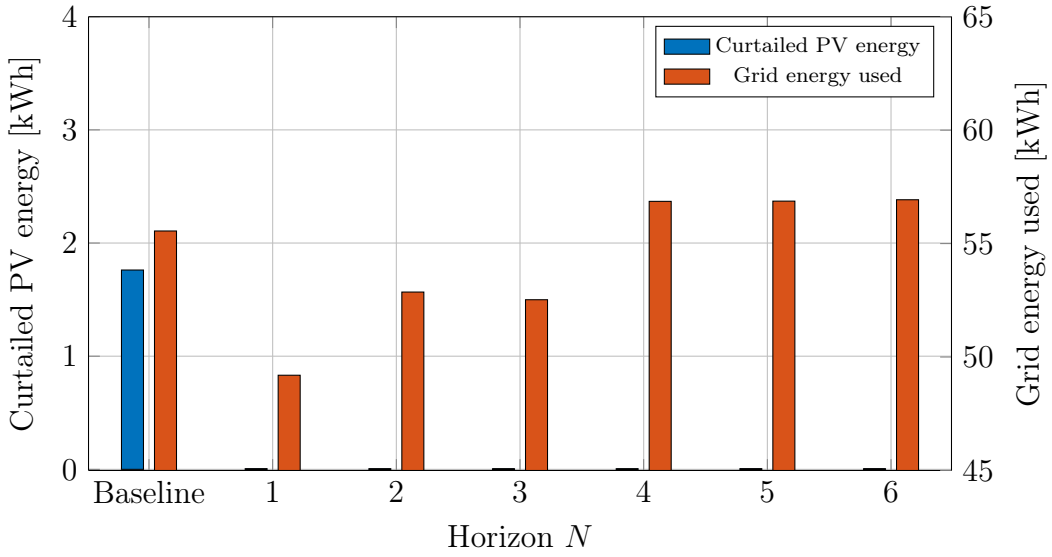

Figure 4.10: Performance comparison of different horizons for a week in December 2017 ($\bar{f}_{\text{AHU}} = 0.71\,\text{h}^{-1}$ and $\bar{f}_{\text{EWH}} = 0.45\,\text{h}^{-1}$).

Under these conditions, at longer prediction horizons the controller opts to increase grid dependency in favour of lowering temperature bound violations, as is clear from the dramatic reduction in EWH cumulative temperature bound violation depicted in Figure 4.11.

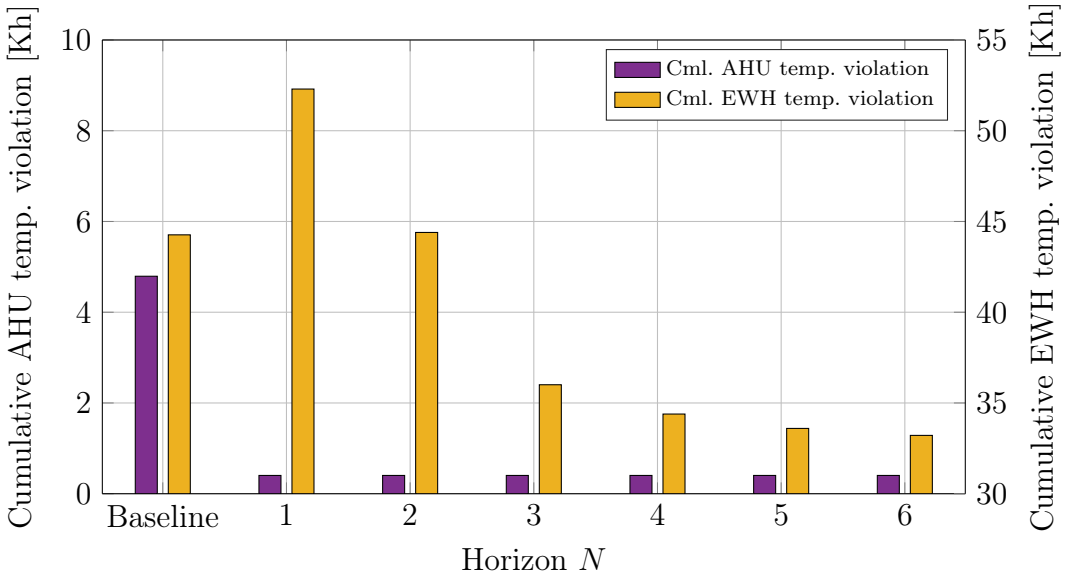

Figure 4.11: Temperature bound violations for the AHU and EWH compared across different horizons for a week in April 2018 ($\bar{f}_{\text{AHU}} = 0.71\,\text{h}^{-1}$ and $\bar{f}_{\text{EWH}} = 0.54\,\text{h}^{-1}$).

Winter

Making use of data from the third week of June 2018, the controller behaves much like it does in autumn, as can be seen from similarities between Figures 4.10 and 4.12, and Figures 4.11 and 4.13.

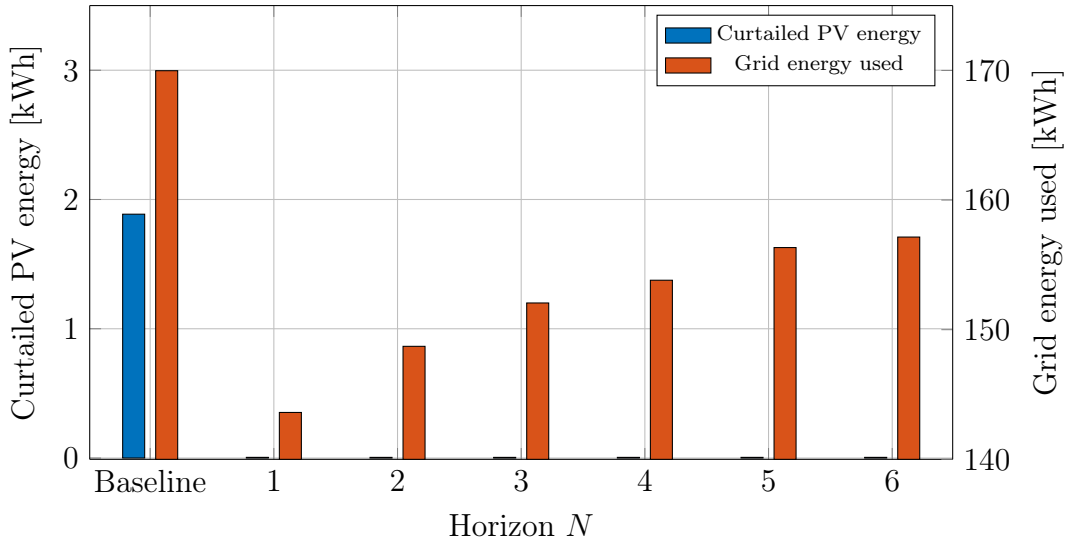

Figure 4.12: Curtailed solar and grid energy used compared across different horizons for a week in June 2018 ($\bar{f}_{\text{AHU}} = 0.36\,\text{h}^{-1}$ and $\bar{f}_{\text{EWH}} = 0.71\,\text{h}^{-1}$).

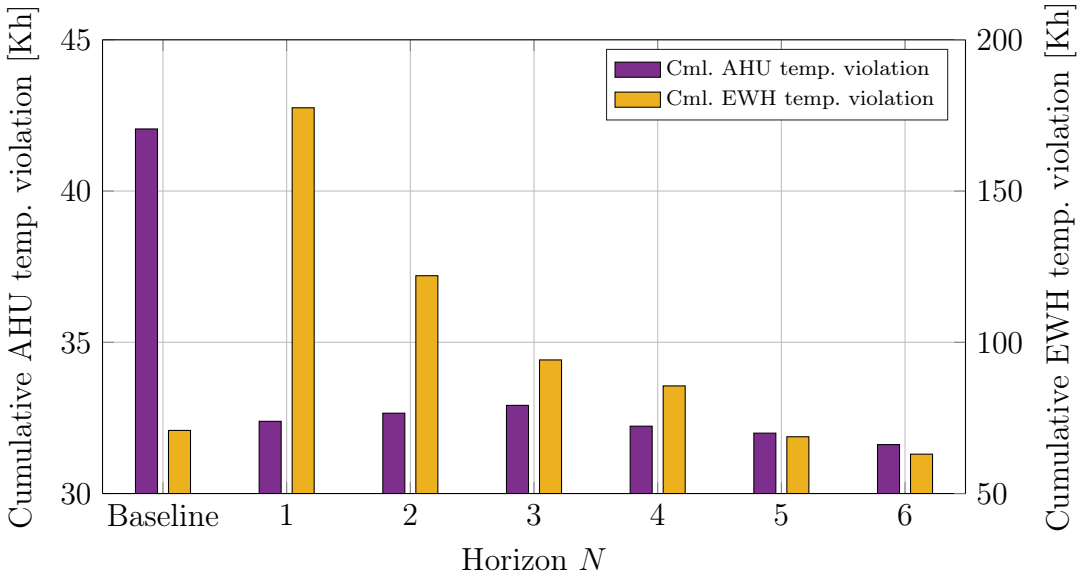

Figure 4.13: Curtailed solar and grid energy used compared across different horizons for a week in June 2018 ($\bar{f}_{\text{AHU}} = 0.36\,\text{h}^{-1}$ and $\bar{f}_{\text{EWH}} = 0.71\,\text{h}^{-1}$).

A Remark on the Increased Grid Energy Consumption in Autumn and Winter

In addition to the lower solar yield characteristic of autumn and winter, a change in prioritisation also contributes to the pronounced increase in grid dependence, when compared to spring and summer. In the interest of having comparable average commutation frequencies across seasons, the penalty for making use of grid energy is relaxed for both autumn and winter. As a result of this adjustment, higher grid dependence is observed.

4.7.2 Long-Horizon Example Simulation

An example simulation, using data from December 2017, is presented here in its entirety. The example simulation makes use of a six-step prediction horizon.

Uncontrollable Nodes

Figure 4.14 depicts the total potential solar energy the system could have generated during th 1–7 December 2017 period, as well as the amount of energy that has to be curtailed due to the BES unit being unable to absorb any more energy and both controllable loads already maximally allocated, while remaining within their defined operating bounds. For the six-step horizon, as shown, 38.62 kWh is curtailed, compared to the baseline curtailment of 50.21 kWh and 41.10 kWh for a one-step horizon.

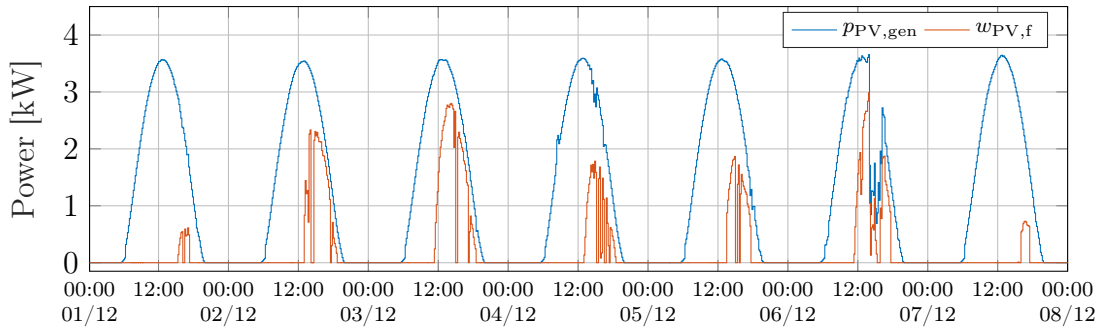

Figure 4.14: Example simulation solar PV potential generation and curtailed power.

The diverse household load, comprised of miscellaneous appliances' load power (Figure 4.15) draws a total of 35.92 kWh over the period of interest.

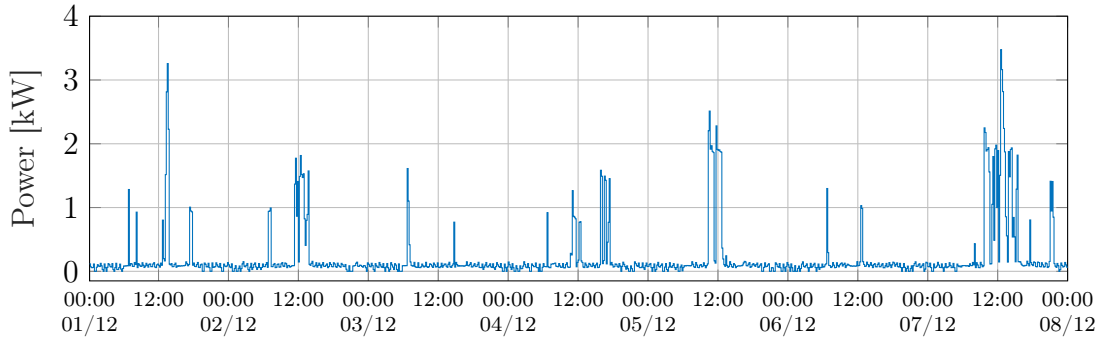

Figure 4.15: Example diverse load power.

Controllable Nodes

As is evident from Figure 4.16, the household operates largely independently during the period in question. Over the course of the week, a total of 2.13 kWh grid energy is used, entirely within the first half of the first day. A higher initial BES SoC could mitigate grid dependence further.

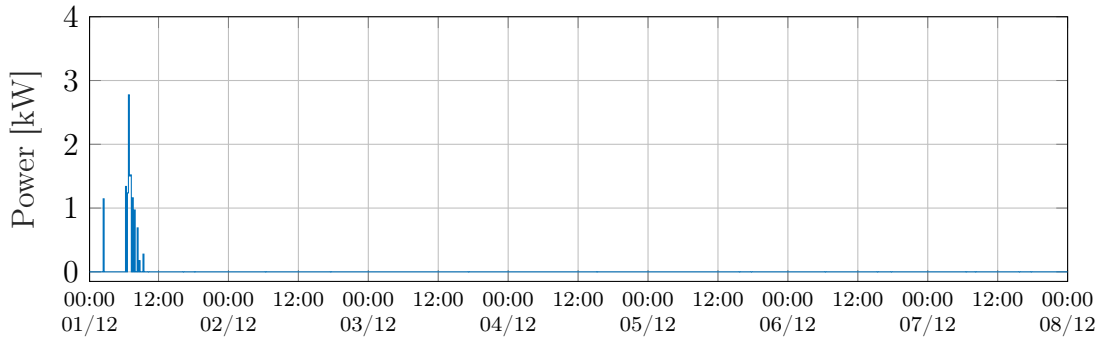

Figure 4.16: Example grid generation power.

Due to the abundance of solar energy during the simulated period, the BES unit rarely drops below 25 %, as can be seen from Figure 4.17a.

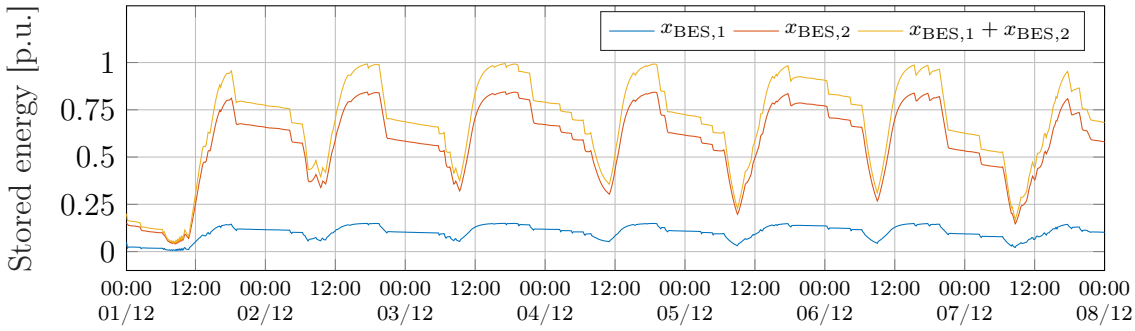

(a) Stored energy.

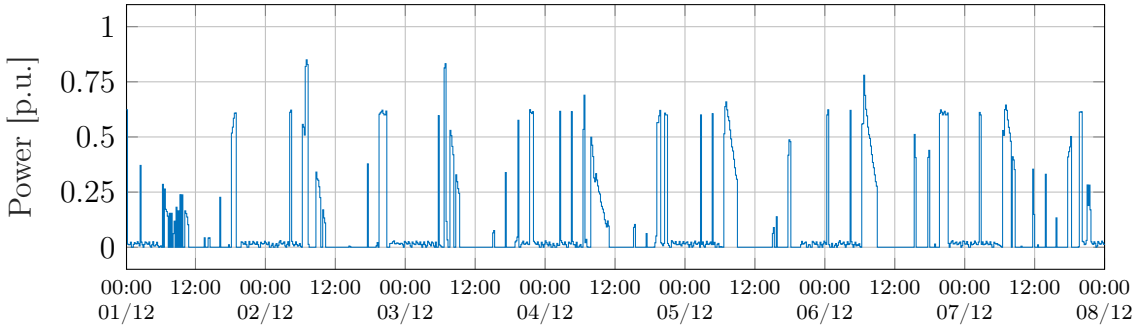

(b) Generated power.

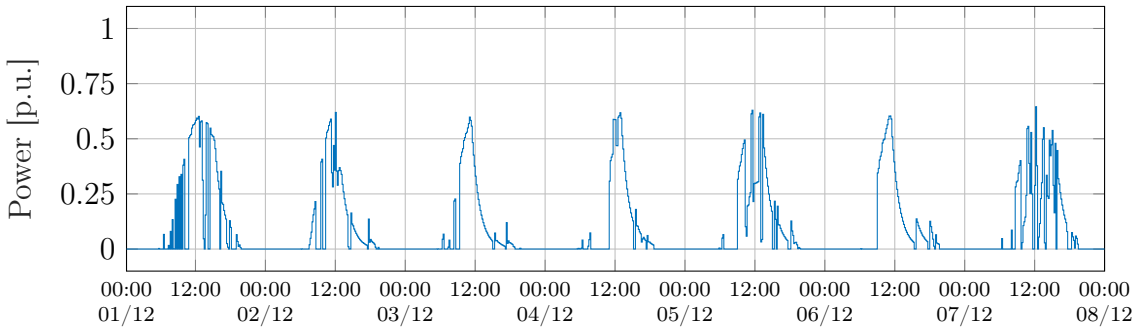

(c) Load power.

Figure 4.17: Example BES stored energy, generation power, and load power.

This is not to say that the BES unit is idle during the example week-long simulation. Quite the contrary, as is evident from Figures 4.17b and 4.17c. Furtermore, the rate-capacity effect, described in Chapter 3, can be observed most days as the battery nears a fully-charged state around midday.

The AHU remains in an on-state throughout its daily 12-hour shifts, aside from some initial commutation (Figure 4.18; a cumulative AHU temperature bound violation of 7.4563 Kh is accrued). This is due to low BES SoC coupled with a moderate penalty for use of grid power. Over the course of the example simulation period, the AHU consumes a total of 33.79 kWh.

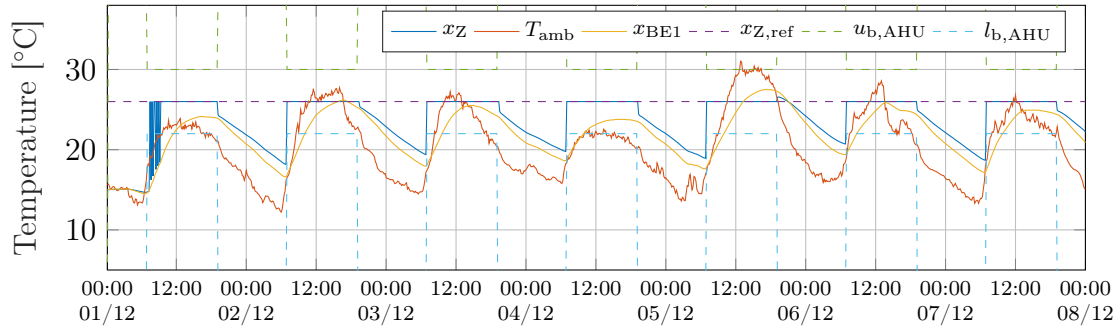

(a) State ('zone'), ambient, wall (building element nr. 1), and state reference temperature progressions. The upper and lower bounds of the AHU state temperature are also shown (active daily from 07:00 to 19:00).

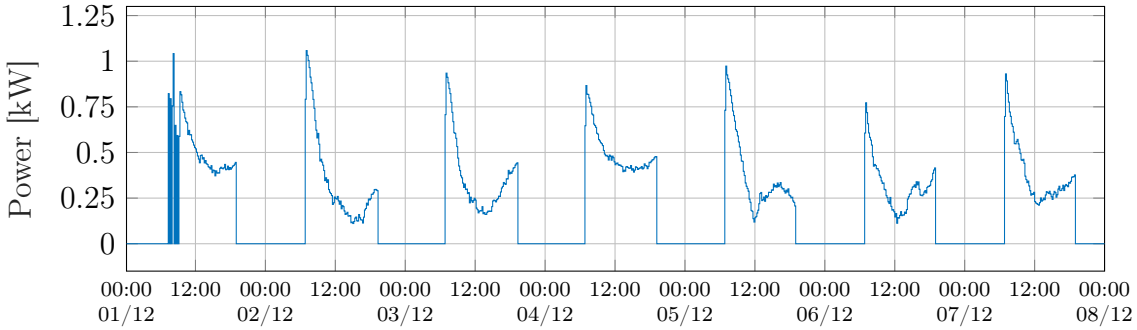

(b) Load power.

Figure 4.18: Example AHU temperatures and load power.

As can be seen from Figure 4.19a, the EWH state temperature is kept safely within the 50–70°C bounds for an overwhelming majority of the simulation period. Despite frequent use, only 25.5456 Kh are accrued in cumulative temperature bound violations. The EWH's element is switched frequently, averaging 0.60 h^{-1} and consumes a total of 93.5 kWh during the example simulation period.

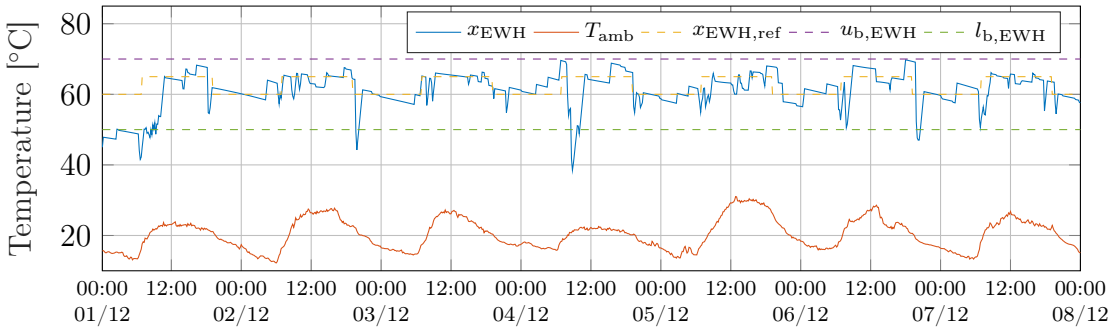

(a) EWH state, ambient, and state reference temperatures. The allowable upper and lower bounds are shown as well.

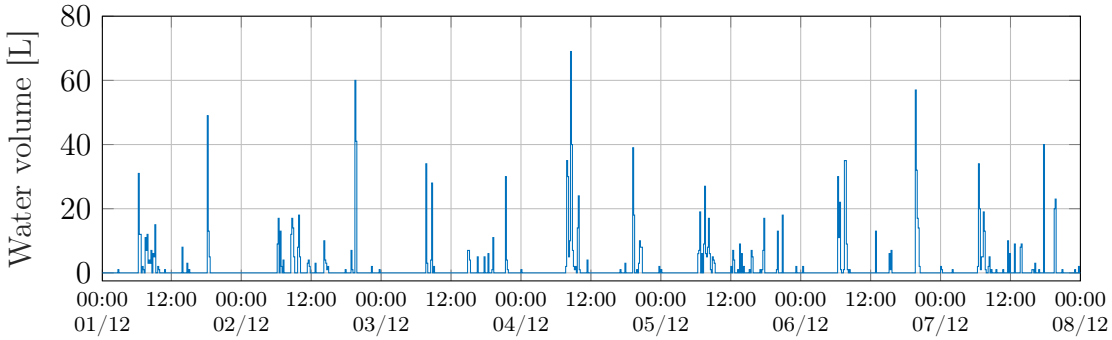

(b) Hot water usage.

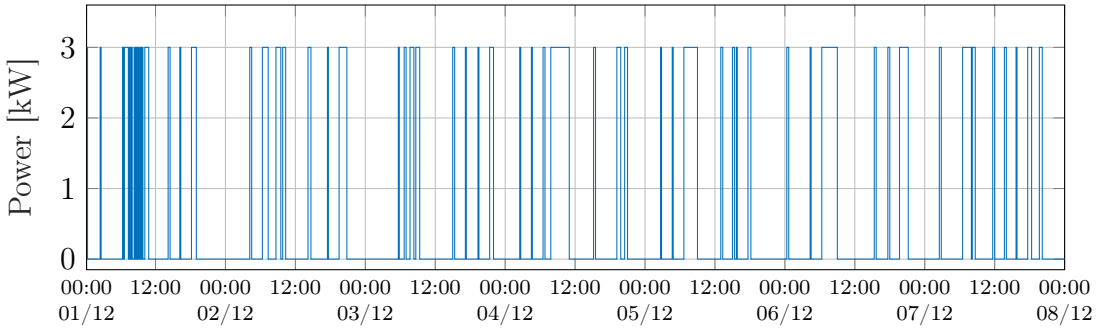

(c) Load power.

Figure 4.19: Example EWH temperatures, hot water usage, and load power.

4.7.3 The Impact of Commutation Penalties

This section investigates the impact of commutation penalties on curtailed PV energy, using data from December 2017.

Of the three controllable power nodes, two are controlled on an integer basis. Continuous fluctuation between 'on' and 'off' states is generally undesirable, as it can cause wear on the equipment involved. As described earlier, this commutation behaviour is penalised in the objective function (4.2a).

Figure 4.20 shows the influence of discouraging commutation to various degrees has on the amount of curtailed PV energy for one-, three- and five-step horizons It is some-

what intuitively assumed that a more lenient penalty on commutation might result in lower amounts of curtailed energy. Interestingly, the opposite is true for the AHU in summertime. Due to its time-varying power consumption, it is more beneficial to penalise repeated 'on/off' instructions heavily and leave it in an on-state than to do the opposite.

This can be explained by the comparatively small amount of power required to maintain close adherence to a reference temperature, as opposed to a higher power demand required to regulate air temperature toward a reference if the difference between ambient and reference temperatures is sizeable. As could be expected, relaxing the penalty on EWH commutation results in lower amounts of curtailed PV energy.

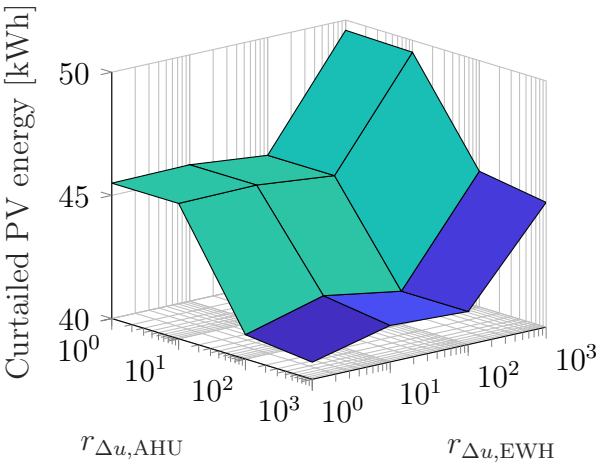

(a) $N = 1$.

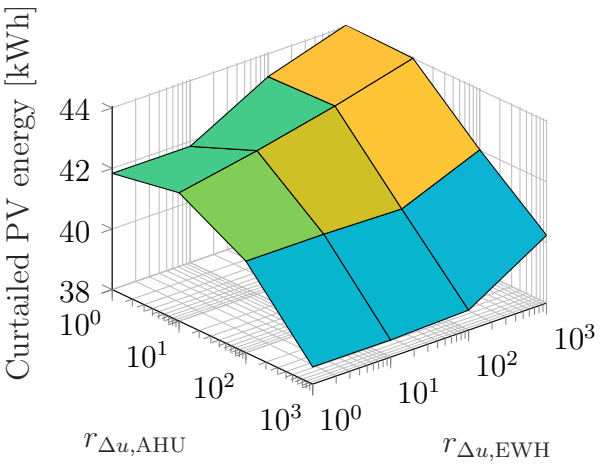

(b) $N = 3$.

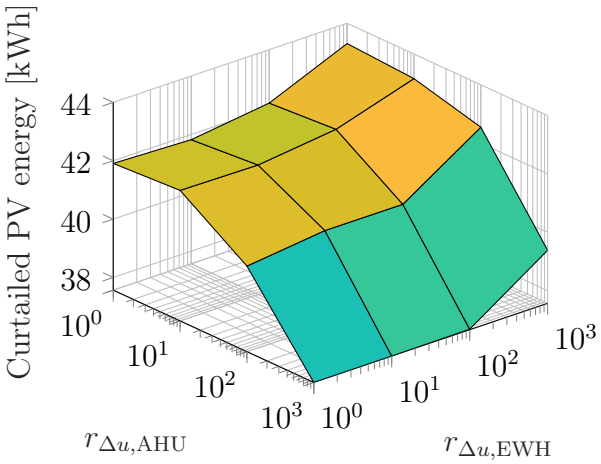

(c) $N = 5$.

Figure 4.20: The impact of integer commutation penalties on curtailed solar energy for different prediction horizon lengths.

The more pronounced variation in Figure 4.20a, as opposed to Figure 4.20b and even more so to Figure 4.20c, can be attributed to the larger influence single terms have in short horizon objective functions. As the horizon increases, a single term's relative influence wanes as more terms are added to $J(k)$.

4.7.4 Computational-Load Reduction Through Initial-Bound Guess

Here the search procedure with the initial-bound guess function (described in Algorithm 4) included as precursor to the branch-and-bound (with depth-first search) function is measured against the branch-and-bound function without the guess function as precursor. Additionally, it is compared with brute-force calculation of the cost at every leaf node of the decision tree and selecting the lowest-cost option, known as doing an exhaustive search of the tree.

Table 4.1 lists the average amount of decision-tree nodes visited before the optimal control-input sequence is found, both with and without the initial-bound guess function. The alternative of doing an exhaustive search of the tree is provided for reference.

Table 4.1: Performance comparison of search methods

Horizon length (N)	1	2	3	4	5	6
Exhaustive search	4	20	84	340	1364	5460
Branch and bound (no initial guess)	4	15	38	76	151	301
Branch and bound (with initial guess)	4	12	32	65	133	270

Consider Figure 4.3a, for example, which depicts the decision tree for a three-step prediction horizon. Nodes lower down the tree branches are dependent on nodes above them, because the control- and disturbance-input matrices are functions of $\boldsymbol{x}$, as described by (3.35). This implies that an exhaustive search cannot evaluate a leaf node without having first calculated the sequence of predicted states leading up to the leaf node in question. This makes the exhaustive search approach unappealing in the present case, as is clear from the explosion in the amount of computation required as horizon length increases (Table 4.1).

It is clear that the branch-and-bound approach is much more effective, compared to the exhaustive search, when longer horizon lengths are used ($N > 1$). When the initial-bound guess is included as well (i.e. starting the decision-tree traversal with incumbent $J^*(k) \ll \infty$), further computational reductions, consistently in excess of 10 %, are brought about.

4.8 Summary

Chapter 4 describes a predictive control strategy aimed at reducing the curtailment of solar PV energy. An objective function is formulated and reworked into the computationally convenient quadratic form. A means of maximally allocating excess solar power generation to available loads is developed in the form of a control-input reference generator. The control strategy is translated into an algorithm from where it is evaluated in numerous simulations, primarily depicting reduced solar PV curtailment, in addition to adhering to thermal constraints as far as possible.

Chapter 5

Conclusions and Recommendations

This chapter concludes the thesis. The main contributions are briefly revisited, where after recommendations for future work are made.

5.1 Overview of Main Results

This section reviews the main results of the thesis, namely the description of a unified system, within which diverse electrical entities are coordinated in unison, and the implementation of a predictive controller in order to reduce curtailed PV and bolster self-sufficiency, while adhering to specified constraints.

5.1.1 System Description

Heterogeneous models, each representing different physical systems, are presented as part a single state-space representation, which is itself embedded within a framework that views electrical entities as power nodes. This node-based approach serves to organise the various electrical entities within a given household in preparation for the exertion of control over them.

5.1.2 Predictive Controller Implementation

With the system described within the power nodes framework in mind, as well as the controllable plant consisting of numerous manipulable electrical entities, a predictive control scheme is formulated to reduce solar PV curtailment in order to boost self-sufficiency.

An objective function is defined and a number of constraints included. A means of reducing PV curtailment through maximally allocating control inputs is proposed. An algorithmic calculation of the optimal control input sequence is developed, complete with a means of shortening the calculation by recycling old sequences.

The predictive controller is evaluated across a diverse set of conditions, from single-step up to six-step horizons. The operation of the controller is best showcased in summer

conditions with a six-step horizon. Clear reductions in solar PV energy curtailment are demonstrated, both when compared to a rules-based controller and to the same predictive control scheme at shorter horizons. Additionally, thermal comfort bounds are largely adhered to in the pursuit of higher levels of self sufficiency.

5.2 Recommendations for Future Work

Some suggestions for follow-on research are made below.

5.2.1 Continuous-Valued Control

The commutation penalty investigation in Section 4.7.3 suggests that continuous-valued control over the AHU and EWH can yield material additional benefits. The added complexity in generating time-varying reference air temperatures, in the case of the AHU, and the inclusion of an ac-to-ac drive, in the case of the EWH, could be justified by potential additional productivity gain. Continuous-valued control, as opposed to integer control, also has the added benefit of exact solutions. In such instances, a decision tree is not necessary, and, as a direct result, longer prediction horizons become feasible.

5.2.2 Battery Degradation in Objective Function

In [20] a convex, piecewise-affine battery capacity degradation map is developed. The aim of this map is to connect individual control actions to the lifetime of the BES. In the present instance, the battery, to a large extent, serves as a buffer against the variable PV power supply. By including the adverse consequences of such intensive use, more conservative control actions might be decided upon, depending on the priority battery lifetime is given in the objective function, but the cost to the home owner could be lowered due to less frequently replacing the BES unit.

5.2.3 Introduce Uncertainty to Improve Robustness

At present, for the entirety of the prediction horizon, perfect knowledge is assumed. This deterministic approach has proven invaluable in developing the basic system structure, but further testing would benefit greatly from the introduction of uncertainty in the form of error in measurements and forecasts to improve the resiliency of the controller.

Bibliography

[1] A. Zipperer, P. A. Aloise-Young, S. Suryanarayanan, et al. "Electric Energy Management in the Smart Home: Perspectives on enabling technologies and consumer behavior". In: *Proceedings of the IEEE* 101.11 (2013).

[2] B. Asare-Bediako, P. F. Ribeiro, and W. L. Kling. "Integrated Energy Optimization with Smart Home Energy Management Systems". In: *3rd IEEE PES Innovative Smart Grid Technologies Europe (ISGT Europe)*. 2012.

[3] City of Cape Town. *Smart Living Handbook: Energy in Your Home*. 4th ed. Self-published, 2011, p. 64.

[4] J. Han, C. S. Choi, W. K. Park, et al. "Green Home Energy Management System Through Comparison of Energy Usage Between the Same Kinds of Home Appliances". In: *2011 IEEE* 15^{th} *International Symposium on Consumer Electronics*. 2011.

[5] S. Coetzee, T. Mouton, and M. J. Booysen. "Home Energy Management Systems: A Qualitative Analysis and Overview". In: *IEEE Africon 2017 Proceedings*. 2017.

[6] City of Cape Town Electricity Services. *Residential Electricity Tariff Explanation. Tariffs Valid With Effect from 1 July 2018*. Self-published. 2018. URL: https://resource.capetown.gov.za/documentcentre/Documents/Procedures,%20guidelines%20and%20regulations/Residential-electricity-tariff-explanation.pdf.

[7] *Insight. An overview of electricity consumption and pricing in South Africa*. Desktop. Deloitte, 2017. URL: www.eskom.co.za/Documents/EcoOverviewElectricitySA-2017.pdf.

[8] M. Modisane Motiang and R. Nembahe. *Energy Price Report 2017*. Department of Energy, 2017. URL: http://www.energy.gov.za/files/media/explained/Energy-Price-Report-2017.pdf.

[9] A. Ilas, P. Ralon, A. Rodriguez, et al. *Renewable Power Generation Costs in 2017*. International Renewable Energy Agency, 2018. ISBN: 978-92-9260-040-2.

[10] Claire Curry. *Lithium-ion Battery Costs and Market. Squeezed margins seek technology improvements & new business models*. 2017.

[11] H. Merz, T. Hansemann, and C. Hübner. *Building Automation. Communication Systems with EIB/KNX, LON and BACnet*. 2nd ed. Cham, Switzerland: Springer International Publishing AG, 2018. Chap. 1. ISBN: 978-3-319-73222-0. DOI: https://doi.org/10.1007/978-3-319-73223-7.

[12] J. T. Amann, A. Wilson, and K. Ackerly. *Consumer Guide to Home Energy Savings*. 9th ed. Gabriola Island, Canada: New Society Publishers, 2007. Chap. 1, p. 9. ISBN: 978-0-86571-602-5.

[13] F. Borelli, A. Bemporad, and M. Morari. *Predictive Control for Linear and Hybrid Systems*. 1st ed. Cambridge, UK: Cambridge University Press, 2017. Chap. 17. ISBN: 978-1-107-65287-3.

[14] K. Wong and M. Negnevitsky. "Demand-side management evaluation tool". In: *IEEE Transactions on Power Systems* 30.1 (2015), pp. 212–222. ISSN: 08858950. DOI: 10.1109/TPWRS.2014.2329323.

[15] P. J. C. Nel, M. J. Booysen, and B. Van Der Merwe. "A Computationally Inexpensive Energy Model for Horizontal Electric Water Heaters With Scheduling". In: *IEEE Transactions on Smart Grid* 9.1 (2018), pp. 48–56. DOI: 10.1109/TSG.2016.2544882.

[16] D. Gyalistras, ed. *OptiControl. Use of weather and occupancy forecasts for optimal building climate control*. 2013 (accessed on 11 November 2018). URL: https://opticontrol.ee.ethz.ch/08E-Contact.html.

[17] F. Oldewurtel. "Stochastic Model Predictive Control for Energy Efficient Building Climate Control". PhD thesis. ETH Zurich, 2011. URL: https://www.research-collection.ethz.ch/handle/20.500.11850/153334.

[18] D. Sturzenegger. "Model Predictive Building Climate Control: Steps Towards Practice". PhD thesis. ETH Zurich, 2014. ISBN: 8610828378018. URL: https://www.research-collection.ethz.ch/handle/20.500.11850/98291.

[19] T. F. Fuller, M. Doyle, and J. Newman. "Simulation and Optimization of the Dual Lithium Ion Insertion Cell". In: *Journal of the Electrochemical Society* 140.1 (1994).

[20] P. Fortenbacher. "On the Integration of Distributed Battery Storage in Low Voltage Grids". 2017. ISBN: 9783906327785.

[21] G. F. Franklin, J. D. Powell, and M. L. Workman. *Digital Control of Dynamic Systems*. 3rd ed. Addison-Wesley, 1998. Chap. 4. ISBN: 978-0201820546.

[22] S. J. Qin and T. A. Badgwell. "A survey of industrial model predictive control technology". In: *Control Engineering Practice* 11.7 (2003), pp. 733–764.

[23] T. Geyer. *Model Predictive Control of High Power Converters and Industrial Drives*. United Kingdom: John Wiley & Sons, 2016. ISBN: 978-1-119-01090-6.

[24] J. Nocedal and S. Wright. *Numerical Optimization*. 2nd ed. New York, USA: Springer-Verlag, 2006. ISBN: 978-0-387-30303-1. DOI: 10.1007/978-0-387-40065-5.

[25] K. Heussen, S. Koch, A. Ulbig, et al. "Unified System-Level Modeling of Intermittent Renewable Energy Sources and Energy Storage for Power System Operation". In: *IEEE Systems Journal* 6.1 (2012), pp. 140–151. ISSN: 19328184. DOI: 10.1109/JSYST.2011.2163020.

[26] *Solar resource maps of South Africa*. 2017 (accessed on 11 November 2018). URL: https://solargis.com/maps-and-gis-data/download/south-africa.

[27] G. M. Masters. *Renewable and Efficient Electric Power Systems*. 2nd ed. Hoboken, New Jersey: John Wiley & Sons, Inc., 2013. ISBN: 978-1-118-14062-8.

[28] *CS6K-285|290MS-SD*. 2018 (accessed on 30 August 2018). URL: https://www.canadiansolar.com/downloads/datasheets/na/Canadian_Solar-Datasheet-CS6KMS_SmartDC-v5.4na.pdf.

[29] *Operating Manual: SUNNY BOY 3000TL / 3600TL / 4000TL / 5000TL*. 2018 (accessed on 30 August 2018). URL: https://files.sma.de/dl/15330/SB30-50TL-21-BE-en-11.pdf.

[30] *Stellenbosch Weather. Location: 33 ° 55'42.84" S, 18 ° 51'55.08" E, Elevation: 119m*. 2018 (accessed on 11 November 2018). URL: http://weather.sun.ac.za/.

[31] *Global Horizontal Irradiance (GHI)*. 2018 (accessed on 11 November 2018). URL: https://www.homerenergy.com/products/pro/docs/3.11/global_horizontal_irradiance_ghi.html.

[32] M. J. Brooks, S. du Clou, J. L. van Niekerk, et al. "SAURAN: A new resource for solar radiometric data in Southern Africa". In: *Journal of Energy in Southern Africa* 26.1 (2015).

[33] *Powerwall 2 AC*. 2018 (accessed on 15 October 2018). URL: https://www.tesla.com/sites/default/files/pdfs/powerwall/Powerwall%202_AC_Datasheet_en_northamerica.pdf.

[34] *New Arctic Midwall Inverter Range*. 2018 (accessed on 28 August 2018). URL: https://www.allianceair.co.za/download-catalogue/alliance-arctic-inverter.pdf.

[35] M. Roux and M. J. Booysen. "Use of smart grid technology to compare regions and days of the week in household water heating". In: Domestic Use of Energy. 2017.

[36] *Gurobi Optimization. Gurobi Optimizer 8.0*. 2018 (accessed on 30 August 2018). URL: http://www.gurobi.com/.

[37] C. A. Floudas. *Nonlinear and Mixed-Integer Optimization: Fundamentals and Applications*. 1st ed. New York, USA: Oxford University Press USA, 1995. Chap. 5. ISBN: 978-0195100563.

[38] B. A. Cunha, A. Burillo, and E. Bouza. "Legionnaires' disease". In: *The Lancet* 387 (10016 2016). DOI: https://doi.org/10.1016/S0140-6736(15)60078-2.

[39] B. Lévesque, M. Lavoire, and J. Joly. "Residential water heater temperature: 49 or 60 degrees Celsius?" In: *The Canadian Journal of Infectious Diseases* 15.1 (2004), pp. 11–12.

[40] M. R. Freije and J. M. Barbaree. *Legionellae Control in Health Care Facilities: A Guide for Minimizing Risk*. HC Information Resources, Inc., 1996. ISBN: 978-0964992641.

Appendix A

Stellenbosch Municipality Tariffs

Note: 1 unit = 1 kWh. All monetary values exclude value-added tax.

Table A.1: Domestic tariffs[1]

Tariff bracket (units)	Cost (c/kWh)
Life Line[2]	
0–60	0
61–110	91.57
110–360	114.59
360–660	171.58
660–1000	197.59
Regular prepaid[3]	
0–50	91.73
51–300	143.25
301–600	174.58
$>$ 600	195.53
Regular prepaid[4]& regular[5]	
0–50	91.57
51–300	117.45
301–600	165.70
$>$ 600	195.14

[1]These tariffs also apply to regular and prepaid domestic properties equipped with renewable-energy generation for own use.

[2]Applicable to indigent households, defined as those properties valued at R200 000 or less, while occupying an area of 250 m^3 or less.

[3]Applicable to residences with an average monthly consumption of less than 600 kWh in the previous financial year.

[4]Applicable to residences with an average monthly consumption of, or more than, 600 kWh in the previous financial year. A monthly fixed charge of R123.22 also applies.

[5]A monthly fixed charge of R154.89 also applies.

Table A.2: Domestic tariffs for properties with renewable-energy generation for own use and export[1]

Tariff bracket (units)	Price (c/kWh)
Import	
0–50	91.57
51–300	117.45
301–600	165.70
> 600	195.14
Export	
Low season[2]	
Peak	85.18
Standard	58.61
Off peak	38.15
High season[3]	
Peak	261.08
Standard	79.10
Off peak	42.96

Table A.3: Time-of-use period definitions

Period	Time of day
Low season	
Monday–Friday	
Off peak	22:00–06:00
Standard	06:00–07:00; 10:00–18:00; 20:00–22:00
Peak	07:00–10:00; 18:00–20:00
Saturday	
Off peak	20:00–07:00; 12:00–18:00
Standard	07:00–12:00; 18:00–20:00
Sunday	
Off peak	All day
High season	
Monday–Friday	
Off peak	22:00–06:00
Standard	10:00–17:00; 19:00–22:00
Peak	06:00–9:00; 17:00–19:00
Saturday	
Off peak	20:00–07:00; ; 12:00–18:00
Standard	07:00–12:00; 18:00–20:00
Sunday	
Off peak	All day

[1] A reading cost of R75.60 and basic charge of R154.89, both monthly, also apply.
[2] September to May of the following year.
[3] June through August.

Appendix B

Room and Air-Handling Unit Specifications

A number of aspects define the room and are briefly described below:

B.1 Room Specifications

Table B.1: Zone attributes

Zone		
Attribute	Value	Unit
Floor area	16	[m^2]
Wall height	3	[m]
Volume	48	[m^3]

Table B.2: Building elements 1–4 attributes

Building element		
Attribute	Value	Unit
Construction type	Wooden wall	[-]
Adjacent A	Zone	[-]
Adjacent B	Ambient air	[-]
Area	4×3	[m^2]

Table B.3: Wooden wall construction attributes

Construction		
Attribute	Value	Unit
Material(s) used	Birch wood	[-]
Thickness	0.05	[m]
Convection coefficient (Adjacent A)	7	[W/m^{2}K]
Convection coefficient (Adjacent B)	7	[W/m^{2}K]

Table B.4: Building element 5 attributes

Building element		
Attribute	Value	Unit
Construction type	Wooden floor	[-]
Adjacent A	Zone	[-]
Adjacent B	Void	[-]
Area	4×4	[m^2]

Table B.5: Wooden floor construction attributes

Construction		
Attribute	Value	Unit
Material(s) used	Birch wood	[-]
Thickness	0.05	[m]
Convection coefficient (Adjacent A)	5	[W/m^{2}K]
Convection coefficient (Adjacent B)	0	[W/m^{2}K]

Table B.6: Building element 6 attributes

Building element		
Attribute	Value	Unit
Construction type	Wooden ceiling	[-]
Adjacent A	Zone	[-]
Adjacent B	Void	[-]
Area	4×4	[m^2]

Table B.7: Wooden ceiling construction attributes

Construction		
Attribute	Value	Unit
Material(s) used	Birch wood	[-]
Thickness	0.05	[m]
Convection coefficient (Adjacent A)	5	[W/m^{2}K]
Convection coefficient (Adjacent B)	0	[W/m^{2}K]

Table B.8: Birch wood material attributes

Material		
Attribute	Value	Unit
Specific heat capacity	1600	[J/kg K]
Specific thermal resistance	7.143	[m K/W]
Density	670	[kg/m^3]

B.2 Air-Handling Unit Specifications

The dual split-inverter AHU used is an Alliance Arctic Midwall FOUSI12 (12 000 Btu) [34], the specifications of which are given in Table B.9[1].

Table B.9: Selected Alliance Arctic Midwall FOUSI12 (12 000 Btu) specifications

Cycle	Specification	Value	Unit
Heating	Capacity	3410	[W]
	Input	997	[W]
	COP	3.42	[W/W]
Cooling	Capacity	3355	[W]
	Input power	1104	[W]
	EER	3.04	[W/W]
Both	Air flow rate (maximum)	560 (0.190)	[m^3/h] ([kg/s])
	Air flow rate (minimum)	440 (0.149)	[m^3/h] ([kg/s])

[1]The volumetric flow rate has been converted into its representative mass flow rate at a density of 1.225 kg/m^3, assuming air pressure of 101.325 kPa.

Appendix C

Alternative Cost Representations

Alternative representations to the cost in sum form can be used to group variables so as to be manipulated in a control environment more easily. Two such representations are given here: the vector and quadratic programming forms.

C.1 Vector Form

Sum form of the cost function:

$$J(k) = \sum_{l=k}^{k+N-1} \left(\|\boldsymbol{x}_{l+1} - \boldsymbol{x}_{l+1,\text{ref}}\|^2_{\boldsymbol{Q}} + \|\boldsymbol{u}_l - \boldsymbol{u}_{l,\text{ref}}\|^2_{\boldsymbol{R}} + \|\Delta\boldsymbol{u}_l\|^2_{\boldsymbol{R}_{\Delta u}} \right). \tag{C.1}$$

$$\boldsymbol{X}(k) = \boldsymbol{S}_x\boldsymbol{x}(k) + \boldsymbol{S}_u(k)\boldsymbol{U}(k) + \boldsymbol{S}_v(k)\boldsymbol{V}(k), \tag{C.2a}$$

with

$$\boldsymbol{X}(k) = \begin{bmatrix} \boldsymbol{x}_{k+1} \\ \boldsymbol{x}_{k+2} \\ \vdots \\ \boldsymbol{x}_{k+N} \end{bmatrix}, \ \boldsymbol{U}(k) = \begin{bmatrix} \boldsymbol{u}_k \\ \boldsymbol{u}_{k+1} \\ \vdots \\ \boldsymbol{u}_{k+N-1} \end{bmatrix} \text{ and } \boldsymbol{V}(k) = \begin{bmatrix} \boldsymbol{v}(k) \\ \boldsymbol{v}_{k+1} \\ \vdots \\ \boldsymbol{v}_{k+N-1} \end{bmatrix}.$$

Furthermore, $\boldsymbol{S}_x \in \mathbb{R}^{N\cdot n_x \times n_x}$ is defined as

$$\boldsymbol{S}_x = \begin{bmatrix} \boldsymbol{A} \\ \boldsymbol{A}^2 \\ \vdots \\ \boldsymbol{A}^{\text{N}} \end{bmatrix}, \tag{C.2b}$$

$\boldsymbol{S}_u \in \mathbb{R}^{N\cdot n_x \times N\cdot m}$ is defined as

$$\boldsymbol{S}_u(k) = \begin{bmatrix} \boldsymbol{B}_u(k) & \boldsymbol{0} & \boldsymbol{0} & \cdots & \boldsymbol{0} \\ \boldsymbol{A}\boldsymbol{B}_u(k) & \boldsymbol{B}_{u,k+1} & \boldsymbol{0} & \cdots & \boldsymbol{0} \\ \boldsymbol{A}^2\boldsymbol{B}_u(k) & \boldsymbol{A}\boldsymbol{B}_{u,k+1} & \boldsymbol{B}_{u,k+2} & \cdots & \boldsymbol{0} \\ \vdots & \vdots & \vdots & \ddots & \vdots \\ \boldsymbol{A}^{N-1}\boldsymbol{B}_u(k) & \boldsymbol{A}^{N-2}\boldsymbol{B}_{u,k+1} & \boldsymbol{A}^{N-3}\boldsymbol{B}_{u,k+2} & \cdots & \boldsymbol{B}_{u,k+N-1} \end{bmatrix} \tag{C.2c}$$

and, similarly, $\boldsymbol{S}_v \in \mathbb{R}^{N\cdot n_x \times N\cdot n_v}$ is defined as

$$\boldsymbol{S}_v(k) = \begin{bmatrix} \boldsymbol{B}_v(k) & \boldsymbol{0} & \boldsymbol{0} & \cdots & \boldsymbol{0} \\ \boldsymbol{A}\boldsymbol{B}_v(k) & \boldsymbol{B}_{v,k+1} & \boldsymbol{0} & \cdots & \boldsymbol{0} \\ \boldsymbol{A}^2\boldsymbol{B}_v(k) & \boldsymbol{A}\boldsymbol{B}_{v,k+1} & \boldsymbol{B}_{v,k+2} & \cdots & \boldsymbol{0} \\ \vdots & \vdots & \vdots & \ddots & \vdots \\ \boldsymbol{A}^{N-1}\boldsymbol{B}_v(k) & \boldsymbol{A}^{N-2}\boldsymbol{B}_{v,k+1} & \boldsymbol{A}^{N-3}\boldsymbol{B}_{v,k+2} & \cdots & \boldsymbol{B}_{v,k+N-1} \end{bmatrix}. \tag{C.2d}$$

The cost function can also be written in vector form, as follows:

$$\begin{aligned} J_k = \|\boldsymbol{X}(k) - \boldsymbol{X}_{\text{ref}}(k)\|^2_{\tilde{\boldsymbol{Q}}} + \|\boldsymbol{U}(k) - \boldsymbol{U}_{\text{ref}}(k)\|^2_{\tilde{\boldsymbol{R}}} \\ + \left\|\tilde{\mathbf{I}}_{\Delta u}\boldsymbol{U}(k) - \tilde{\mathbf{I}}_{\Delta u,\text{init}}\boldsymbol{u}(k-1)\right\|^2_{\tilde{\boldsymbol{R}}_{\Delta u}}, \end{aligned} \tag{C.3a}$$

where the stacked penalty matrices are defined as

$$\tilde{\boldsymbol{Q}} = \begin{bmatrix} \boldsymbol{Q} & \boldsymbol{0} & \cdots & \boldsymbol{0} \\ \boldsymbol{0} & \boldsymbol{Q} & \cdots & \boldsymbol{0} \\ \vdots & \vdots & \ddots & \vdots \\ \boldsymbol{0} & \boldsymbol{0} & \cdots & \boldsymbol{Q} \end{bmatrix}, \tag{C.3b}$$

$$\tilde{\boldsymbol{R}} = \begin{bmatrix} \boldsymbol{R} & \boldsymbol{0} & \cdots & \boldsymbol{0} \\ \boldsymbol{0} & \boldsymbol{R} & \cdots & \boldsymbol{0} \\ \vdots & \vdots & \ddots & \vdots \\ \boldsymbol{0} & \boldsymbol{0} & \cdots & \boldsymbol{R} \end{bmatrix} \tag{C.3c}$$

and

$$\tilde{\boldsymbol{R}}_{\Delta u} = \begin{bmatrix} \boldsymbol{R}_{\Delta u} & \boldsymbol{0} & \cdots & \boldsymbol{0} \\ \boldsymbol{0} & \boldsymbol{R}_{\Delta u} & \cdots & \boldsymbol{0} \\ \vdots & \vdots & \ddots & \vdots \\ \boldsymbol{0} & \boldsymbol{0} & \cdots & \boldsymbol{R}_{\Delta u} \end{bmatrix}. \tag{C.3d}$$

Furthermore, the matrices used to order consecutive time steps' control input vectors

(in order to penalise change in control inputs) are defined as

$$\tilde{\mathbf{I}}_{\Delta u} = \begin{bmatrix} \mathbf{I}^m & \mathbf{0} & \mathbf{0} & \cdots & \mathbf{0} \\ -\mathbf{I}^m & \mathbf{I}^m & \mathbf{0} & \cdots & \mathbf{0} \\ \mathbf{0} & -\mathbf{I}^m & \mathbf{I}^m & \cdots & \mathbf{0} \\ \vdots & \vdots & \vdots & \ddots & \vdots \\ \mathbf{0} & \mathbf{0} & \mathbf{0} & \cdots & \mathbf{I}^m \end{bmatrix} \tag{C.3e}$$

and

$$\tilde{\mathbf{I}}_{\Delta u,\text{init}} = \begin{bmatrix} \mathbf{I}^m \\ \mathbf{0} \\ \vdots \\ \mathbf{0} \end{bmatrix}. \tag{C.3f}$$

The state reference vector can be defined as

$$\boldsymbol{X}_{\text{ref}}(k) = \begin{bmatrix} \boldsymbol{x}_{\text{ref}}(k+1) \\ \boldsymbol{x}_{\text{ref}}(k+2) \\ \vdots \\ \boldsymbol{x}_{\text{ref}}(k+N) \end{bmatrix} \in \mathbb{R}^{N \cdot n_x}. \tag{C.4}$$

The input reference vector is defined as

$$\boldsymbol{U}_{\text{ref}}(k) = \begin{bmatrix} \boldsymbol{u}_{\text{ref}}(k) \\ \boldsymbol{u}_{\text{ref},k+1} \\ \vdots \\ \boldsymbol{u}_{\text{ref},k+N-1} \end{bmatrix} \in \mathbb{R}^{N(m_{\text{c}}+m_{\text{b}})}. \tag{C.5}$$

C.2 Quadratic Programming Form

The first term of (C.3a) can be expanded as shown below:

$$\begin{aligned}
\|\boldsymbol{X}(k)-\boldsymbol{X}_{\text{ref}}(k)\|_{\tilde{\boldsymbol{Q}}}^2 =& \|\boldsymbol{S}_x\boldsymbol{x}(k)+\boldsymbol{S}_u(k)\boldsymbol{U}(k)+\boldsymbol{S}_v(k)\boldsymbol{V}(k)-\boldsymbol{X}_{\text{ref}}(k)\|_{\tilde{\boldsymbol{Q}}}^2 \\
=&\big(\boldsymbol{S}_x\boldsymbol{x}(k)+\boldsymbol{S}_u(k)\boldsymbol{U}(k)+\boldsymbol{S}_v(k)\boldsymbol{V}(k)-\boldsymbol{X}_{\text{ref}}(k)\big)^{\mathrm{T}}\tilde{\boldsymbol{Q}} \\
&\big(\boldsymbol{S}_x\boldsymbol{x}(k)+\boldsymbol{S}_u(k)\boldsymbol{U}(k)+\boldsymbol{S}_v(k)\boldsymbol{V}(k)-\boldsymbol{X}_{\text{ref}}(k)\big) \\
=&\big(\boldsymbol{x}^{\mathrm{T}}(k)\boldsymbol{S}_x^{\mathrm{T}}\tilde{\boldsymbol{Q}}+\boldsymbol{U}^{\mathrm{T}}(k)\boldsymbol{S}_u^{\mathrm{T}}(k)\tilde{\boldsymbol{Q}}+\boldsymbol{V}^{\mathrm{T}}(k)\boldsymbol{S}_v^{\mathrm{T}}(k)\tilde{\boldsymbol{Q}}-\boldsymbol{X}_{\text{ref}}^{\mathrm{T}}(k)\tilde{\boldsymbol{Q}}\big) \\
&\big(\boldsymbol{S}_x\boldsymbol{x}(k)+\boldsymbol{S}_u(k)\boldsymbol{U}(k)+\boldsymbol{S}_v(k)\boldsymbol{V}(k)-\boldsymbol{X}_{\text{ref}}(k)\big) \\
=&\boldsymbol{x}^{\mathrm{T}}(k)\boldsymbol{S}_x^{\mathrm{T}}\tilde{\boldsymbol{Q}}\boldsymbol{S}_x\boldsymbol{x}(k)+\boldsymbol{x}^{\mathrm{T}}(k)\boldsymbol{S}_x^{\mathrm{T}}\tilde{\boldsymbol{Q}}\boldsymbol{S}_u(k)\boldsymbol{U}(k) \\
&+\boldsymbol{x}^{\mathrm{T}}(k)\boldsymbol{S}_x^{\mathrm{T}}\tilde{\boldsymbol{Q}}\boldsymbol{S}_v(k)\boldsymbol{V}(k)-\boldsymbol{x}^{\mathrm{T}}(k)\boldsymbol{S}_x^{\mathrm{T}}\tilde{\boldsymbol{Q}}\boldsymbol{X}_{\text{ref}}(k) \\
&+\boldsymbol{U}^{\mathrm{T}}(k)\boldsymbol{S}_u^{\mathrm{T}}(k)\tilde{\boldsymbol{Q}}\boldsymbol{S}_x\boldsymbol{x}(k)+\boldsymbol{U}^{\mathrm{T}}(k)\boldsymbol{S}_u^{\mathrm{T}}(k)\tilde{\boldsymbol{Q}}\boldsymbol{S}_u(k)\boldsymbol{U}(k) \\
&+\boldsymbol{U}^{\mathrm{T}}(k)\boldsymbol{S}_u^{\mathrm{T}}(k)\tilde{\boldsymbol{Q}}\boldsymbol{S}_v(k)\boldsymbol{V}(k)-\boldsymbol{U}^{\mathrm{T}}(k)\boldsymbol{S}_u^{\mathrm{T}}(k)\tilde{\boldsymbol{Q}}\boldsymbol{X}_{\text{ref}}(k) \\
&+\boldsymbol{V}^{\mathrm{T}}(k)\boldsymbol{S}_v^{\mathrm{T}}(k)\tilde{\boldsymbol{Q}}\boldsymbol{S}_x\boldsymbol{x}(k)+\boldsymbol{V}^{\mathrm{T}}(k)\boldsymbol{S}_v^{\mathrm{T}}(k)\tilde{\boldsymbol{Q}}\boldsymbol{S}_u(k)\boldsymbol{U}(k) \\
&+\boldsymbol{V}^{\mathrm{T}}(k)\boldsymbol{S}_v^{\mathrm{T}}(k)\tilde{\boldsymbol{Q}}\boldsymbol{S}_v(k)\boldsymbol{V}(k)-\boldsymbol{V}^{\mathrm{T}}(k)\boldsymbol{S}_v^{\mathrm{T}}(k)\tilde{\boldsymbol{Q}}\boldsymbol{X}_{\text{ref}}(k) \\
&-\boldsymbol{X}_{\text{ref}}^{\mathrm{T}}(k)\tilde{\boldsymbol{Q}}\boldsymbol{S}_x\boldsymbol{x}(k)-\boldsymbol{X}_{\text{ref}}^{\mathrm{T}}(k)\tilde{\boldsymbol{Q}}\boldsymbol{S}_u(k)\boldsymbol{U}(k) \\
&-\boldsymbol{X}_{\text{ref}}^{\mathrm{T}}(k)\tilde{\boldsymbol{Q}}\boldsymbol{S}_v(k)\boldsymbol{V}(k)+\boldsymbol{X}_{\text{ref}}^{\mathrm{T}}(k)\tilde{\boldsymbol{Q}}\boldsymbol{X}_{\text{ref}}(k) \\
=&\|\boldsymbol{S}_x\boldsymbol{x}(k)\|_{\tilde{\boldsymbol{Q}}}^2+2\boldsymbol{x}^{\mathrm{T}}(k)\boldsymbol{S}_x^{\mathrm{T}}\tilde{\boldsymbol{Q}}\boldsymbol{S}_u(k)\boldsymbol{U}(k)+2\boldsymbol{V}^{\mathrm{T}}(k)\boldsymbol{S}_v^{\mathrm{T}}(k)\tilde{\boldsymbol{Q}}\boldsymbol{S}_x\boldsymbol{x}(k) \\
&-2\boldsymbol{X}_{\text{ref}}^{\mathrm{T}}(k)\tilde{\boldsymbol{Q}}\boldsymbol{S}_x\boldsymbol{x}(k)+\boldsymbol{U}^{\mathrm{T}}(k)\boldsymbol{S}_u^{\mathrm{T}}(k)\tilde{\boldsymbol{Q}}\boldsymbol{S}_u(k)\boldsymbol{U}(k) \\
&+2\boldsymbol{V}^{\mathrm{T}}(k)\boldsymbol{S}_v^{\mathrm{T}}(k)\tilde{\boldsymbol{Q}}\boldsymbol{S}_u(k)\boldsymbol{U}(k)-2\boldsymbol{X}_{\text{ref}}^{\mathrm{T}}(k)\tilde{\boldsymbol{Q}}\boldsymbol{S}_u(k)\boldsymbol{U}(k) \\
&+\|\boldsymbol{S}_v(k)\boldsymbol{V}(k)\|_{\tilde{\boldsymbol{Q}}}^{\mathrm{T}}-2\boldsymbol{X}_{\text{ref}}^{\mathrm{T}}(k)\tilde{\boldsymbol{Q}}\boldsymbol{S}_v(k)\boldsymbol{V}(k)+\|\boldsymbol{X}_{\text{ref}}(k)\|_{\tilde{\boldsymbol{Q}}}^2 \\
=&\boldsymbol{U}^{\mathrm{T}}(k)\boldsymbol{S}_u^{\mathrm{T}}(k)\tilde{\boldsymbol{Q}}\boldsymbol{S}_u(k)\boldsymbol{U}(k)+2\big(\boldsymbol{x}^{\mathrm{T}}(k)\boldsymbol{S}_x^{\mathrm{T}}\tilde{\boldsymbol{Q}}\boldsymbol{S}_u(k) \\
&+\boldsymbol{V}^{\mathrm{T}}(k)\boldsymbol{S}_v^{\mathrm{T}}(k)\tilde{\boldsymbol{Q}}\boldsymbol{S}_u(k)-\boldsymbol{X}_{\text{ref}}^{\mathrm{T}}(k)\tilde{\boldsymbol{Q}}\boldsymbol{S}_u(k)\big)\boldsymbol{U}(k) \\
&+2\big(\boldsymbol{V}^{\mathrm{T}}(k)\boldsymbol{S}_v^{\mathrm{T}}(k)\tilde{\boldsymbol{Q}}\boldsymbol{S}_x\boldsymbol{x}(k)-\boldsymbol{X}_{\text{ref}}^{\mathrm{T}}(k)\tilde{\boldsymbol{Q}}\boldsymbol{S}_x\boldsymbol{x}(k) \\
&-\boldsymbol{X}_{\text{ref}}^{\mathrm{T}}(k)\tilde{\boldsymbol{Q}}\boldsymbol{S}_v(k)\boldsymbol{V}(k)\big)+\|\boldsymbol{S}_x\boldsymbol{x}(k)\|_{\tilde{\boldsymbol{Q}}}^2 \\
&+\|\boldsymbol{S}_v(k)\boldsymbol{V}(k)\|_{\tilde{\boldsymbol{Q}}}^{\mathrm{T}}+\|\boldsymbol{X}_{\text{ref}}(k)\|_{\tilde{\boldsymbol{Q}}}^2 \qquad \text{(C.6)}
\end{aligned}$$

The second term of (C.3a) can be expanded as shown below:

$$\begin{aligned}
\|\boldsymbol{U}(k)-\boldsymbol{U}_{\text{ref}}(k)\|_{\tilde{\boldsymbol{R}}}^2 &= (\boldsymbol{U}(k)-\boldsymbol{U}_{\text{ref}}(k))^T\tilde{\boldsymbol{R}}(\boldsymbol{U}(k)-\boldsymbol{U}_{\text{ref}}(k)) \\
&= (\boldsymbol{U}^T(k)\tilde{\boldsymbol{R}}-\boldsymbol{U}_{\text{ref}}^T(k)\tilde{\boldsymbol{R}})(\boldsymbol{U}(k)-\boldsymbol{U}_{\text{ref}}(k)) \\
&= \boldsymbol{U}^T(k)\tilde{\boldsymbol{R}}\boldsymbol{U}(k)-\boldsymbol{U}^T(k)\tilde{\boldsymbol{R}}\boldsymbol{U}_{\text{ref}}(k)-\boldsymbol{U}_{\text{ref}}^T(k)\tilde{\boldsymbol{R}}\boldsymbol{U}(k)+\boldsymbol{U}_{\text{ref}}^T(k)\tilde{\boldsymbol{R}}\boldsymbol{U}_{\text{ref}}(k) \\
&= \boldsymbol{U}^T(k)\tilde{\boldsymbol{R}}\boldsymbol{U}(k)-2\boldsymbol{U}_{\text{ref}}^T(k)\tilde{\boldsymbol{R}}\boldsymbol{U}(k)+\|\boldsymbol{U}_{\text{ref}}(k)\|_{\tilde{\boldsymbol{R}}}^2 \qquad \text{(C.7)}
\end{aligned}$$

The third term of (C.3a) can be expanded as shown below:

$$\begin{aligned}\left\|\tilde{\mathbf{I}}_{\Delta u}\boldsymbol{U}(k)-\tilde{\mathbf{I}}_{\Delta u,\text{init}}\boldsymbol{u}(k-1)\right\|^2_{\tilde{\boldsymbol{R}}_{\Delta u}} =&(\tilde{\mathbf{I}}_{\Delta u}\boldsymbol{U}(k)-\tilde{\mathbf{I}}_{\Delta u,\text{init}}\boldsymbol{u}(k-1))^T\tilde{\boldsymbol{R}}_{\Delta u}\\ &(\tilde{\mathbf{I}}_{\Delta u}\boldsymbol{U}(k)-\tilde{\mathbf{I}}_{\Delta u,\text{init}}\boldsymbol{u}(k-1))\\ =&(\boldsymbol{U}^T(k)\tilde{\mathbf{I}}^T_{\Delta u}\tilde{\boldsymbol{R}}_{\Delta u}-\boldsymbol{u}^T(k-1)\tilde{\mathbf{I}}^T_{\Delta u,\text{init}}\tilde{\boldsymbol{R}}_{\Delta u})\\ &(\tilde{\mathbf{I}}_{\Delta u}\boldsymbol{U}(k)-\tilde{\mathbf{I}}_{\Delta u,\text{init}}\boldsymbol{u}(k-1))\\ =&\boldsymbol{U}^T(k)\tilde{\mathbf{I}}^T_{\Delta u}\tilde{\boldsymbol{R}}_{\Delta u}\tilde{\mathbf{I}}_{\Delta u}\boldsymbol{U}(k)-\boldsymbol{U}^T(k)\tilde{\mathbf{I}}^T_{\Delta u}\tilde{\boldsymbol{R}}_{\Delta u}\tilde{\mathbf{I}}_{\Delta u,\text{init}}\boldsymbol{u}(k-1)\\ &-\boldsymbol{u}^T(k-1)\tilde{\mathbf{I}}^T_{\Delta u,\text{init}}\tilde{\boldsymbol{R}}_{\Delta u}\tilde{\mathbf{I}}_{\Delta u}\boldsymbol{U}(k)+\left\|\tilde{\mathbf{I}}_{\Delta u,\text{init}}\boldsymbol{u}(k-1)\right\|\\ =&\boldsymbol{U}^T(k)\tilde{\mathbf{I}}^T_{\Delta u}\tilde{\boldsymbol{R}}_{\Delta u}\tilde{\mathbf{I}}_{\Delta u}\boldsymbol{U}(k)-2\boldsymbol{u}^T(k-1)\tilde{\mathbf{I}}^T_{\Delta u,\text{init}}\tilde{\boldsymbol{R}}_{\Delta u}\tilde{\mathbf{I}}_{\Delta u}\boldsymbol{U}(k)\\ &+\left\|\tilde{\mathbf{I}}_{\Delta u,\text{init}}\boldsymbol{u}(k-1)\right\|^2_{\tilde{\boldsymbol{R}}_{\Delta u}} \qquad \text{(C.8)}\end{aligned}$$

Using (C.6)–(C.8) above, the cost can be rewritten as shown below:

$$J_k=\boldsymbol{U}^T(k)\boldsymbol{\Gamma}(k)\boldsymbol{U}(k)+2\boldsymbol{\Upsilon}^{\mathrm{T}}(k)\boldsymbol{U}(k)+\Theta(k), \qquad \text{(C.9a)}$$

where

$$\boldsymbol{\Gamma}(k)=\boldsymbol{S}_u^{\mathrm{T}}(k)\tilde{\boldsymbol{Q}}\boldsymbol{S}_u(k)+\tilde{\boldsymbol{R}}+\tilde{\mathbf{I}}^T_{\Delta u}\tilde{\boldsymbol{R}}_{\Delta u}\tilde{\mathbf{I}}_{\Delta u}, \qquad \text{(C.9b)}$$

$$\begin{aligned}\boldsymbol{\Upsilon}^{\mathrm{T}}(k)=&\boldsymbol{x}^{\mathrm{T}}(k)\boldsymbol{S}_x^{\mathrm{T}}\tilde{\boldsymbol{Q}}\boldsymbol{S}_u(k)+\boldsymbol{V}^{\mathrm{T}}(k)\boldsymbol{S}_v^{\mathrm{T}}(k)\tilde{\boldsymbol{Q}}\boldsymbol{S}_u(k)-\boldsymbol{X}_{\text{ref}}^{\mathrm{T}}(k)\tilde{\boldsymbol{Q}}\boldsymbol{S}_u(k)\\ &-\boldsymbol{U}_{\text{ref}}^T(k)\tilde{\boldsymbol{R}}-\boldsymbol{u}^T(k-1)\tilde{\mathbf{I}}^T_{\Delta u,\text{init}}\tilde{\boldsymbol{R}}_{\Delta u}\tilde{\mathbf{I}}_{\Delta u} \qquad \text{(C.9c)}\end{aligned}$$

and

$$\begin{aligned}\Theta(k)=&2\big(\boldsymbol{V}^{\mathrm{T}}(k)\boldsymbol{S}_v^{\mathrm{T}}(k)\tilde{\boldsymbol{Q}}\boldsymbol{S}_x\boldsymbol{x}(k)-\boldsymbol{X}_{\text{ref}}^{\mathrm{T}}(k)\tilde{\boldsymbol{Q}}\boldsymbol{S}_x\boldsymbol{x}(k)-\boldsymbol{X}_{\text{ref}}^{\mathrm{T}}(k)\tilde{\boldsymbol{Q}}\boldsymbol{S}_v(k)\boldsymbol{V}(k)\big)\\ &+\|\boldsymbol{S}_x\boldsymbol{x}(k)\|^2_{\tilde{\boldsymbol{Q}}}+\|\boldsymbol{S}_v(k)\boldsymbol{V}(k)\|^2_{\tilde{\boldsymbol{Q}}}+\|\boldsymbol{X}_{\text{ref}}(k)\|^2_{\tilde{\boldsymbol{Q}}}+\|\boldsymbol{U}_{\text{ref}}(k)\|^2_{\tilde{\boldsymbol{R}}}\\ &+\left\|\tilde{\boldsymbol{I}}_{\Delta u,\text{init}}\boldsymbol{u}(k-1)\right\|^2_{\tilde{\boldsymbol{R}}_{\Delta u}}. \qquad \text{(C.9d)}\end{aligned}$$